ALMA MATER STUDIORUM
UNIVERSITÀ DI BOLOGNA

DOTTORATO DI RICERCA IN

INGEGNERIA BIOMEDICA, ELETTRICA E DEI SISTEMI

Ciclo 37

Settore Concorsuale: 09/E2 - Ingegneria dell'Energia Elettrica

Settore Scientifico Disciplinare: ING-IND/32 - Convertitori, Macchine e Azionamenti Elettrici

INNOVATIVE APPROACHES FOR POWER CONVERSION FROM RENEWABLES

Presentata da: ***Elena Macrelli***

Coordinatore Dottorato
Michele Monaci

Supervisore
Alberto Bellini

Co-Supervisore
Angelo Tani

Esame finale anno 2025

ALMA MATER STUDIORUM
UNIVERSITY OF BOLOGNA

PH.D. PROGRAMME
BIOMEDICAL, ELECTRICAL AND SYSTEMS ENGINEERING
(IBES)

SSD ING-IND/32

INNOVATIVE APPROACHES FOR POWER CONVERSION FROM RENEWABLES

Ph.D. Thesis

Ph.D. candidate
ELENA MACRELLI

Supervisor
Prof.
ALBERTO BELLINI

Ph.D. coordinator
Prof.
MICHELE MONACI

Co-Supervisor
Prof.
ANGELO TANI

XXXVII° CYCLE

KEYWORDS

Renewable Energy Sources

Energy Transition

Energy Storage

Flywheel Batteries

Acknowledgments

I would like to remember all the people I met during these wonderful three years of my Ph.D.
Each one of them was special to me and taught me so much.
Without them, this experience would never have been so enriching.

Elena

Abstract

The following thesis summarizes the main results achieved during my Ph.D. research focused on power conversion from renewable energy sources. Two case studies are presented, both exploring innovative approaches to established renewable energy technologies.

The first one focuses on an interesting solution for residential energy storage, i.e. Flywheel Energy Storage Systems (FESS). FESS are already a mature technology for some specific applications but the idea is to extend their field to domestic uses too. The idea is to employ them as an alternative to chemical batteries for energy storage when coupled, for example, with a residential photovoltaic panel. The working principles and state of the art of this technology are exposed along with their advantages and drawbacks with respect to other solutions.

An ironless dual-rotor electric machine prototype, named MechSTOR, is presented. The prototype has been specifically designed and realized for FESS application in order to increase its self-discharge duration time. A thorough analysis of the machine is provided both with simulations and experimental tests. Performances are assessed both from the mechanical and electromagnetic domains. In addition to that, different motordrive solution to ensure the optimal performance of the machine are explored.

As for the complete FESS system, a tool is presented that allows to simulate the bidirectional power flow between all the nodes and estimate the final energy savings. This simulation model is an useful support for the optimal design of the complete system. In fact, it allows to find the best match between the size of all the system components and the power profiles of PV generation and electric load consumption. FESS is simulated both

as standalone technology and included in a Hybrid Energy Storage System (HESS) with a chemical battery.

The second case study focuses on power conversion systems for wind energy. The physical basis of power generation from wind turbines and the state of the art of this technology are presented. After that, an innovative configuration for a Permanent Magnet Synchronous Motor (PMSM) is proposed. This solution is the Opened End PMSM (OW-PMSM) fed by a dual inverter. This motordrive presents a number of advantages that make them an ideal technology for wind turbines, e.g. higher energy density and higher fault tolerance. However, OW-PMSM fed by a dual inverter with a common DC bus is affected by a Zero Sequence Current (ZSC) circulation. ZSC significantly decreases OW-PMSM performances, thus, it must be minimized through proper modulation of the phase voltages of the motors. In addition to that, because of the dual inverter, switching losses are double the one of a conventional single inverter motordrive. A modulation technique based on Discontinuous Pulse Width Modulation (DPWM) is proposed to cancel out the ZSC achieving, at the same time, a consistent reduction of the switching losses of the double inverter system. The technique is explained in detail and validated by presenting results of the experimental tests.

Contents

Chapter 1

Transition to Renewables: Current Scenario and Pathway

1.1 Greenhouse Gases and Climate Change

Human activity emits around 50 billion tonnes of greenhouse gases each year measured in carbon dioxide equivalents (CO2eq). This unit sums up all the warming impacts of the different greenhouse gases by taking into account their "global warming potential" (GWP): the warming impact of a gas compared to carbon dioxide. In fact, carbon dioxide (CO2) due to the use of fossil fuels dominates the total emissions (74.1%) but there are other greenhouse gases: methane (CH4) and nitrous oxide (N2O) (mostly from agriculture, waste treatment and gas flaring) and fluorinated gases (HFCs, PFCs, SF6, NF3) (from industrial processes). Their share in the total emissions is lower, but these gases are much more potent than CO2 in terms of their GWP [1].

1.1.1 The Role of the Energy Sector

As for the sources of the human-caused greenhouse gas emissions, the energy sector is by far the most impacting one, as shown in Fig. 1.1. The energy sector includes electricity and heat, transportation, buildings, manufacturing and construction, other fuel combustion and fugitive emissions. According to 2021 data, energy accounts for the 75.4% (37.41 GtCO2e) of the world

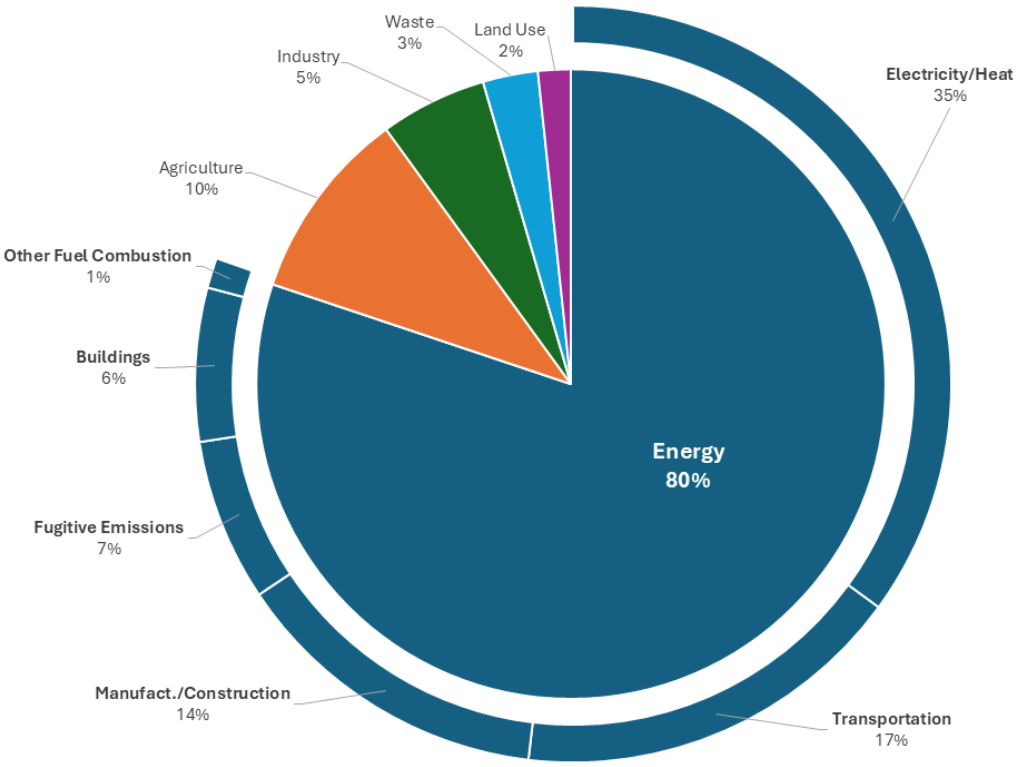

Figure 1.1: Global GHG emissions share of each sector (2021 data) [2].

emissions, followed by agriculture (5.86 GtCO2e), industry (3.26 GtCO2e), waste (1.68 GtCO2e) and land use (1.34 GtCO2e) [2]. These values include not only direct emissions from fossil fuel combustion but also indirect emissions from collateral activities such as the use of electricity. Within the energy sector, heat and electricity generation is responsible for most emissions (31.8%), followed by transportation (17%) and manufacturing and construction (12.7%). In addition to that, the first two subsectors are two of the three fastest-growing sources of greenhouse gas emissions. Since 1990, electricity and heating grew by 84% and transportation by 78% along with a 203% increase in industrial processes also. The growth in industrial emissions is due also to the potent HFCs, originated by the increased use of refrigeration and air conditioning. In a world where huge numbers of people still do not have access to household electricity, the emissions of this sector are projected to increase even more in the future.

1.1.2 A Pathway for Net Zero Emissions

The consequences of global warming long ago predicted and the visible climate impacts unfolding right now under the current 1.1°C show the urgency of minimizing temperature increase [4], [5]. By signing the Paris Agreement at the UN Climate Change Conference (COP21) in 2015, 196 parties agreed to pursue efforts "to limit the temperature increase to 1.5°C above pre-industrial levels." In the latest installment of the Intergovernmental Panel on Climate Change's (IPCC) Sixth Assessment Report, 278 scientists from 65 countries confirmed that global GHG emissions must peak before 2025 to increase our chances of meeting the Paris Agreement's 1.5°C target [6]. Notwithstanding this, GHG emissions have continued to rise over the past decade and projections forecast a 2.8°C temperature increase by the end of the century if we keep on following the climate policies currently in place [7]. Fig. 1.2 shows a projection of the global emissions for the energy sector by 2030 and two IEA produced scenarios are compared. The Pre-Paris Baseline Scenario is based on the policies that were in place in 2015 [8] while the Stated Policies Scenario (STEPS) considers the currently established and planned policies. As visible, projected expansion of renewable energy sources allows significant reduction in GHG emissions (about 6 GtCO2e), but this

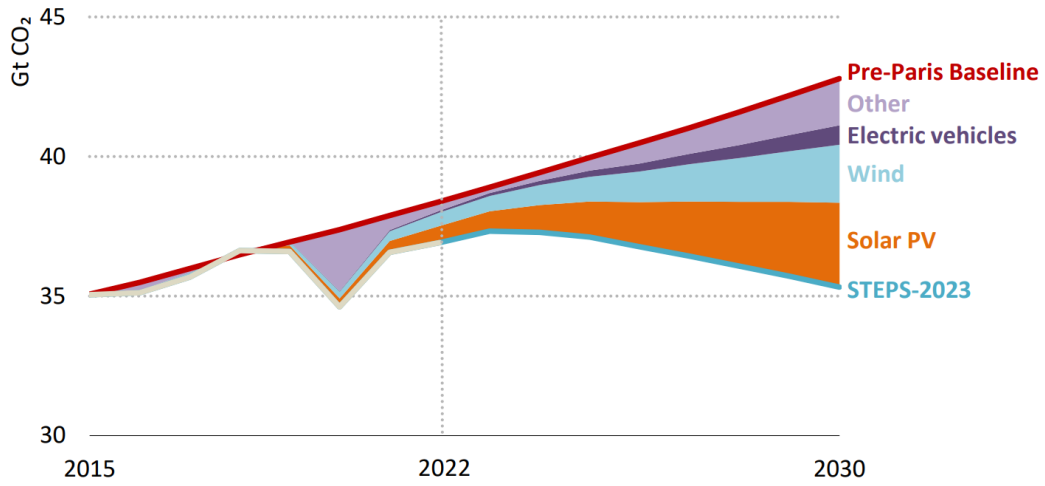

Figure 1.2: Global energy sector CO2 emissions in the Pre-Paris Baseline Scenario and STEPS, 2015-2030 [3].

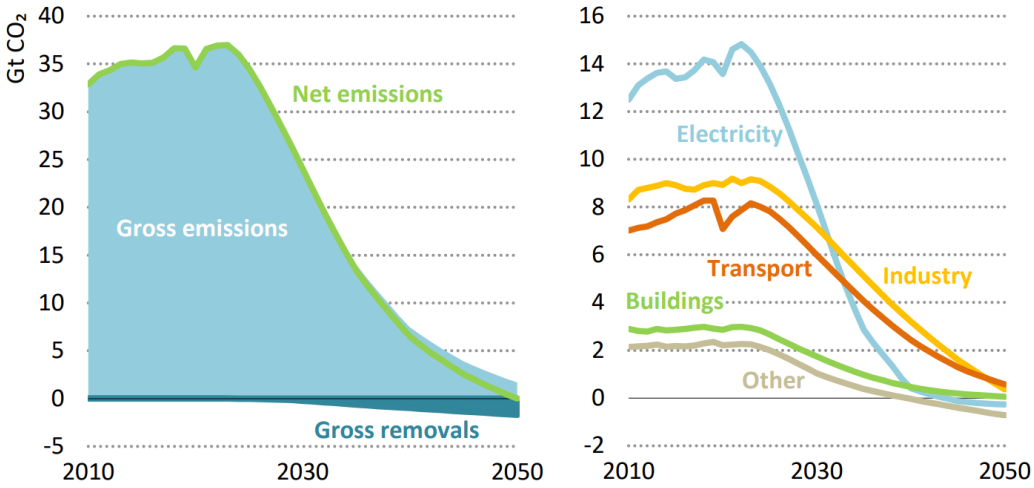

Figure 1.3: Energy sector gross emissions and removals, total net CO2 emissions, and net emissions by sector in the NZE Scenario, 2010-2050 [3].

is not enough to meet the 1.5°C target. In its 2023 updated report, the IEA translates Paris Agreement's target into a concrete set of actions to reach a milestone: net zero emissions by 2050 [3]. This Net Zero Emissions Scenario (NZE) focuses on the energy sector, the most impacting one in terms of GHG emissions, and deploys a wide portfolio of clean energy technologies. In addition to that, this path includes universal access to electricity and clean cooking by 2030. The projected GHG emission reduction for the energy sector in the NZE are shown in Fig. 1.3.

This roadmap shows that limiting global warming to 1.5°C is still within reach, but very ambitious actions, transformational change and collaborations between countries are required.

1.2 Levers for Net Zero Emissions

In order to reach the 2050 net zero emissions milestone, NZE scenario identifies some key actions that must be launched, summarized in Fig. 1.4. Clean energy technologies available today deliver more than 80% of the emissions reductions needed by 2030. Thus, in order to bend the emissions curve sharply downwards, an acceleration is needed, driven by well-designed poli-

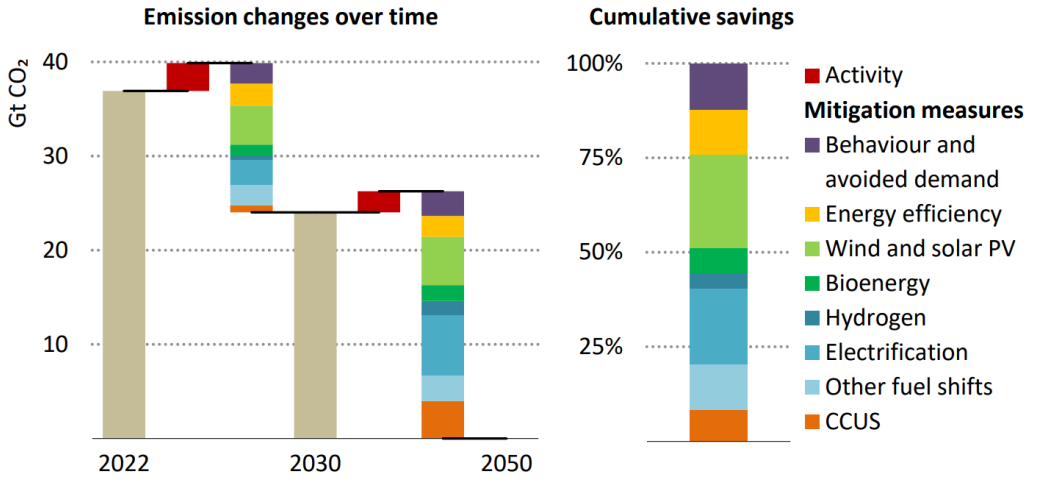

Figure 1.4: CO2 emissions reductions by mitigation measure in the NZE Scenario, 2022-2050 [3].

cies facilitating declines in fossil fuel demand and clean energy expansion.

1.2.1 Tripling of Global Installed Renewables Capacity

The most effective lever to cut emission in the NZE scenario is the tripling of global installed renewables capacity to 11000 GW by 2030. Between 2015 and 2022, standardisation and short lead times allowed considerable growth for mass manufactured technologies such as solar PV (400% capacity increase), electric car (2000% sales increase), residential heat pump (225% sale increase) and stationary battery storage (2500% capacity increase) [3]. Historical data and 2023 estimates of renewable electricity capacity additions are shown in Fig. 1.5. With the current rate, advanced economies and China are expected to reach around 85% of the required renewables capacity by 2030. However, deployment has been uneven across regions: developing economies have significant potential to expand renewables cost effectively and require the largest boost, as shown in Fig. 1.6. Hence more supportive policy environments and international support are needed in other developing countries.

As for the competitiveness of renewable energy sources, currently, the generation costs of new solar PV and onshore wind installations are mostly lower than the generation costs of of new coal and natural gas plants. Their

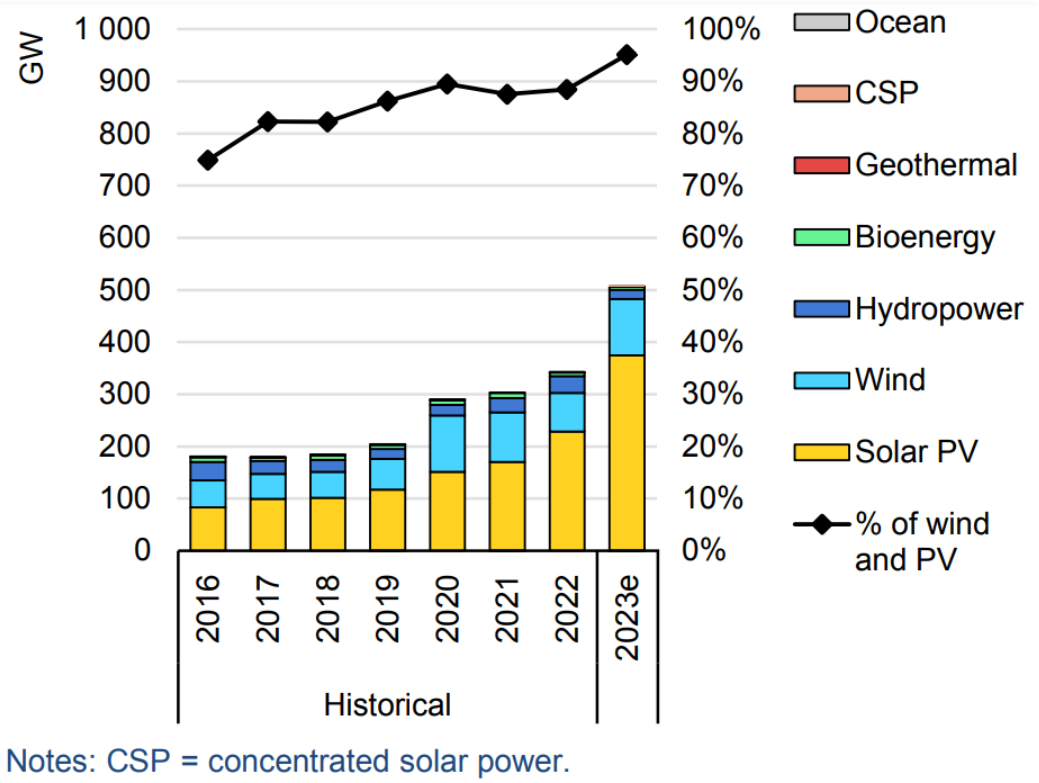

Figure 1.5: Historical data and 2023 estimates of renewable electricity capacity additions by technology (adapted from [9]).

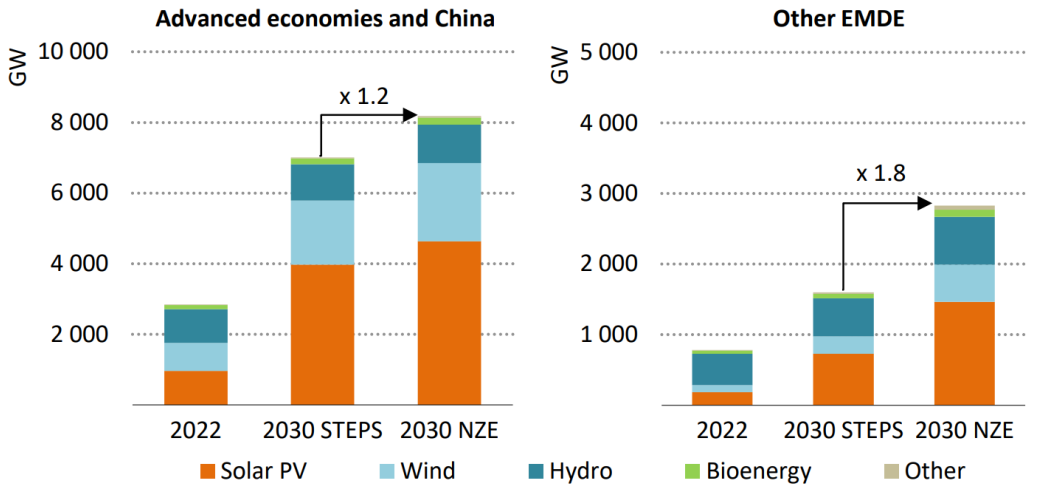

Figure 1.6: Installed and required renewables capacity by technology and economic grouping in the STEPS and NZE Scenario, 2022 and 2030 [3].

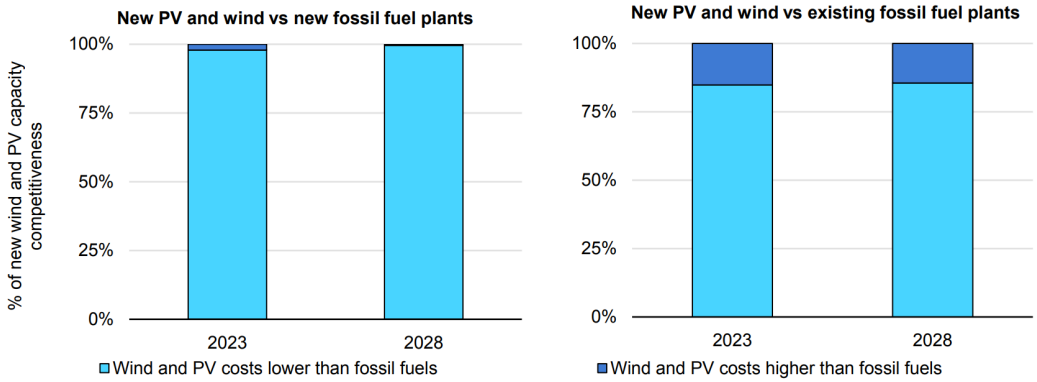

Figure 1.7: Share of utility-scale wind and PV with lower levelised cost of energy than new coal and natural gas power plants (left) and existing plants (right), 2023-2028 (adapted from [9]).

competitiveness is expected to further improve. Fig. 1.7 shows the percentage of newly installed utility-scale wind and PV divided between less competitive (light-blue) and more competitive (dark blue). Their cost is compared with new fossil fuel-fired plants (left graph) and already existing ones (right graph). 2028 data were estimated with STEPS scenario. The share of more competitive PV and wind plants is projected to increase, also when compared to already existing fossil fuel-fired plant. It must be underlined, however, that assessing competitiveness based on generation costs only might be misleading for variable renewable energy sources. As previously mentioned, they require to be integrated in flexible power plants and to be coupled with storage at higher penetration levels.

1.2.2 Electrification of the Energy System

This great increase in renewable capacity needs to be employed in all activities previously served by fossil fuels. Thus, electrification of end-uses in transport, buildings and industry is mandatory. Currently, the growth rate of electric cars sales is enough to meet the 2030 level of deployment required by NZE Scenario, but uptake is needed in trucks. Moreover, installations of heat pumps must expand to 20% per year to 2030, almost double that the current rate. Clearly, also an upgrade in the energy system infrastructure is needed: transmission and distribution grids must expand by around

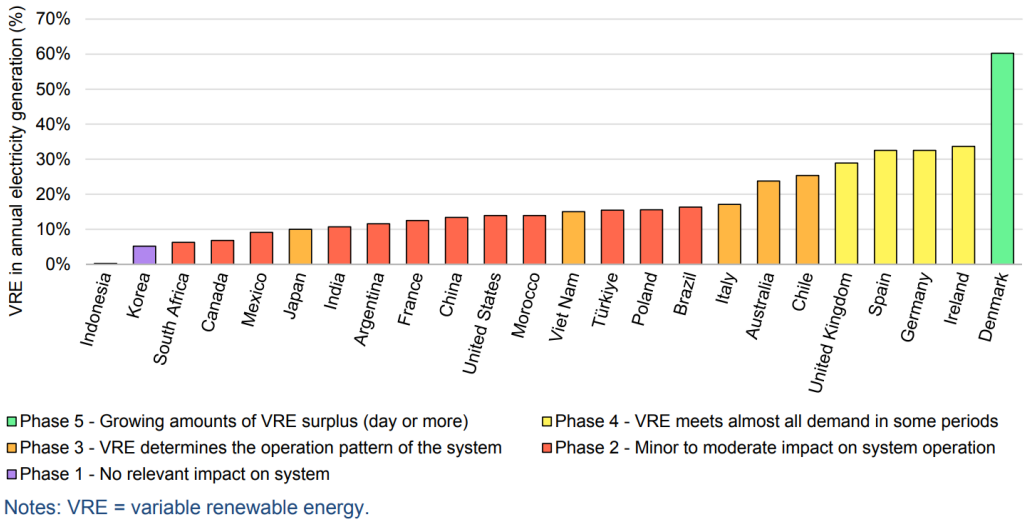

Figure 1.8: Countries in phases of renewables integration, 2022 [9].

2 million km each year to 2030 [3]. In fact, grid expansion must keep pace with variable renewable energy growth. In Fig. 1.8, different countries have been categorized in six phases based on the challenges power systems face with increasing renewable energy penetration. In Phase 1, where most countries fall into currently, renewables have no significant impact at the system level. However, an increasing number of regions are entering higher phases, with Denmark already in Phase 5, and more are expected to speed up in the future. In fact, renewable energy sources such as wind and PV can cause net load variability and changes in power flow patterns because of their variability. With their expansion in the grid, they will increasingly determine how the system operates. The impact on the grid depends on the correlation between renewable production and electricity demand, the relative share and complementarity of PV wind and countries interconnection capacities with other grid areas to manage possible subregional challenges. Hence, efficient investments in grid infrastructure are needed to manage both possible curtailment and surplus production. Energy storage systems will be crucial for integrating renewable energy sources efficiently, as it will be presented in Chapter 2.

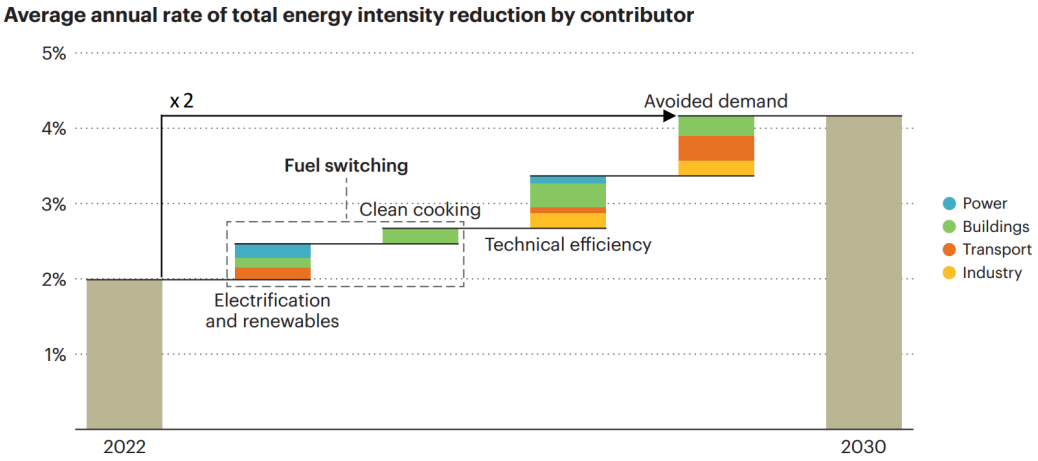

Figure 1.9: Average annual rate of total energy intensity reduction by contributor [3].

1.2.3 Double the Rate of Energy Intensity Improvement

Boost the renewable energy production and electrification, however, is not sufficient. In fact, NZE scenario requires to double the annual rate of energy intensity improvements by 2030. This will allow not only a consistent cut to emissions but also improvements in energy security and affordability, mandatory to guarantee universal access to clean energy. The set of actions to be carried out includes: improving the technical efficiency of electric equipment (electric motors, air conditioners, household appliances, etc.) switching to clean fuels (such as electricity and clean cooking solutions) and a more efficient use of energy and materials. In particular, improvements in the efficiency of buildings are of the utmost importance, as underlined in green in Fig. 1.9. Finally, behavioural changes have a significant role and avoided demand saves five-times more energy per capita in advanced economies, compared with developing economies, as shown in Fig. 1.10. In fact, household behaviors are estimated to account for for 72% of global GHG emissions [10]. Recent policy interventions related to the Covid pandemic in 2019 and energy crisis in 2022 already led the path and showed the feasibility of this action. Thus, further measures must be adopted to speed up efficiency.

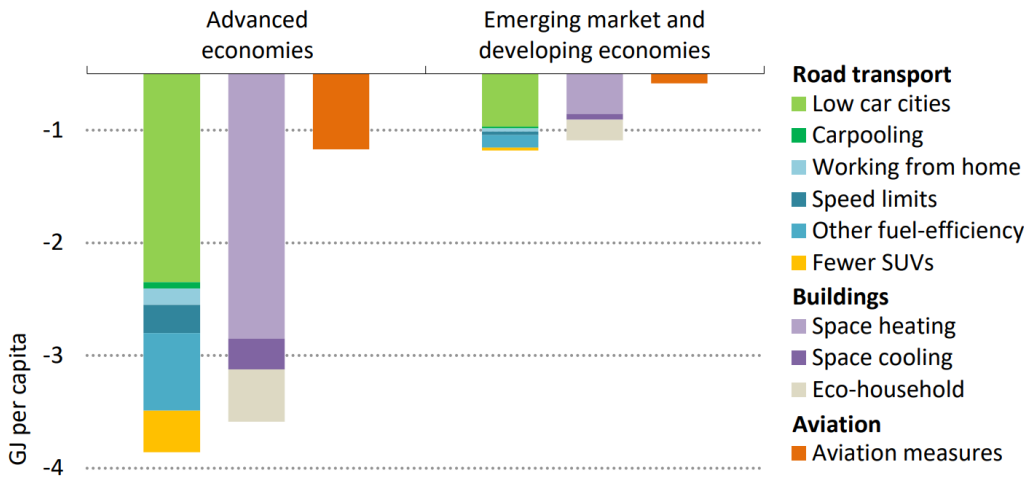

Figure 1.10: Changes in energy per capita consumption from behavioural measures in the NZE Scenario, 2030 [3].

1.2.4 Slash Methane Emissions and Coal Plants Dismission

Methane emissions have an impressive impact on global temperatures in the short term because, even if its lifetime in the atmosphere is short, its GWP is 28 times higher [11]. In fact, methane has been responsible for around one-quarter of radiative forcing since 1750 [12]. The energy sector is responsible for 40% of total methane emissions, second only to agriculture. Thus, it is mandatory to achieve a 75% cut of methane emissions in the energy sector by 2023 and it is one of the least cost opportunities to limit global warming in the near term. Methane emissions stems from fossil fuels operations: production, processing, storage, transportation and nearly leaking from end-use equipment. Fig. 1.11 shows that NZE target will be achieved by explicit action plans to support reductions but also by the decline in fossil fuel demand thanks to electrification.

Finally, it should be underlined a non-negotiable milestone already declared in the 2021 version of the NZE roadmap: an immediate end to new approvals of unabated coal plants [13]

With the gradual dismission of fossil-fuel fired plants, some thermal plants will be still needed as a support for energy security. For example, nuclear

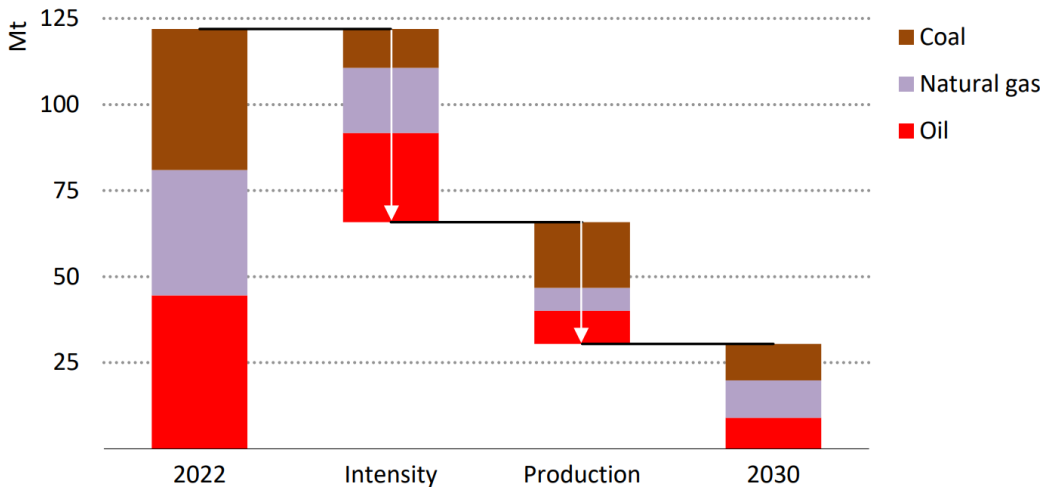

Figure 1.11: Methane emissions from fossil fuel operations and reductions in the NZE Scenario, 2022-2030 [3].

power will have an important role in the NZE scenario. Nuclear energy contribution is higher in the first decades, with its output rising by 40% to 2030 and doubling by 2050. Its overall share of generation, however, stalls to 10% in 2050 [13].

1.2.5 Further Advance in Innovation

Still, further advances in innovation is needed for some sectors such as heavy industry and long-distance transport. In these cases, emissions are harder to cut because the required low-emissions technologies are not yet readily available. On a brighter note, the readiness level of some critical clean energy technologies has made considerable progress in recent years, as shown in Fig. 1.12. Grid scale renewables plants and scaled up batteries almost reached maturity while carbon capture technologies and solid oxide electrolysers for low-emissions hydrogen supply are approaching the market uptake. Especially, hydrogen and hydrogen-based fuels and carbon capture, utilisation and storage (CCUS) have an important role in emissions cutting for heavy industry and long-distance transport. If all planned projects for hydrogen electrolysis capacity and CCUS are realised, they would provide around 70% and 40%, respectively, of the required amount in the NZE Scenario by 2030.

Further acceleration will thus be central to decarbonize these sectors.

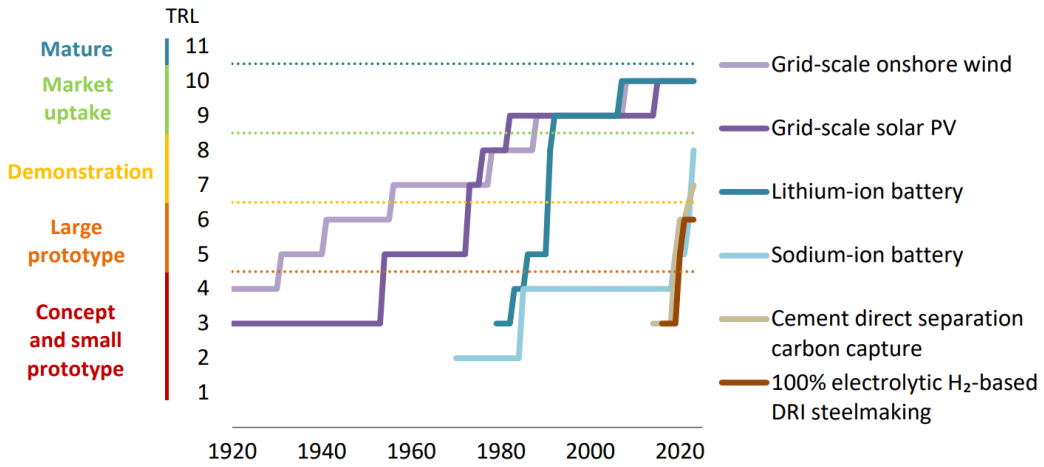

Figure 1.12: Evolution of technology readiness levels for selected clean energy technologies [3].

Chapter 2

Energy Storage: Enabling Technology for the Transition

2.1 Features and Limitations of Renewable Energy Sources

Renewable energy is defined as the energy obtained from natural sources that are replenished at a higher rate than they are consumed. Clearly, the main advantage of renewable energy is the far lower amount of GHG emitted by energy generation with respect to fossil-fuels combustion. In addition to that, renewable energy sources (RES) are plentiful and readily available in nature and, especially in recent years, cheaper than many fossil-fuel based sources. On the other hand, they have some peculiar features that pose certain challenges in their full employment and efficient integration in the existing grid. These peculiarities, however, can also offer some opportunities of improvements in terms of energy security and independence of the user to the main grid.

2.1.1 Variable RES

The first distinctive characteristic of RES is that, being natural sources, the generated energy amount is subject to variability due to the weather and en-

vironmental conditions. By considering this aspect, a first distinction must be traced between different RES. In fact, wind and, especially, PV are way more dependent on weather conditions than other RES, such as geothermal and hydropower, which are usually condensed in centralized plants and provide a more stable output. Due to their intermittency, they may be addresses as variable renewable energy sources. As previously shown, variable RES are expected to play a major role in the energy transition. Thus, proper management is of the utmost importance to guarantee their optimal employment and efficient integration in the grid.

Because of their intermittency, there is usually a mismatch between the RES generation curve and the demand curve, leading to time intervals of both power shortage and surplus. The most straightforward example is the one of a residential PV module: power generation happens during daylight hours and stops after sunset. Many consumers follow similar daily routines such as returning home from job around the same time. This means that, in the evening, many commuters may want to use electric household equipment, switch on the heat pumps, charge the EV, etc. Hence, during the day there is a surplus production of energy while power demand spikes in the evening, when no power is generated. Fig. 2.1 shows the electricity demand and energy generation curves of different sources during a sample day in India. Two energy mix are considered: the present day one, relying mostly on fossil fuels, and the projected 2050 one under the NZE path. As visible, while the 2022 generation profile was more stable and in line with the demand curve, the penetration of solar PV causes huge peaks in 2050 energy production.

The power system has always needed to ensure instantaneous stability and long-term security of supply. Flexibility is the capacity to manage the variability and mismatch between generation and demand over all timescales, from daily cycles down to the scale of seconds when, for example, clouds interrupt PV power generation. In order to achieve this in a reliable and cost-effective way, backup resources and methods are needed. One of these methods is represented by the variable electric load itself. In fact, electrification is not only increasing the variability of electric power consumption, but also the quantity and variety of electrical equipment that can shift around

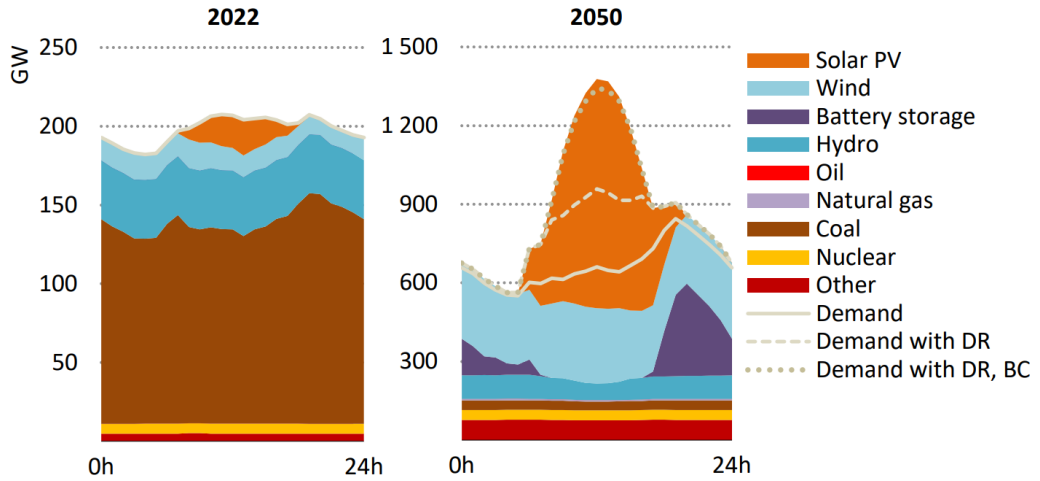

Notes: GW = gigawatt; DR = demand response; BC = battery charging. Demand response includes the flexible operation of electrolysers.

Figure 2.1: Hourly electricity generation by source for a sample day in India in August in the APS, 2022 and 2050 [14].

their load, such as heat pumps, air conditioners and EVs. For example, it is possible to incentivise consumers to preheat buildings when solar generation is abundant to reduce the evening peak demand of heat pumps. Heat pumps are highly efficient producers of heating and cooling per unit of energy input, particularly compared with fossil fuel-based production [15]. Or smart EV charging systems can shift charging loads during surplus production hours. This re-organization of the load is called demand-response and it is set to play an increasingly important part in the provision of short-term flexibility. Alongside demand-response measures, energy storage is recognized as a crucial technology for short-term flexibility [14]. Batteries can charge during excess renewable generation periods and discharge the stored energy during peak demand. Demand-response and energy storage are shown by the dashed line and the blue area, respectively, in Fig. 2.1.

Nowadays, most of the flexibility required across all timescales today is achieved through thermal power plants cycling. In addition to that, hydropower and pumped storage represent a big asset to store surplus production. Fig. 2.2 shows the increase in flexibility needs of the power system along with the measures adopted to meet them, both for short term and seasonal

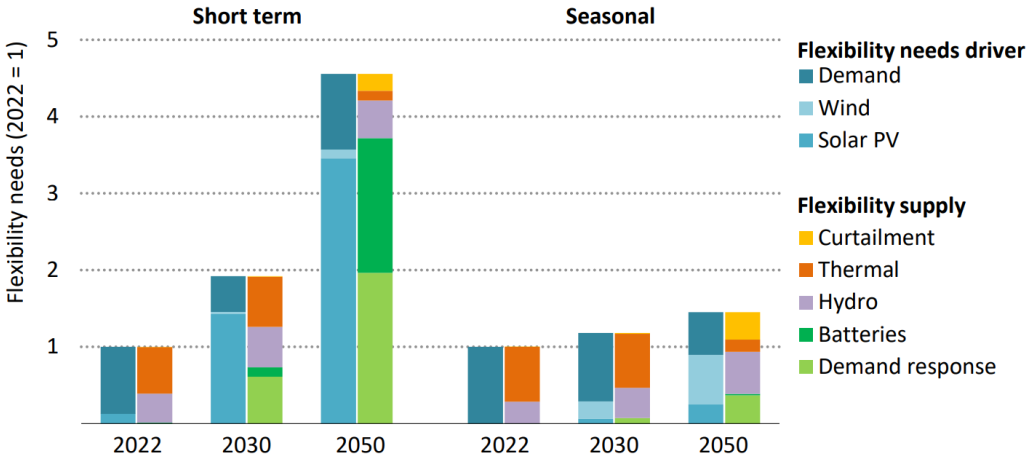

Figure 2.2: Global power system flexibility needs and supply: present ones and projected future ones [14].

variability. Short-term needs grow significantly mainly due to the increasing diffusion of solar PV. Wind penetration, on the other hand, contributes to the less sharp rise of seasonal needs. As the contribution made by thermal power plants wanes, energy storage and demand-response emerge as crucial suppliers of flexibility and become the main measures to meet the flexibility needs by 2050. Hydropower is not projected to grow, but remains a stable and reliable asset, especially for seasonal variability, thanks to its long storing times [16]. When all these solutions fall short, curtailment must come into play to achieve a match between supply and demand.

2.1.2 Distributed RES

Another main feature of wind and PV is the fact that they are distributed. Thanks to their modularity, wind and PV can be organized in bigger size centralized power plants, in line with the current centralized dispatch structure, but also employed as small-scale energy resources usually situated near sites of electricity use. In this last case, they are more difficult to integrate in the existing centralized transmission grids that were mostly designed in the 20th Century. But with the proper technologies, policies and regulations, distributed RES can open new opportunities, improve energy security end reduce overall costs. In fact, the rapid expansion of distributed RES will

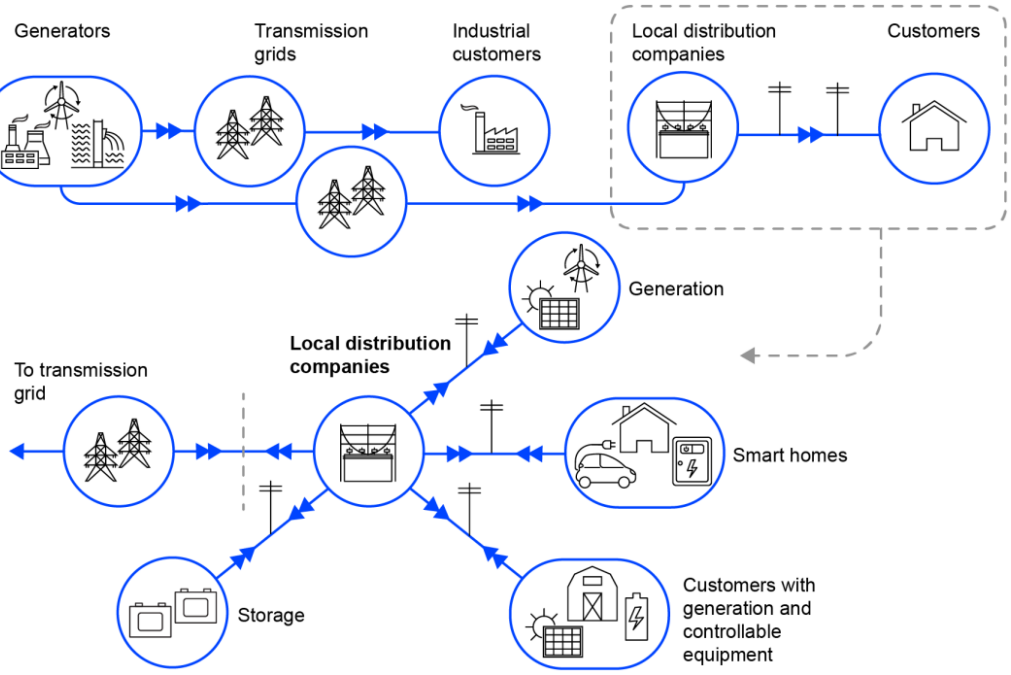

Figure 2.3: Comparison between centralized grid and distributed dispatch of the future (adapted from [15]).

transform not only how power is generated, but also how it is traded, dispatched and consumed. Fig. 2.3 shows a comparison between centralized and distributed dispatch. In the current transmission grid, production is limited to large, centralized plants and trading is managed by few retailers. Moreover, the power flow to the end user is unidirectional. In the future system, the final connection between local distribution companies and customers will be replaced by a smaller scale sub-net, connecting different types of loads and distributed RES and allowing bidirectional power flow.

In this way, consumers have access to affordable electricity and are less dependent on the grid. But, most of all, they become more proactive. In fact, they are able to produce electricity for their own consumption and, in case of surplus production, store it or sell it on the market. Energy storage management and demand-response have to be shaped to respond to market signals by increasing electricity consumption when prices are low and reducing it during peak hours. As an example, EV can be charged overnight when electricity prices are lower, or the unused stored energy can be sold

during peak times when its value is higher. In order to make the most of these opportunities interactive smart energy devices, digital tools and effective demand-response policies are required. But, most of all, affordable and reliable energy storage technologies play the most important role.

2.2 Current Scenario and Trends for Energy Storage

As previously stated, energy storage is the enabling technology for the transition to renewable energy sources generation as it not only addresses their intermittency but also unlocks new possibilities for a non-centralized and reliable transmission grid. Energy storage is an aggregate category including all the technologies that allow to store energy for a later use. In order to achieve that, energy type conversion is always needed thus, losses are involved throughout all the storing process: at energy input, during energy transformation and at energy output. All the different energy storage technologies can be compared on the basis of the following parameters: capacity in terms of energy and power units, energy density and power density (energy and power units per physical unit), storage rates (i.e. how much power can be delivered during charging and discharging), lifetime (i.e. number of charging cycles), depth of discharge and maximum state of charge, and energy cycle efficiencies. Based on the values of these parameters, each storage solution finds its optimal field of application. For the ease of this presentation, energy storage systems available today can be broadly divided into two categories: long-term storage and short-term storage.

2.2.1 Long-term Energy Storage

An energy storage technology can be considered long-term when it can store energy for more than 10 hours. As these solutions allows to store energy for weeks, months or even years, they are best suited to address seasonal and interannual variability in power generation from RES, most of the time for big-scale energy. Long-term energy storage will be of particular importance

Technology	Power range	Storage capacity	Typical round-trip efficiency	TRL[2]
Pumped hydro	10 MW - 5 GW	0.2 - 0.5 GWh	70-85%	11
Compressed air (underground storage)	5 MW - 300 MW	0.2 - 1 GWh	41-75%	9
Thermal storage – low temperature	1 kW - 300 MW	n.a.	30-50%	8-9
Thermal storage – high temperature	1 - 60 MW	n.a.	80%	5-7
Gravitational	1 kW - 25 MW	100 MWh	80%	7
Electrolytic H_2 and gas turbine (GT) in combined cycle	Hundreds of MW	Unlimited	21%-27%	9*
Electrolytic ammonia and direct combustion in GT-combined cycle	Hundreds of MW	Unlimited	22%-24%	9*
Electrolytic H_2 and fuel cell	0.3 - 50 MW	Unlimited	30-50%	7-9

[2] Technology readiness levels (TRL) reference scale: concept development 1-2-3, small prototype 4, large prototype 5-6, demonstration plant 7-8, early adoption 9-10, mature technology 11.

Figure 2.4: Comparison of key parameters for long-term energy storage technologies [16].

toward the end of the NZE path especially, when, thanks to the higher shares of RES, storage requirements will eventually extend beyond hour-to-hour or daily fluctuations to monthly and seasonal timescales.

Pumped-storage Hydroelectricity

Pumped-storage hydroelectricity (PHS) is the main commercially available technology for this category. In fact, PSH that can provide long-duration and grid-scale storage, with high discharge rates, which corresponds to the power that can be delivered by the storage. In addition to that, even if its construction costs are high, they are compensated by very long operational life, making it a low-cost solution also. PSH represents 96% of current global storage capacity [16] but further growth can happen at a slow pace because there are some obvious geographical limitations due to water availability, specific site and environmental requirements.

Long-duration Energy Storage Alternatives

Other long-term energy storage solutions include compressed air energy storage, thermal energy storage and gravitational energy storage. In addition to that, the surplus generated power can be used to operate electrolysers for hydrogen or ammonia production, to be used later as a clean fuel. These are more energy-carriers than energy storage but serve at the need to avoid waste of surplus power and employing it later with no additional emissions.

Long-term energy storage technologies and their key parameters are summarized in Fig. 2.4.

2.2.2 Short-term Energy Storage

Short-duration energy storage present about 1-4 hours of storing times and, usually, have higher charge/discharge rates and are smaller in size than long-term solutions. A mix of flexibility resources is needed to manage variability across all timescales, but currently and in the nearer future, short-duration energy storage will play the central role. In fact, the following years will see a high growth of mostly variable and distributed RES, hence short-duration flexibility resources to address hourly and daily variations are more needed. The increase in variable RES installations will induce a parallel boost in short-term energy storage, with over 400 GW to be deployed between 2023 and 2028, as shown in Fig. 2.5. Existing long-term storage capabilities will continue their contribution, but their deployment will remain limited compared with short-term energy storage because of the longer development and permitting timelines, as well as limited natural resources in some areas In order to promote the evolution of the distributed energy system of the future, these storage technologies require small-medium sizes allowing their optimal paired with smaller-scale distributed RES. But, most of all, storage technologies must be cheap, in line with the decline of RES prices, especially if they are employed on a residential level. Otherwise, large costs would be added to our energy system, failing the affordability of RES [17].

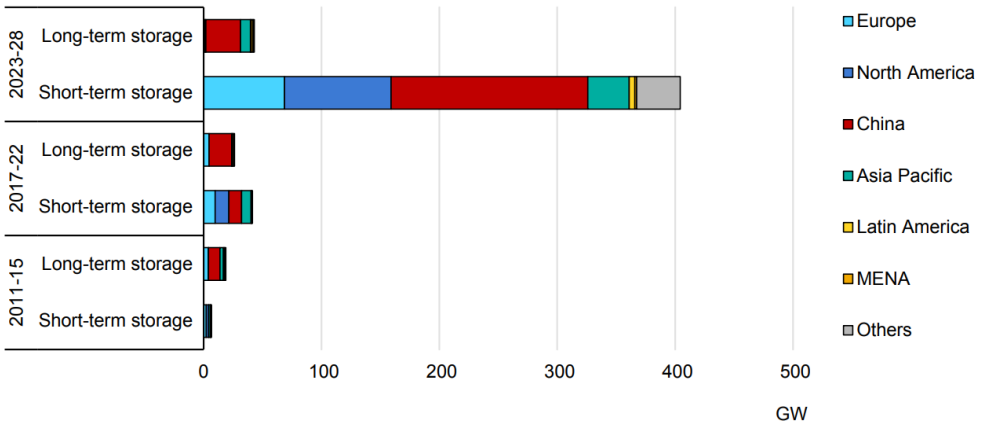

Figure 2.5: Short- and long-term storage capacity growth, 2011-2028 [9].

Electrochemical Batteries

Nowadays, the most widespread storage technology is represented by electrochemical batteries. At the present state, they are the best fitting of al the short-duration storage solutions, meeting all the requirements of size, power density, charge rate and, most of all, costs.

Batteries convert electrical energy to chemical potential energy through redox reactions and store it in electrochemical cells. They can be categorized based on their materials but one of the most common types is the lithium-ion cell battery. In fact, lithium-ion batteries are used in almost everything, ranging from small devices such as mobile phones and laptops to electric vehicles and grid storage [18]. What is more important, however, is that the prices of lithium-ion batteries decreased by 97% in the last three decades, and they are still falling steeply. This great decrease in costs was achieved thanks to the booming of the maket, scaling up of the production capacity and with innovations in the development, as happened with other mass manufactured technologies. In addition to that, energy density experienced a 3.4-fold increase from the 200 Wh per liter of 1991 to over 700 Wh per liter of present days [19]. The decline in prices and increase in installed capacity of lithium-ion batteries during last decades are depicted in Fig. 2.6.

However, chemical batteries are not free from drawbacks. One of them

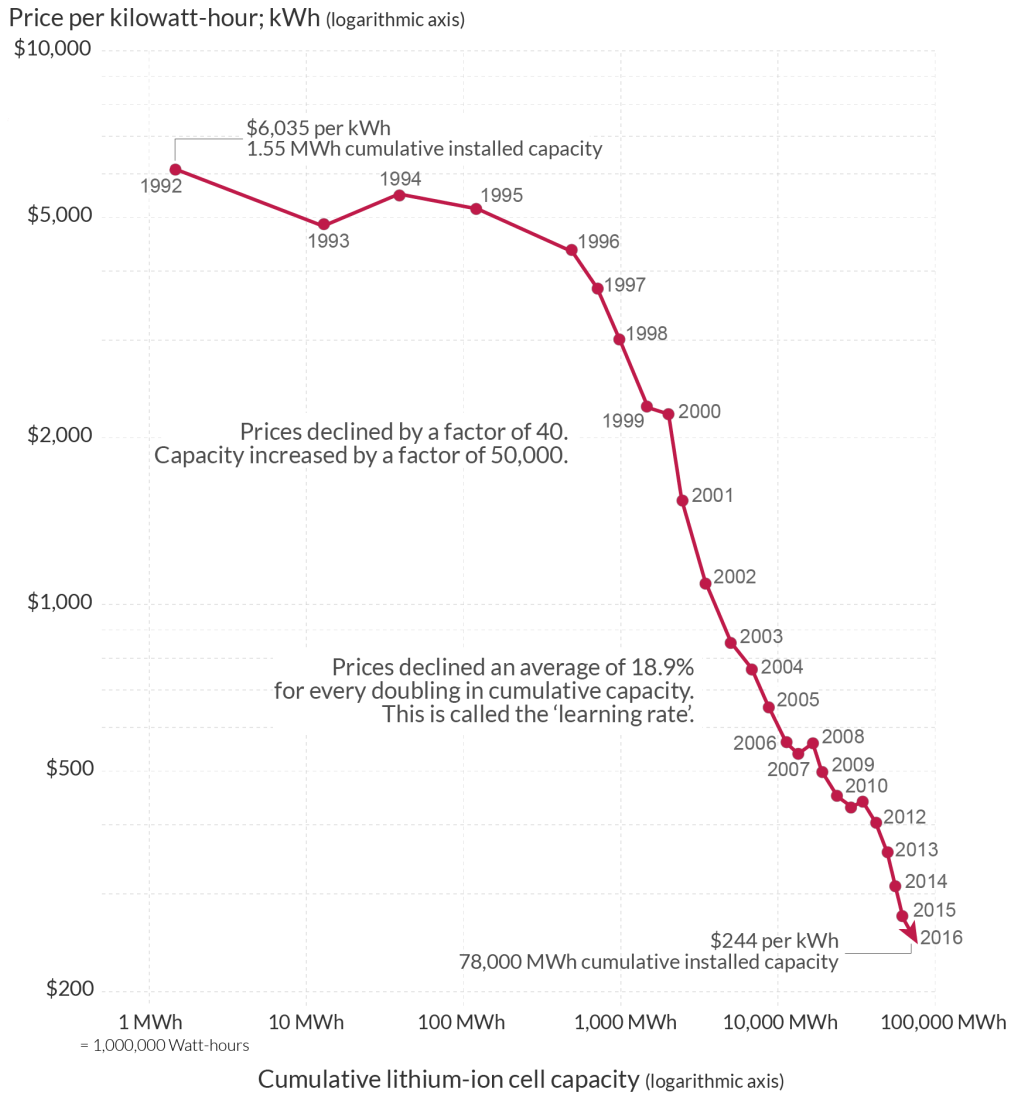

Figure 2.6: Price and market size of lithium-ion batteries since 1992 [20].

is represented by their lifetime: cycle after cycle of charge/discharge, cells degrade, reducing the capacity of electricity storage. But the main problem is represented by the fact that some elements required for their construction depend on critical materials. These raw materials are highly geographically concentrated, thus, present an high risk of supply shocks and constraints. Recently, concerns are raising not only about cost, availability and unavoidable replacement but also about the related environmental footprint and social

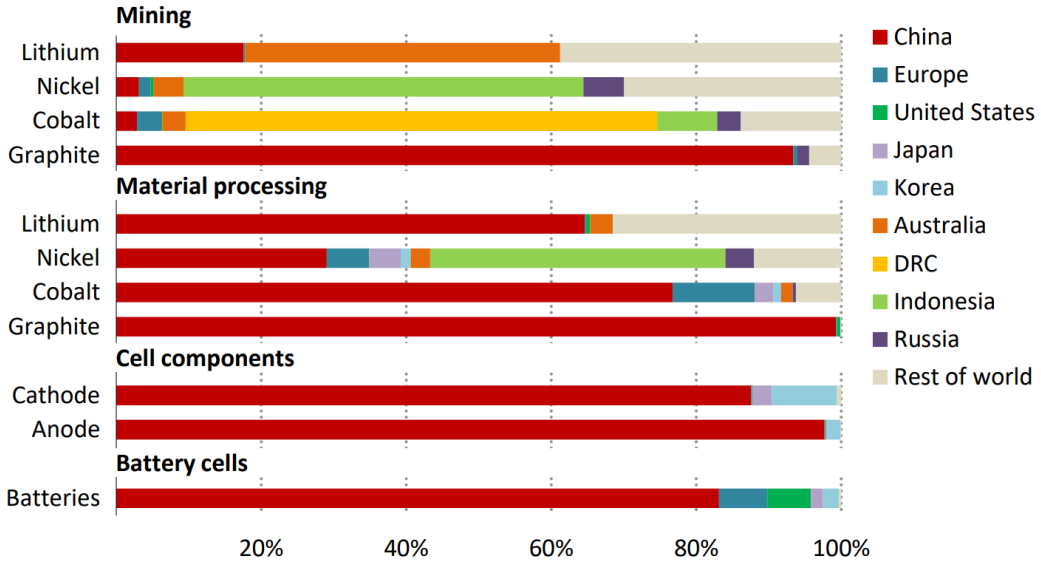

Figure 2.7: Geographical distribution of the global battery supply chain [20].

fairness. Challenges arise not only in supply and extraction of the raw materials but also in their manufacturing. In fact, batteries have a complex supply chain whose stages are dominated by few actors. On total world's production, 90% of graphite production is concentrated in China, 45% of lithium production is concentrated in Australia, 65% of cobalt production is concentrated in the Democratic Republic of the Congo (DRC) and 55% of nickel production is concentrated in Indonesia [21]. Moreover, China dominates all the following steps of material processing, cathode and anode manufacturing and complete batteries construction, as shown in Fig. 2.7.

Battery and EV manufacturers are taking steps to address this challenge by getting directly involved in the production chains, mainly through investment in mines and refineries. In addition to that, material intensity and recycling practices are increasing and efforts are made to decarbonise battery manufacturing in order to reduce battery lifecycle emissions. But, given the rapid scaling up of demand, further efforts needed to ensure a stable and zero-emissions supply of raw materials and production.

Short-duration Energy Storage Alternatives

Other short-term energy storage technologies include supercapacitors, that use electrostatic capacitance instead of chemical redox reactions for storage, and superconducting magnetic storage, where the energy is stored in the magnetic field of a superconducting coil.

Finally, a promising technology that is collecting the interest of the research is represented by flywheel energy storage. Flywheels are energy storage systems that store kinetic energy in a rotating mass couplet to an electric motor. Flywheel batteries are mainly designed for peak shaving in energy distribution systems but they could be a viable alternative to chemical batteries in distributed and residential energy storage applications. The specific features, advantages and drawbacks of flywheel energy storage will be presented in Chapter 3.

Chapter 3

Case Study: Optimization of a Flywheel Battery for Domestic Energy Storage

3.1 Flywheel Energy Storage

3.1.1 Physical Basis and History

A flywheel basically consists of a rotating mass allowing to store energy in the form of kinetic energy. Charging happens by increasing the mass speed by a torque applied in the direction of rotation. The flywheel stays in storage mode by spinning at constant speed. Energy is later extracted by a braking torque that decelerates the mass and produces useful work.

The kinetic energy of a rotating object is given by:

$$E_K = \frac{1}{2} \cdot I \cdot \omega^2 \tag{3.1}$$

with I as the moment of inertia and ω as the angular speed.

Commonly, flywheels are shaped as a uniform disk or a solid cylinder,

whose moment of inertia can be expressed by:

$$I = \frac{1}{2} \cdot m \cdot R^2 \tag{3.2}$$

with m as the mass and R as the outer radius of the flywheel.

The energy density can thus be expressed as:

$$\frac{E}{m} = \frac{1}{4} \cdot v^2 \tag{3.3}$$

with v as the surface speed of the flywheel.

It is convenient to design the flywheels to operate at the highest surface speed allowed by the chosen material. In fact, the rotating flywheel is subject to a stress that must remain below the strength of the material with a suitable safety margin. For a uniform disk or solid cylinder the maximum stress occurs at the center and is given by:

$$\sigma_{max} = \frac{1}{8} \cdot \rho \cdot v^2 \cdot (3 + \nu) \tag{3.4}$$

with ρ as the density and ν as the Poisson ratio of the material [22].

Specific energy expressed in terms of material properties shows that a strong and light material stores more energy per unit mass than a strong but heavy material:

$$\frac{E}{m} = \frac{2}{(3 + \nu)} \cdot \frac{\sigma_{max}}{\rho} \cdot v^2 \tag{3.5}$$

Thus, for example, carbon composite is a more convenient choice that high strength steel.

Since early times, machinery made use of flywheels as a component to smooth the flow of energy. At the very beginning, flywheels were small and human-powered. With the advent of steam engines the 1780s, flywheel saw a rise in size and power, culminating in the massive stationary steam engines of the late 1800s. In engines or industrial equipment, flywheels' purpose is to damp out sudden speed variations caused by pulsed motive source or pulsed load. In fact, even if torque varies significantly, the speed of the flywheel varies little.

It is only in the late 20th century that flywheels developed as standalone systems. Modern flywheels are designed specifically for energy storage and power management. As standalone systems, they can be found in a variety of applications ranging from grid-connected energy management to electromagnetic aircraft launch [23].

3.1.2 State of the Art of the Design

Modern flywheels operate at a much higher speed than industrial times flywheels. In this way, it is possible to maximise the stored energy and make the best use of their material.

As they achieve bidirectional mechanical/electric energy conversion, flywheel energy storage systems (FESS) require both mechanical and electric design. The link between them is represented by a motor/generator that charges and discharges the flywheel electrically, as shown in Fig. 3.1. As for the electric part, FESS are controlled by a power management system connected to the application that it serves. The mechanical part is mainly constituted by the actual rotating mass and the bearings. Along with electric machine design, rotor and bearings design is of the utmost importance to insure the desired performance of the FESS. Finally, the complete FESS is housed in a evacuated or reduced pressure enclosure to minimize aerodynamic drag.

For FESS design, the delivered power and the stored energy can be specified independently. Thus, it is useful to categorize different flywheels in terms of the duration of the output power delivery. In fact, high power but low energy flywheels will provide power for a short time, while lower power and higher energy ones will provide power for a long time. Their design criteria will vary accordingly. In the first case, the machine requires a powerful mo-

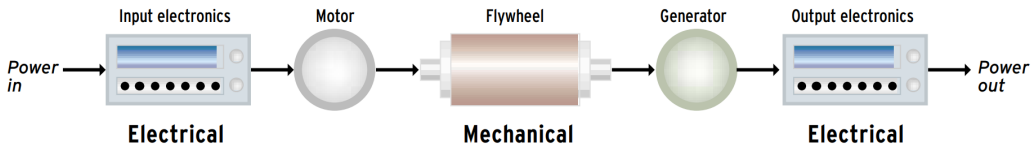

Figure 3.1: Bidirectional conversion of electrical and mechanical energy in a FESS [24].

tor, thus, has to be optimized to minimize motor cost. In the second case, the machine stores much more energy and has to be optimized to minimize rotor cost.

Additionally, while the stored energy is determined by the speed and moment of inertia of the flywheel, the limits on maximum power are actually set by the power electronics converters. Higher power means higher stress on the power devices and larger size for the converter. The progress in high-power devices of recent years, however, paves the way for higher-power flywheel operation. In fact, with high-power devices, fewer individual components are needed and the size of the power converters becomes comparable to the one of the FESS.

Rotor Design

The rotating mass representing the core of the FESS can be integrated into the electric machine rotor or attached to it by a hub and shaft. Rotor design aims primarily at maximizing the stored energy per unit mass. The ideal rotor would be the 'Stodola hub' [25], but this shape is unfeasible in machine design, hence, not used in practice. Thus, common rotor shapes are mainly two and the choice between them depends on the material of construction. If the material is an isotropic one, such as steel, rotors are shaped in solid disks or long, solid cylinders. For an oriented material, on the other hand, the preferred shape is the hollow cylinder.

A trade-off between rotor performance and its simplicity of construction exists. As previously explained, carbon composite rotor offers a really high energy density than steel. However, being an oriented material, an hollow cylinder shape is required. Energy density of steel is much lower, but, being isotropic, rotor can be shaped as a solid disk or cylinder, that are much simpler to construct. Thus, solid metal flywheels are more common than composite flywheels.

Bearings Design

As flywheel rotors' purpose is storing the kinetic energy, they are much heavier than the rotors of common electric machines operating at comparable speed. In addition to that, thermal management and lubrication are difficult because FESS operate in a vacuum chamber. Thus, bearings requirements for FESS are stricter than usual. Bearings support the flywheel rotor while allowing it to spin freely, reducing mechanical losses. Usually, they represent the life limiting element in FESS design. In fact, the need to support the a greater weight leads to the use of larger bearings whose lifetime is shorter than smaller bearings. In addition to that, drag losses are higher [23].

Bearings types for FESS are mainly two: ball bearings and active magnetic bearings. Ball bearings are a simple and common solution, but their performance and lifetime is quite low for FESS applications. As active magnetic bearings levitate and actively position the rotor, they are free from contact and therefore free from wear. They are an advantageous choice to meet the life and load requirements of flywheels, but they are more expensive and complex. Often, both bearings types are used in conjunction. This reduces load on the ball bearings improving their life and allowing the use of smaller bearings.

Most of the time, standalone FESS are built using a vertical spin axis to manage bearing loads and simplify the levitation system design. An example of the structure and components of a complete FESS is presented in Fig. 3.2.

Electric Machine Design

For FESS applications, different choices of electric machine types have been explored including homopolar, synchronous reluctance, induction, and many types of permanent magnet machine. In fact, application-specific design of the machine is of the utmost importance to obtain satisfying performance and make FESS a competitive solution. Thus, the selection of a motor type is dictated by a number of different considerations.

As for the thermal aspects, a goal of flywheel motor design is to minimize

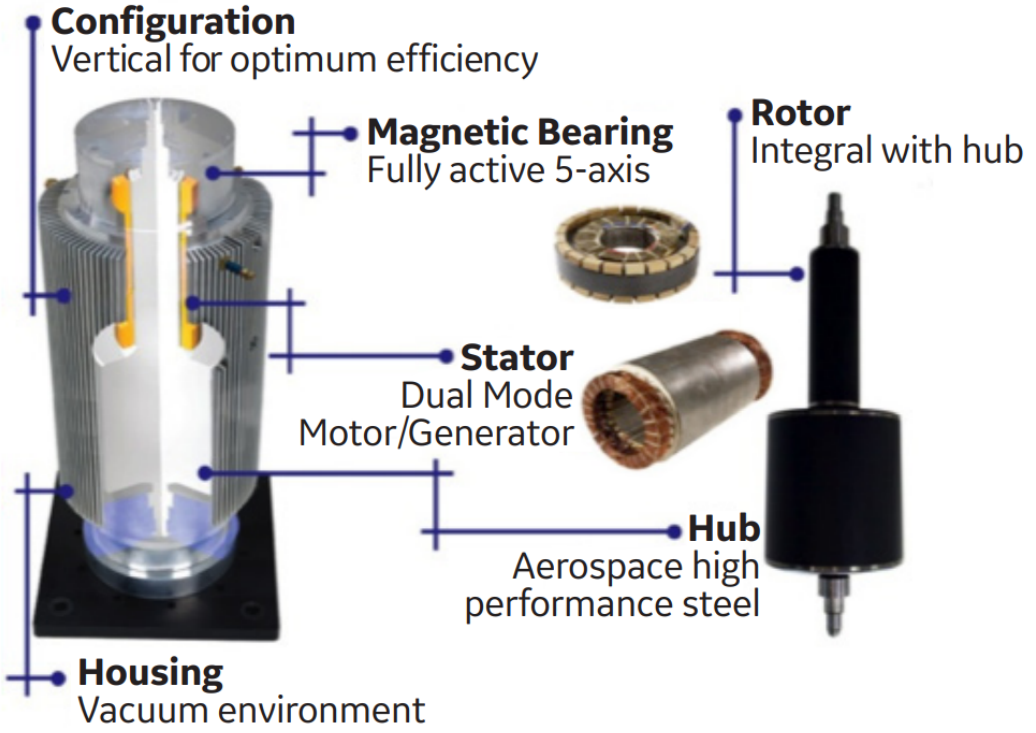

Figure 3.2: Structure and components of a vertical spin axis FESS [26].

heat dissipated in the rotor. In fact, being housed in a vacuum chamber, thermal management of the machine is more difficult. Heat removal occurs only through radiation from the rotor to the housing and can be ineffective. This is especially true for FESS applications with frequent cycles. In this case, design for low on-rotor loss is critical and permanent magnet machines are usually used.

The most important aspect in machine design, however, is to ensure that the self-discharge duration time is sufficiently high for energy storage applications. Self-discharge duration time is defined as the amount of time in which the system is able to actually keep the stored energy if disconnected from the source and the load. This means, in practice, that the rotating flywheel must keep on spinning without slowing down as long as possible. In order to increase this storage time, all losses in the electric machine must be minimized. Additionally, this is required to obtain a satisfying efficiency in energy conversion.

Loss sources can be divided in mechanical and electromagnetic. Mechanical sources are represented for example by ventilation effects due to friction with air and friction in mechanical transmission components. The former are addressed by sealing the entire system in a vacuum container, the latter are minimized by the use of bearings. Electromagnetic loss sources are represented by Joule losses in the windings, losses in the permanent magnets and in the iron core. Iron core losses, especially, are the most impacting ones when the FESS is in storing mode and the machine is not fed by the supply current. In order to minimize these loss sources, a proper choice of the electric machine type and is optimal design are mandatory.

Additional aspects regarding electric machine design for FESS will be treated more in detail in the following sections. Moreover, an electric machine prototype specifically designed and realized for FESS application will be presented.

3.1.3 Advantages and Drawbacks

For energy storage systems, the cost of a certain technology is evaluated over its lifetime. Among the many criteria for the selection of one energy storage technology over another, cost surely represents the deciding factor.

Cost drivers for flywheel systems are spread out over three main cost subsystems that scale differently with energy and power. Those that scale with the stored energy are the costs of the rotor, the bearings, the housing, and structural hardware, as rotor weight increases with the storage capacity. The costs that scale with the power are the ones of the motor itself, the motor drive train and the electrical equipment. Finally, costs of other equipment such as vacuum pump, sensors, telemetry, diagnostics, controls and operation components do not scale with energy or power. FESS are gaining attention for the same types of applications usually served by conventional electrochemical batteries, supercapacitors or superconducting magnetic energy storage (SMES). Of course, keeping the coil at cryogenic temperature itself consumes energy, which is one reason why SMES systems are not considered suitable for long-term energy storage

As previously mentioned, chemical batteries costs have steeply decreased in the previous years and this technology represents the de facto standard for low cycle applications, such as EV. Technological advances in fibers, resins, composite manufacturing techniques, and manufacturing quality control have made it possible to realize flywheels that operate reliably at high speed, thus, with an increased density of energy storage. [24]. Notwithstanding these improvements in technology and manufacturing chain, FESS are highly unlikely to achieve the same incremental energy cost [23]. Moreover, FESS energy density remains lower than for chemical batteries. But it is in applications requiring many cycles and a calendar life of decades that flywheel can compete with the other energy storage solutions such as batteries, supercapacitors and SMES.

In fact, FESS leading advantages are the really long lifetime and their high robustness to charge/discharge cycles degradation. In fact, many studies aimed at assessing and improving the mechanical strength and resistance to fatigue cycles can be found in literature [27], [28]. Differently from chemical batteries, flywheel life is almost independent of the depth of discharge and they can work both on very deep discharges and on frequent shallow discharges with same performances. Power ratings are limited by the power electronics and not on the electrochemistry. On the other hand, this load variability is challenging for chemical batteries as it makes their design difficult to optimize.

Moreover, FESS show advantages also in terms of power and discharge time. Differently from batteries, FESS are more capable to manage sudden peaks in input or output power. Thus, flywheels are a cost effective solution for applications requiring power for more than several seconds and up to several or tens of minutes, particularly when high cycle life is required. Additionally, the state of charge of a flywheel battery is easily determined from its rotational speed while determining its value for an electrochemical battery is more difficult. Finally, while chemical batteries depend on highly critical and geographically concentrated materials, FESS materials are cheap and more readily available, and their environmental footprint is lower.

Still, when it comes to applications requiring long storage times, chemical

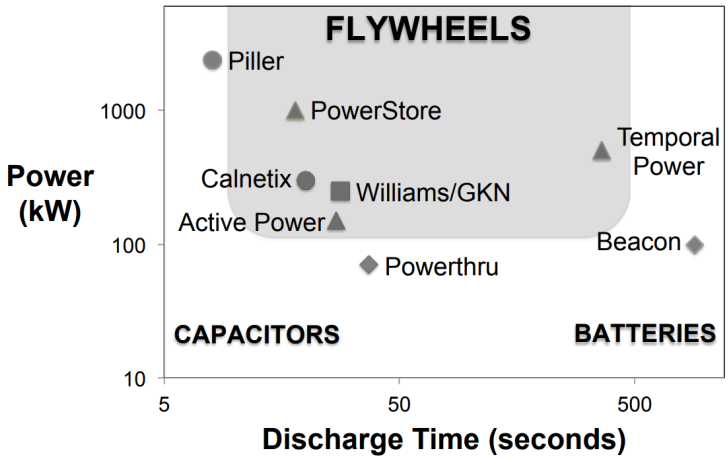

Figure 3.3: Application regions where flywheels, capacitors, and batteries are most cost effective [23].

batteries remains the reference solution. SMES systems are not considered suitable for long-term energy storage because keeping the coil at cryogenic temperature itself consumes energy. Storage time for FESS is lower than for batteries, but efforts in design can be made to increase their self-discharge duration time, as it will be later exposed. The application regions where batteries, supercapacitors and flywheels are most cost effective can be located in terms of required lifetime and discharge time, as shown in Fig. 3.3.

3.1.4 Modern Applications

Being more cost effective than other competing solutions is not enough to guarantee widespread deployment of a technology. In fact, a market must exist to ensure that the adoption of that technology result in an economic return. Currently, flywheels represent a cost competitive and economically effective solution in some applications such as grid connected, industrial and commercial power management but also pulsed power, uninterruptible power supplies and mobile applications.

In grid connected power management, FESS are adopted for frequency regulation and control of power peaks caused by fluctuating renewable generating resources. The electric grid must work at a frequency as constant as possible to ensure that the generators of electric plants remain synchro-

	VRLA BATTERY PLANT	GE FLYWHEEL
Embedded Carbon Emmissions (CO_2/kg)	1.14	2.70
Energy Storage for 1MW UPS	6 Cabinets/Strings	4x300kw Flywheels
Total Energy Storage Weight (kg)	14,693	1,297
Total Embedded Carbon (kg CO_2)	16,750	5,502
15 Year Energy Storage Replacement	3 Times	0 Times
Total 15 Year Lifecycle Embedded Carbon (kg CO_2)	67,000	3,502

Figure 3.4: Carbon footprint comparison between of flywheel UPS and chemical battery UPS [26].

nized. Otherwise, a widespread power outage may occur. For instance, if the load increase is faster than a turbine generator's response time, the generator slows down, momentarily operating at lower frequency. Similarly, renewable energy generation might produce sudden power fluctuations that vary considerably in frequency, severity and duration. Thus, energy storage plants are specifically installed to provide the ancillary service of frequency regulation and peak shaving. FESS already represent a mature technology when used in plants for grid stability management. For example, Beacon Power LLC $20MW$ Stephentown plant provides almost 10% of New York's overall frequency regulation needs [29]. Moreover, thanks to their fast time response, FESS are well suited for mitigating the frequent, short-duration power fluctuations inherent in wind generated electricity. Grid management applications are located on the utility side of the electric meter. Hence, a market for energy storage solutions can be created by a regulatory agency only.

Industrial and commercial power management applications, on the other hand, are located on the customer side of the electric meter. Hence, the market for power management solutions is less regulated. In this sector, FESS are adopted to retrieve regenerated electricity that would otherwise be lost and provide high peak power for short duration in case of need. Thanks to its capacity to collect energy at a steady rate and release it rapidly with a high power into the application, FESS are well suited for cyclic power profiles that produce regenerated electricity, such as mining, but also pulsed power industrial applications, such as aircraft and roller coaster launch. For example, the Joint European Torus (JET), Oxfordshire, England requires

power pulses of more than $1000MW$ and is equipped with two flywheels. During a $20s$ shot, each flywheel can discharge $700kW$ h of energy at a peak power of $500MW$ [30]. FESS can be used, for example, in train stations to capture the regenerative braking energy and use it later to accelerate the train as it leaves its stop [31]. FESS are a mature technology for Uninterruptible Power Supplies (UPS). During some possible power outages, critical facilities require a load support system until backup diesel generators can be brought up to speed. Thanks to their fast response time and much longer service life, FESS directly compete with batteries in this application. A comparison between battery and flywheel UPS systems, with a particular focus on their carbon footprint, is provided in Fig. 3.4. Flywheel based UPS can reduce the total carbon footprint by 95% when compared with chemical battery based UPS. Another successful application for FESS is mobile i.e. where the flywheel is installed in a vehicle. As previously mentioned, flywheels are well suited for applications where load duration is short and repeated frequently, such as cranes. Thus, FESS are efficiently employed also on rubber tired gantry cranes that operate and move in container terminals around the world are powered by an onboard diesel generator [32], helping to reduce their fuel consumption. Moreover, FESS have been included in hybrid powertrains to improve fuel efficiency in motorsport, reducing the number of pit stops [33]. Finally, flywheels have been used on spacecrafts throughout the history of space flight. They are implemented as reaction wheels for precision rotation and stabilization of the spacecraft or as Control Moment Gyros (CMGs) to produce large steering torque with very little power. In both cases, they allow to replace limited propellant consumption to inexhaustible solar power use [34]. Additionally, they can also be employed as energy storage devices [35]. This FESS technological background and knowledge derived from spacecraft can be readily adaptable to terrestrial uses.

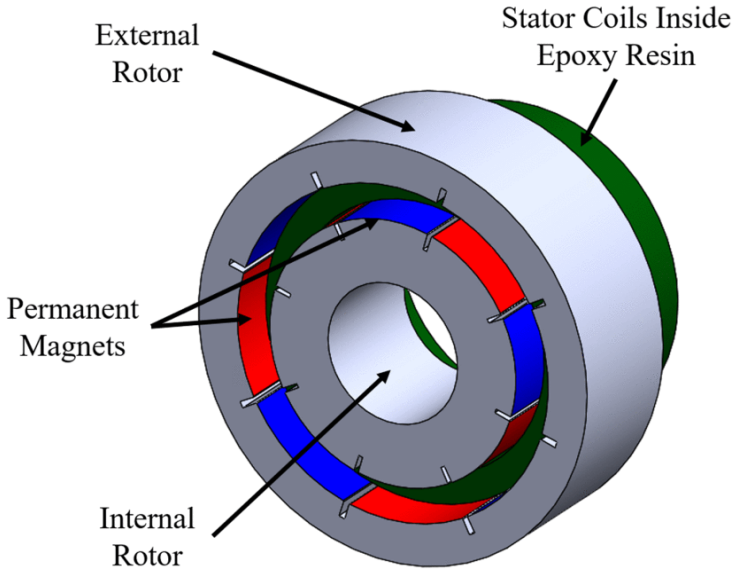

Figure 3.5: MechSTOR's dual rotor topology [36].

3.2 Electric Machine Design

3.2.1 MechSTOR Prototype

Being the central energy conversion device, the electric machine coupled to the flywheel plays a key role in FESS. Hence, its optimal and application specific design is of the utmost importance to ensure the profitability of this energy storage system.

As previously exposed, FESS are already a mature technology in case of grid frequency regulation, power management, UPS and other damping and short-time energy storage applications. In these cases, FESS are designed to manage sudden and high energy peaks hence, the currently achievable value for the self-discharge duration time is enough. FESS, however, might represent an interesting alternative to chemical batteries for longer storage times applications. The idea is to extend their field of application as standalone systems on a domestic level. For example, a small size FESS could be used in combination with a photovoltaic system for a typical residential user, replacing the role currently served by chemical batteries. The profitability in terms of energy and cost savings for the end user largely depends on the optimal

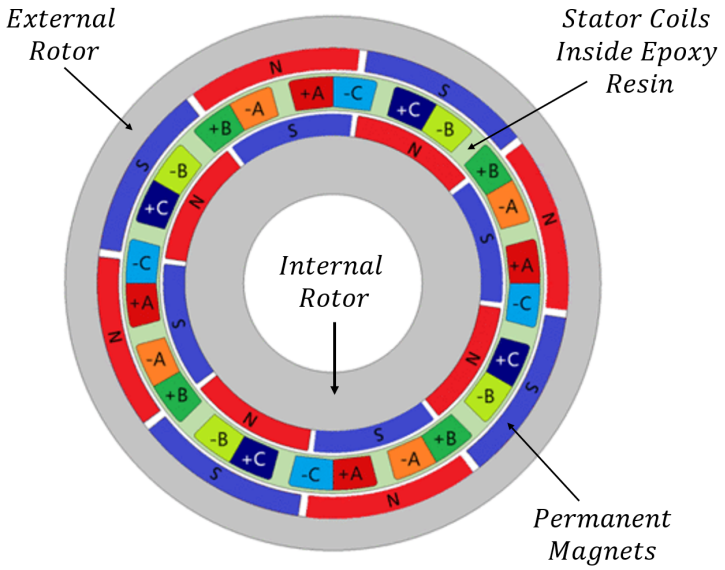

Figure 3.6: Slots and windings scheme of MechSTOR [36].

sizing of the system, on the effective control of the power flow and, most of all, on the dedicated design of the electric machine. The machine must feature high efficiency, low losses and system performances should be preserved also in case of fault. Specifically, self-discharge duration time must be increased. In fact at least a few hours of self-discharge duration are required to match requirements for renewable energy time shift.

In order to increase self-discharge duration, all losses must be minimized. The loss sources can be divided in mechanical and electromagnetic. Mechanical sources are associated with the rotor motion and are mainly due to friction in mechanical transmission components (e. g. bearings), possible imperfections such as misalignments and/or excessive clearance in joints, and partly due to ventilation effects. The electromagnetic sources concern the electric machine structure and consist of Joule losses in the windings, permanent magnet losses and iron core losses. The latter ones, especially, are the most impacting ones when the FESS is in storing mode, i.e. it is disconnected from the supply and the load. In this case, the flywheel must keep on spinning at constant speed and this operation mode can be referred to as idling. An iron-core brushless surface permanent magnet could be a

nice option for its high efficiency, however at high speeds, it is prone to high core losses and eddy currents that result in self-braking effect during storing mode. One solution to avoid the shortcomings linked to core losses could be represented by with a pure reluctance machine or an ironless machine.

By following this idea, an ironless electric machine prototype, named MechSTOR, was specifically designed and realized. The prototype was optimized for a flywheel energy storage at household level and compared with two reference machines with identical size and torque: an iron-core brushless surface permanent magnet machine and a pure reluctance machine. Results show that MechSTOR self-discharge duration time is higher than the one of the other two reference machines [36]. The ironless solution was already proposed for FESS with different configurations [37], [38], [39]. Ironless machines, however, present an increased reluctance of the core as a drawback, and this affects their energy density and efficiency. For this reason, a dual-rotor topology was chosen. In this way, it is possible to reduce the reluctance of magnetic paths and minimize magnetomotive force drops. The resulting topology consists of two concentric circular structures with surface mounted permanent magnets. Stator coils are encapsulated in epoxy resin and placed between the rotors, as shown in Fig. 3.5. The windings have a fractional-slot, double layer arrangement following a 12–8 slot–pole combination, as shown in Fig. 3.6. The machine was designed for a $3kW$ rated power and $9000rpm$ rated speed and its geometrical parameters are summarized in Table 3.1. Even if higher speed would allow a higher energy density, rated speed was limited to this value because of other design constraints such as cost and safety.

In the following, further investigations regarding fault tolerance, vibration analysis and possible power converter configurations for MechSTOR will be exposed

3.2.2 Multiphase Configurations

A previously cited, MechSTOR has a 12-8 slot-pole configuration. This solution allows to configure the machine as 3-Phase, 6-Phase and 12-Phase

Table 3.1: Geometrical Parameters of MechSTOR

Parameter	Value
Outer Rotor External Diameter	150 mm
Outer Rotor Internal Diameter	132 mm
Inner Rotor External Diameter	82 mm
Inner Rotor Internal Diameter	55 mm
Lamination Stack	50 mm
Stator Slots	12
Poles	8
PM Volume	$2.3 \cdot 10^{-4}$ m^3

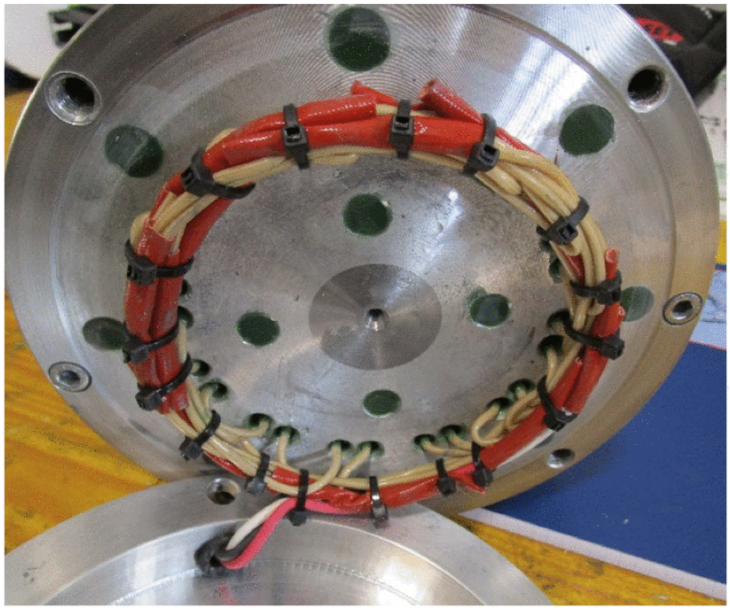

Figure 3.7: MechSTOR coil connections at the rear flange [36].

without rewinding the stator coils [36]. In fact, the end windings of each coil are connected outside the rear flange to allow different series or parallel connections (from zero to four parallel connections) as shown in Fig. 3.7. As it will explained in the following, however, it may be convenient to rewind the stator coils in order to maintain the same total number of conductors of a phase as in the 3-Phase configuration.

Multiphase solutions have a series of advantages such as greater efficiency, lower power per phase, higher torque density, reduced torque pulsation and

higher fault tolerance [40]. This last feature is especially important for applications where high reliability is demanded, such as FESS. Hence, MechSTOR can be reconfigured to allow higher fault-tolerance.

In addition to that, MechSTOR already features an intrinsic fault-tolerance. In fact, because of the ironless core, the armature reaction in case of fault will be more limited and the magnetic field at the air gap will suffer less distortion. For this reason, radial forces caused by unbalanced magnetic forces will be lower than in iron-core solutions. Limiting these forces is really important because, in the final application, the machine will use high performance bearings or magnetic bearings, which are strongly affected by radial forces. In MechSTOR, also the mutual coupling between phases is lower because, with an ironless core, the linked fluxes between phases must cross high reluctance paths of air and PM. Hence, a fault in a single phase will have a lower effect on the other phases. The mutual coupling between the phases is further decreased because a concentrated winding was adopted.

However, this lower value for the mutual coupling causes a lower overall value for the phase inductances and, hence, a lower filtering capability for the supply current. For this reason, in order to reduce the torque ripple to reasonable limits, large size filtering inductors are required and, most of all, a quite high switching frequency. The higher the switching frequency, the higher the switching losses of the diodes and IGBT of the inverter controlling the motor. As it will be shown, multiphase configuration help increase the value of phase inductances and, hence, reduce torque ripple without increasing too much the switching frequency.

In order to assess the convenience of multiphase configurations for MechSTOR, phase faults were modeled in case of 3-phase, 6-phase and 12-phase configuration with Finite Element Method Magnetics (FEMM) [41]. Joule losses were chosen as a benchmark for performance comparison in the different cases. In fact Joule losses in the windings are the main loss component for MechSTOR. As previously explained, core losses for MechSTOR are negligible thanks to the ironless structure. In addition to that, the final system will be sealed in a vacuum container and will use high performance bearings, hence, mechanical losses are minimized too. Moreover, Joule losses are

heavily affected by phase faults in the machine. Hence, Joule losses represent a fair benchmark to compare the performances of different multi-phase configurations in faulty conditions.

In case of a phase fault, the motor will draw more current in the remaining connected phases. As a consequence, more current is required by the machine to develop the same torque, leading to an increase in Joule losses. Hence, the performance of the FESS in terms of final energy savings will be lower.

Multiphase configurations are more fault-tolerant as the number of coils involved in the fault decreases with the number of phases of the configuration. Thanks to the remaining connected phases, the machine will be able to work even under faulty operating conditions.

Two kind of faults were considered: open circuit of a phase (OC) and short circuit of 5% of the coils of a phase (SC). For each of these two fault types, loss computation via FEMM was repeated for all of the three multiphase configurations. Hence, simulation were performed for the following cases:

- Healthy machine;
- Phase OC in the 3-Phase configuration;
- Phase OC in the 6-Phase configuration;
- Phase OC in the 12-Phase configuration;
- Phase SC in the 3-Phase configuration;
- Phase SC in the 6-Phase configuration;
- Phase SC in the 12-Phase configuration;

In healthy conditions Joule losses are mainly proportional to the input current, i.e. to the developed torque. In faulty conditions, phase current may be affected by speed, hence, Joule losses may also be dependent on the speed. Thus, losses were estimated from the model for different torque and speed values.

In the following, fault modeling in FEMM of each fault in the different configurations will be explained.

Phase Open Circuit Modeling

In phase OC, the open-circuited conductors will carry no current. As a consequence, the remaining healthy conductors will draw additional current to develop the same torque, leading to an increase in Joule losses.

OC faults were modeled in the different multiphase configurations, by changing the coefficients of Phase C in the slot matrix (Table 3.2).

The generic element k_{qj} of the slot matrix indicates how much the q–th slot is filled by conductors of the j–th phase:

- $k_{qj} = 1$ means that the q–th slot is completely filled by conductors of the j–th phase;
- $k_{qj} = 0.5$ means that only 50% of the q–th slot is filled by conductors of the j–th phase;
- $k_{qj} = 0$ means that no conductor of the j–th phase is in the q–th slot;
- The sign of k_{qj} indicates the direction of the current.

Each coil has two sides and therefore two coefficients in the slot matrix. Hence, open connected coils can be simply represented by a value '0' in the corresponding two slots. MechSTOR is a fractional-slot machine with double

Table 3.2: Phase Open Circuit Modeling with Slot Matrix

q	k_a	k_b	k_c			
			Healthy	**OC - 3ph**	**OC - 6ph**	**OC - 12ph**
1	0.5	0	-0.5	0	0	0
2	-0.5	0.5	0	0	0	0
3	0	-0.5	0.5	0	0.5	0.5
4	0.5	0	-0.5	0	-0.5	-0.5
5	-0.5	0.5	0	0	0	0
6	0	-0.5	0.5	0	0	0.5
7	0.5	0	-0.5	0	0	-0.5
8	-0.5	0.5	0	0	0	0
9	0	-0.5	0.5	0	0.5	0.5
10	0.5	0	-0.5	0	-0.5	-0.5
11	-0.5	0.5	0	0	0	0
12	0	-0.5	0.5	0	0	0

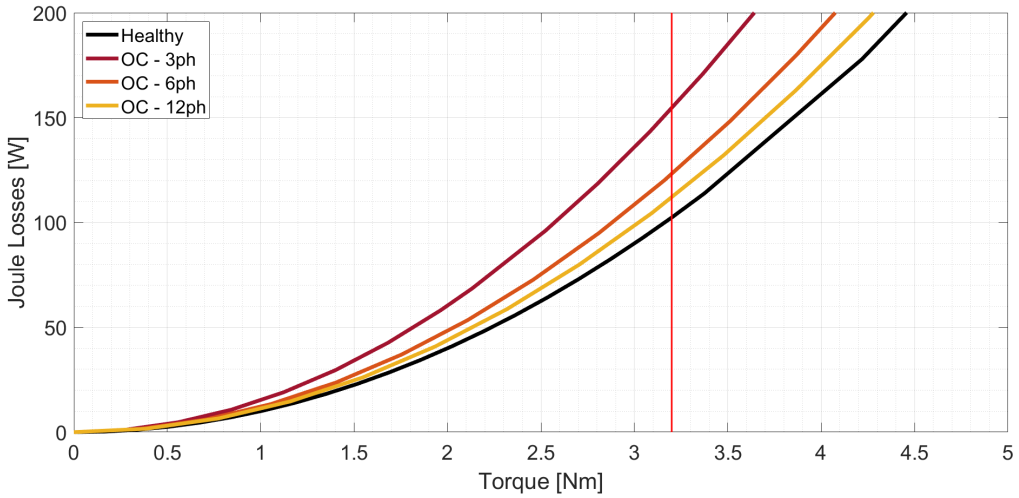

Figure 3.8: Joule losses as a function of the developed torque in different scenarios: healthy machine (black), OC in 3-Phase configuration (red), OC in 6-Phase configuration (orange) and OC in 12-Phase configuration (yellow). The red vertical line represents the machine's torque limit [41].

layer windings, hence, the remaining coefficients of the matrix are set to '0.5'. As previously explained, with increasing number of phases, the number of open connected coils (slot with '0' coefficient) decreases. The multiphase configuration of MechSTOR is derived by the conventional 3-phase winding by splitting the number of coils of each phase. Hence, in case of fault in 3-Phase configurations, all Phase C slots coefficients are set to '0'. In case of 6-Phase configuration, only four slot coefficients are set to '0'. Finally, for 12-Phase configuration, the slots coefficients set to '0' are only two.

Fig. 3.8 shows the Joule losses as a function of the torque in the four cases. The red vertical line is placed in correspondence of the maximum torque of the machine. As expected, Joule losses for the 3-Phase configuration are higher, but the difference between all configuration is small for low T values.

Phase Short Circuit Modeling

The modeling of a short circuit of a phase is less straightforward than the OC case and requires some assumptions. As explained previously, thanks to the ironless core, the machine phases can be represented as a pure resistance series connected with an ideal generator representing the Back EMF (BEMF),

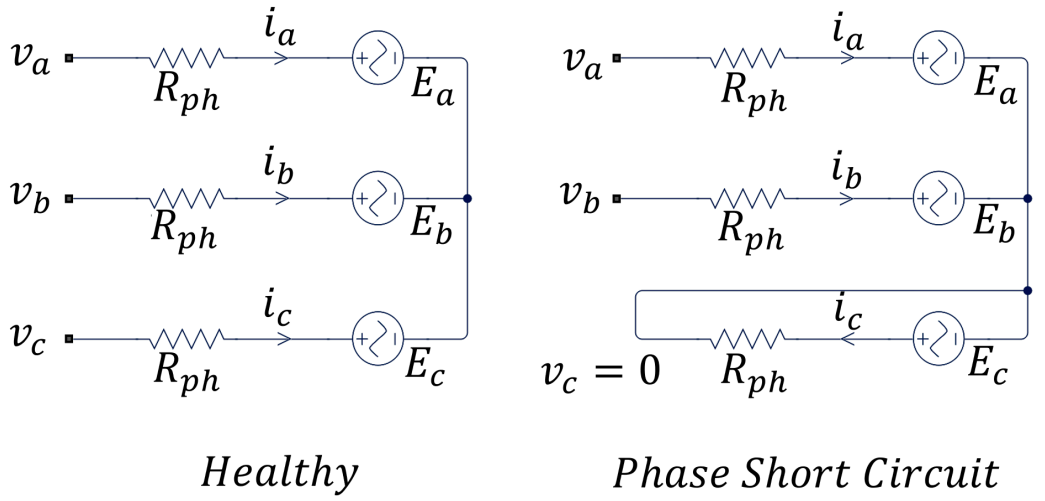

Figure 3.9: Equivalent circuit model of the stator in healthy conditions (left) and in case of short circuit of Phase C (right) [41].

as shown in the equivalent circuit model of Fig. 3.9. When motoring, the direction of the current in the SC phase is opposite to the current in the other healthy phases because the faulty one acts as a generator. As a consequence, the torque in the faulty phase is opposite to the other phases, decreasing the total torque value. Thus, the conductors in the healthy phases shall draw even more current than in OC case to develop the same torque. Specifically, the amplitude of the short circuit current will be:

$$i_c = E_c / R_{ph}, \tag{3.6}$$

where R_{ph} is the phase resistance and E_c is the BEMF of Phase C, that is proportional to the machine electric speed ω_e. Hence, i_c and Joule losses are proportional to machine speed. For this reason, Joule losses P_{Cu} in case of Phase SC fault will be proportional both to the developed torque and to the speed:

$$P_{Cu} \propto T, \omega_e. \tag{3.7}$$

As the short circuit current i_c is pretty high, the loss component proportional to ω_e (caused by the faulty phase) is dominant over the loss component proportional to T (caused by the remaining healthy phases). This is espe-

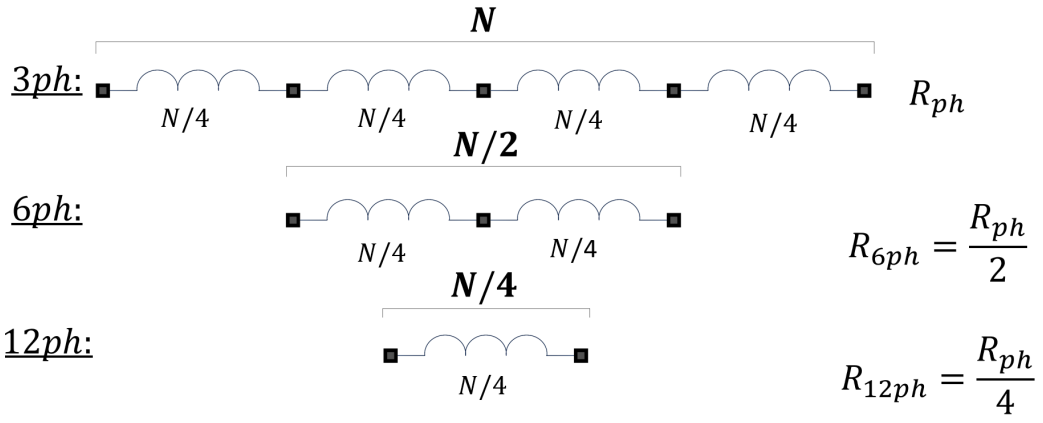

Figure 3.10: Option 1: Realizing the multiphase configuration by parallel connections. N is the number of conductors for a phase in the standard 3-Phase configuration. R_{ph},R_{ph6} and R_{ph12} are the phase resistances in the 3-Phase, 6-Phase and 12-Phase, respectively [41].

cially true when the machine is in idling time where T is low. Hence, the dependence of P_{Cu} from T was neglected, and losses were computed as a function of speed only.

In fact, at high speed, the short circuit current reaches critical values. As MechSTOR phases can be represented as purely resistive, there is no inductive component limiting i_c. The short circuit current keeps on increasing linearly with the BEMF and the speed, as in (3.6). In order to decrease this high current value, two options were considered to realize the multiphase configuration:

- Option I: reconfigure the stator windings by utilizing the parallel connections;
- Option II: rewinding the stator coils.

Option I is less expensive and complex, but features some drawbacks. With this choice, the total number of conductors of a phase decreases as shown in Fig. 3.10). E. g. for 6-Phase configuration, the BEMF and resistance of a phase consequently halves, while the short circuit current remains the same, for (3.6).

With Option II, on the other hand, it is possible to maintain the same total number of conductors of a phase as in the 3-Phase configuration as

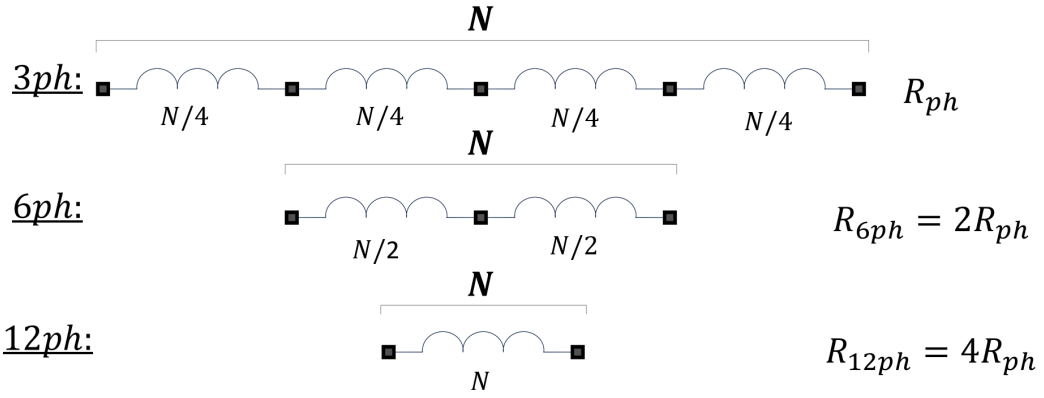

Figure 3.11: Option 2: Realizing the multiphase configuration by rewinding the stator coils. N is the number of conductors for a phase in the standard 3-Phase configuration. R_{ph},R_{ph6} and R_{ph12} are the phase resistances in the 3-Phase, 6-Phase and 12-Phase, respectively [41].

shown in Fig. 3.11). In order to do that, the number of conductors per slot must increase leading to a decrease of the coil conductor section. Hence, for 6-Phase configuration, the BEMF remains the same and the resistance of a phase doubles, because the conductor section halved. The short circuit current, conversely, halves.

At high speed, the short circuit current may reach unacceptable values

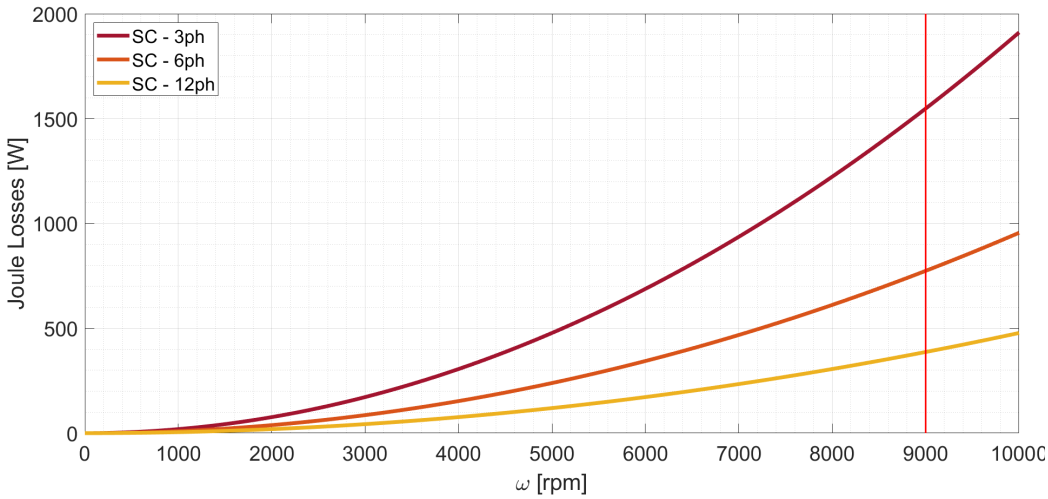

Figure 3.12: Joule losses as a function of the mechanical speed in different scenarios: SC in 3-Phase configuration (red), SC in 6-Phase configuration (orange) and SC in 12-Phase configuration (yellow). The red vertical line represents the rated speed [41].

that could lead to overheating, hence, Option II may be more convenient even if it requires a stator coils rewinding. With this choice, devices and connectors with lower current rating can be selected for the coupled inverter.

Regardless of the connection option, Joule losses in the three multiphase configurations are:

$$P_{Cu,3ph} = i_c^2 \cdot R_{ph} = E_c^2 / R_{ph}, \tag{3.8}$$

$$P_{Cu,6ph} = (i_c/2)^2 \cdot 2 \cdot R_{ph} = P_{Cu,3ph}/2, \tag{3.9}$$

$$P_{Cu,12ph} = (i_c/4)^2 \cdot 4 \cdot R_{ph} = P_{Cu,3ph}/4, \tag{3.10}$$

Hence, joule losses can be computed as a function of ω by simulating BEMF values at different speeds with FEMM.

Phase SC is a more severe condition than phase OC and the corresponding loss are extremely high. The complete short circuit of a phase is an unacceptable condition. Hence, for this analysis, a short circuit of 5% of a phase coils was considered. Consequently, Joule losses are 5% of the full phase SC losses.

Fig. 3.12 shows the Joule losses in case of SC of 5% of a phase coils as a function of the mechanical speed. The loss values are really high even if only a small fraction of the phase coils are in short-circuited.

As visible, multiphase solutions guarantee an higher tolerance to faults and are higly beneficial in terms of losses reduction. They require, however, also a higher complexity for the coupled inverter. The number of devices and legs of the inverter depends on the number of phases. In order to allow an independent control for each phase, each leg requires a distinct gating signal and current sensors. Hence, PWM modulation and sensing becomes more complex. For this reason, the profitability of multiphase reconfiguration must be evaluated in view of the specific FESS application.

In case of open circuit fault, multiphase configurations might not provide significant improvements with respect to conventional 3-Phase connection. When used as a standalone storing device for residential application, FESS follows some typical daily cycles, as it will be shown in detail in the following sections. During its daily cycles, the electric machine works mostly in storing

mode, hence, with low torque values. High values of torque are requested only in the charge and discharge intervals. As visible in Fig. 3.8, for low torque values, Joule losses in faulty conditions are similar for all multiphase configurations. Hence, on average, the total amount of Joule losses in case of OC fault would be similar between all the configurations. For this reason, re-configuring the machine as multiphase is not essential for OC faults. MechSTOR shows a very low mutual and self inductance between the phases which leads to an intrinsic good fault tolerance in case of OC fault.

On the other hand, in case of short circuit, Joule losses becomes dependent on the speed. At high speed, especially, multiphase configurations would allow a significant losses reduction with respect to 3-phase configuration, as visible in Fig. 3.12. That is because short circuit of a phase is a more severe condition than open circuit, hence, Joule losses are appreciably increased. This is especially important because the machine would work most of the time in storing mode at high speed. Hence, he advantages would outdo the drawbacks of the additional inverter complexity.

Torque Ripple in Multiphase Configurations

In MechSTOR, the linked fluxes between phases must cross high reluctance paths of air and PM, hence, the mutual coupling between phases is lower. In addition to that, because of the concentrated winding, the mutual coupling is even lower than in the case of a distributed winding. For this reason, the overall value of the phase inductances will be lower.

Phase inductance computation for a machine with a distributed winding in the three multiphase configurations is schematized in Fig. 3.13. For a distributed winding machine, the value of the phase inductances is the same regardless of the multiphase configuration.

For a machine with a concentrated winding, instead, the term relative to the mutual coupling is negligible and can be removed, as presented in Fig. 3.14. In this case, the value of phase inductance is higher for multiphase configurations, being double for 6-Phase and quadruple for 12-Phase configuration.

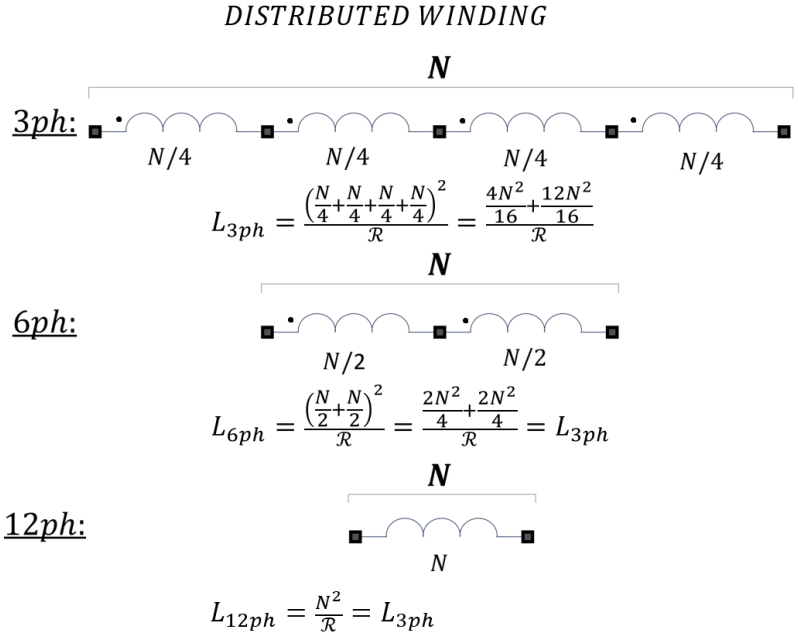

Figure 3.13: Phase inductance computation as a function of the number of conductors per phase for distributed winding machine.

The values of phase inductances for MechSTOR in the three multiphase configuration were computed with FEMM and are displayed in Table 3.3.

A lower value for the phase inductances means a lower filtering capability for the supply current. This causes a higher ripple in the developed torque. For this reason, the addition of large filtering inductors is required. As known, large size inductors are expensive and of difficult fabrication in integrated circuits. Alternatively, an high switching frequency could be used to reduce the torque ripple. This, however, causes an increase in switching losses as they are directly proportional to the switching frequency. The impact of switching losses may become, in this case, quite relevant.

Table 3.3: MechSTOR Phase Inductances Values in Different Multiphase Configurations

Configuration	Synchronous Inductance
3-Phase	3.9 mH
6-Phase	7.8 mH
12-Phase	15.6 mH

MechSTOR was modeled in PLECS in its three multiphase configurations with the corresponding computed values of the phase inductances. No filtering inductor was included in the PLECS model in order to assess the effect of phase inductances only. Then, the developed torque was simulated for different switching frequencies.

Fig. 3.15, Fig. 3.16 and Fig. 3.17 show the simulated torque ripple for different switching frequencies for 3-Phase, 6-Phase and 12-Phase configuration, respectively.

As visible, thanks to the higher value of the phase inductance, torque ripple for the 12-Phase configuration is low even at low switching frequencies. In fact, in 12-Phase configuration, the value of the phase inductance is quadruple the 3-Phase one. This means that 12-Phase configuration would be highly beneficial, allowing to obtain an acceptable torque ripple even at lower switching frequencies and with no filtering inductors.

The advantage of multiphase configurations is not limited to the higher inductive component. In fact, it is possible to introduce an offset in the

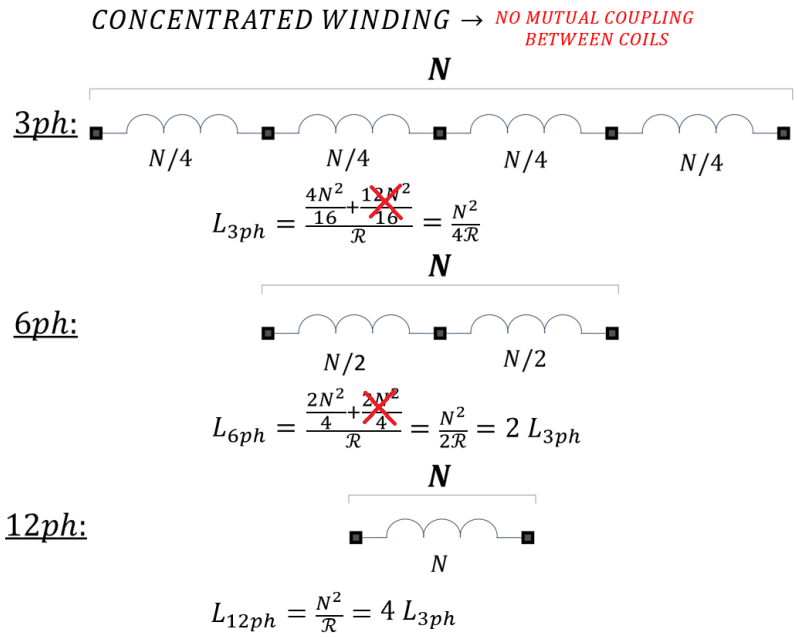

Figure 3.14: Phase inductance computation as a function of the number of conductors per phase for a concentrated winding machine.

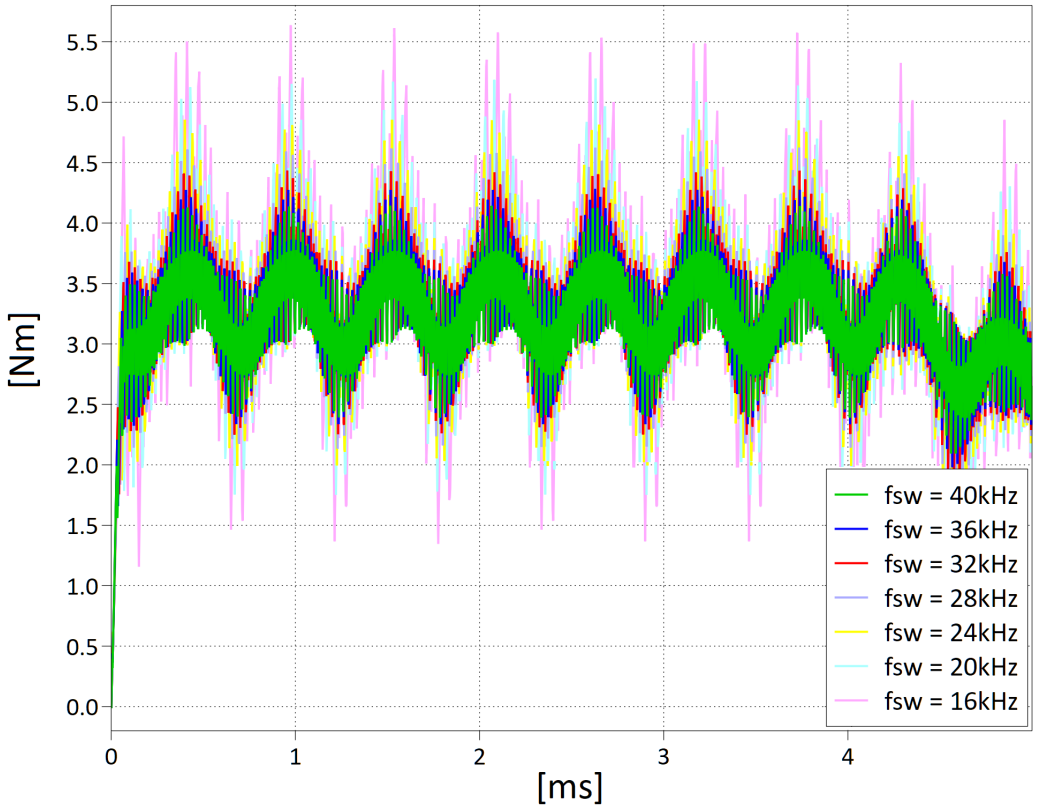

Figure 3.15: Simulated torque and its ripple for different switching frequencies in the 3-Phase configuration.

carriers for PWM modulation of the different three-phase terns that allows a partial compensation of the torque ripple. The introduced offset amounts to 50% for the 6-Phase configuration and to 25% to the 12-Phase configuration between each consecutive three-phase tern.

To enrich the comparison, the overheating of the machine in each configuration should be taken into account too. Multiphase solutions may lead to significant advantages from the thermal point of view, considering the fact that the machine will work in a vacuum chamber.

3.2.3 CSI Motordrive

Nowadays, the world of electrical drives is dominated by the voltage source inverter (VSI). Its high efficiency, simplicity, and widespread availability of

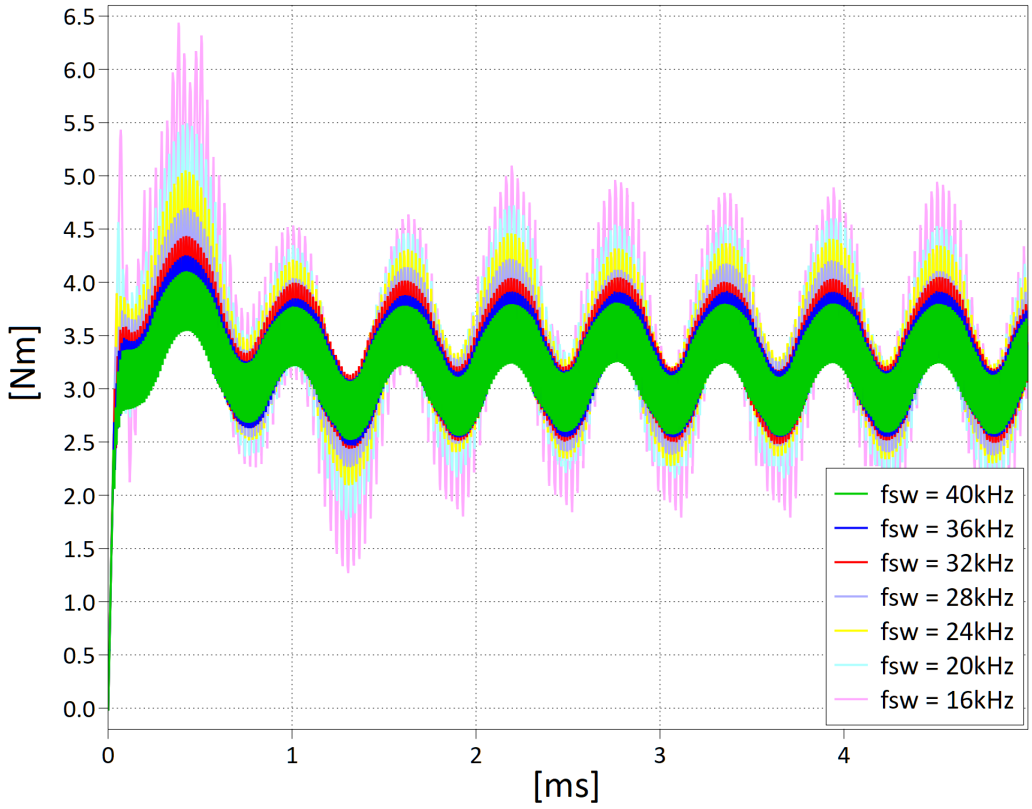

Figure 3.16: Simulated torque and its ripple for different switching frequencies in the 6-Phase configuration.

voltage sources make it the de facto standard solution. Current source inverters (CSI), on the other hand, have never been popular because of their difficult implementation. An additional diode is required in a series to the IGBT, in order to ensure reverse-blocking capability of the IGBT, thus doubling the conduction losses. Moreover, a CSI requires an DC input inductor that may be bulky and heavy due to the limitation of the maximum frequency of the power switches. Eventually, CSI requires a current source and a prestage preserving the continuity of the current on the DC inductor, degrading the overall performance of the system.

Recently, CSI have gained attention, because of new wide bandgap devices, that can solve typical CSI drawbacks. The new switching devices feature: higher switching frequencies; reverse-blocking capability and lower conduction losses. Hence, the dimensions of the input inductor can be re-

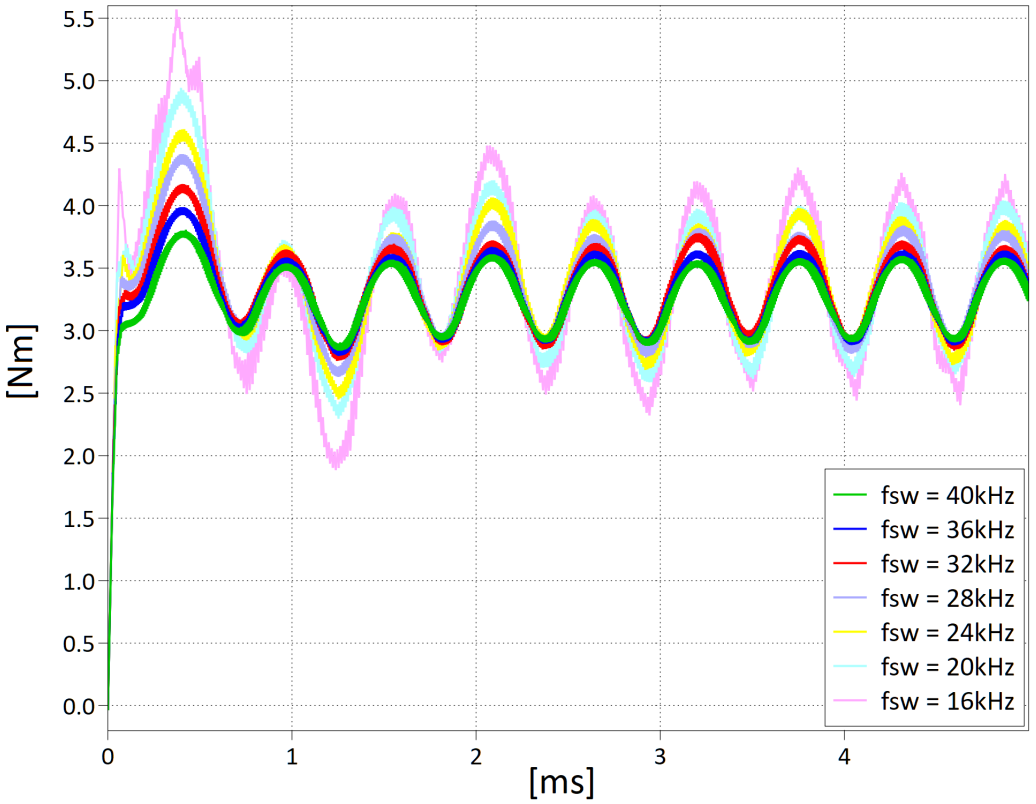

Figure 3.17: Simulated torque and its ripple for different switching frequencies in the 12-Phase configuration.

duced and an additional diode is not required. Specific advantages of CSI make them an attractive solution for some niche applications. CSI directly modulates the current, which means a simpler current control and the DC inductor limits overcurrent in case of phase leg shoot-through [42]. In addition, CSI's low output-voltage total harmonic distortion reduces stress on the insulation systems of both the electric machine and the converter. Due to its inherent voltage boost capability, CSI is ideal for high-speed drives limited by low DC link voltages, delaying the flux weakening operation [43]. At high-speed and higher frequency, the size of the DC inductor can be further decreased. In conclusion, the power density is increased [44] because of the absence of electrolytic capacitors and of the above mentioned features.

On the other hand, the main drawback of a CSI is represented by the higher conduction losses: four devices are always on and a pre-stage is needed.

New topologies have been investigated: an additional leg that conducts during the overlapping periods, reducing the conduction losses [45]. Eventually, it may be possible to avoid the pre-stage in high-speed drives [46].

As exposed in the previous sections, MechSTOR features low values for the phase inductances, hence, has a low filtering capability for the supply current. This means that the quality of supply current waveforms is of the utmost importance to prevent high current ripple.

For a VSI-fed ironless machine, the current and torque ripple can only be reduced with large filtering inductors and high switching frequency. The former increases the size and weight of the power converter; the latter increases switching losses.

This problem can be addressed in a different way by considering a CSI. In fact, with a CSI-fed drive, it is possible to obtain excellent current waveforms, reducing harmonic distortion of the supply current even at lower switching frequency and preventing high torque ripple.

The performance of a CSI drive for MechSTOR were assessed and compared to those of a conventional VSI drive from the standpoint of the phase currents THD and torque ripple. Both drives were modelled and simulated in PLECS in the same conditions, i.e. by keeping the same switching frequency and simulation parameters.

Modeling of VSI-fed and CSI-fed Drives

The complete motordrive, with control system, VSI/CSI and MechSTOR machine, was modelled in PLECS.

For both inverters, SiC MOSFETs s4101 [48] and SiC Schottky diodes s6305 [49] were chosen and a thermal model of these devices was derived from their datasheet. Once the thermal model of the devices is defined, PLECS allows to automatically compute total conduction and switching losses of the inverter. Here, it must be specified that losses on the input filtering capacitor for the VSI and the input filtering inductor for the CSI have not been taken into account.

Simulations were carried out for both converters under the same condi-

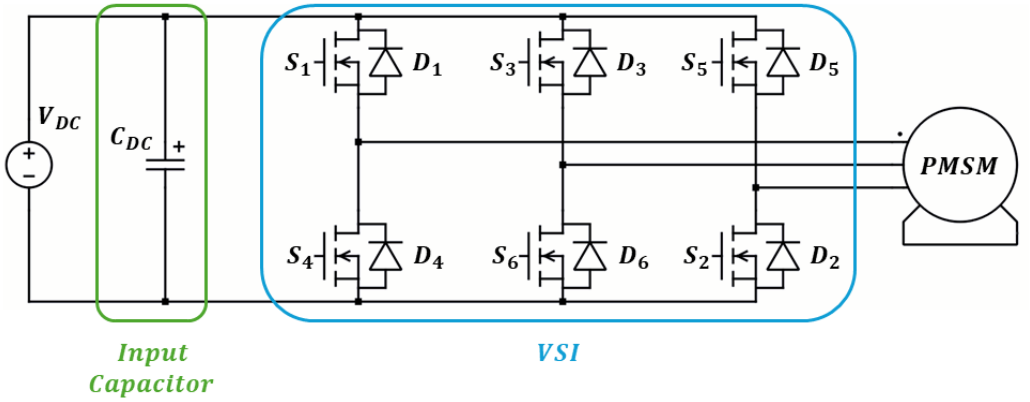

Figure 3.18: VSI architecture [47].

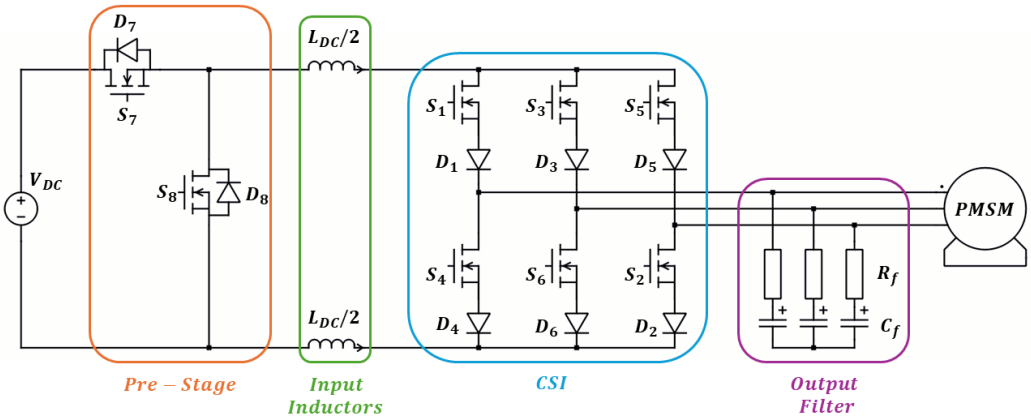

Figure 3.19: CSI architecture [47].

tions, with the parameters listed in Table 3.4 and the performances were estimated in steady state. Simulations were repeated for different values of the switching frequency: 40 kHz, 60 kHz, 80 kHz and 100 kHz. Additional parameters of both inverters are listed in Table 3.5.

For VSI, the traditional architecture with filtering input capacitor was chosen and no output filter was used, as shown in Fig. 3.18. The machine was operated in Maximum Torque Per Ampere (MTPA) mode with $\pi/2$ nominal angle and Space Vector Modulation (SVM).

For CSI, a six switches architecture was chosen, with the pre-stage, the input inductors and the output filtering capacitors, as shown in Fig. 3.19. When the output voltage is smaller than the input voltage, the CSI behaves

as a boost converter, hence, it is not possible to obtain a good control of the input DC current without a pre-stage. A bidirectional PWM boost was chosen as a pre-stage, in order to keep constant the input current source. The CSI was modulated with SVM too. A main difference with VSI happens during the zeo state, when a shoot-through of one leg occurs that creates a re-circulation path for the current because of the presence of the inductor. During this zero state, CSI provides its boost effect on the output voltage. For this reason an overlap between active and zero states is required to prevent an over voltage on the power devices (opposite to the dead-time required for VSI). In addition to that, Field Oriented Control for CSI-fed drives is different from VSI-fed drives, because there are no reference voltages and reference currents are directly modulated from the DC link current.

Results

The phase currents and output torque waveforms for the VSI-fed drive at 40 kHz switching frequency during two electrical periods are shown in Fig. 3.20 and Fig. 3.21, respectively. In this case, a current THD of about 11% and a peak-to-peak torque ripple of about 1.4 Nm were obtained. This level of THD is not acceptable for industrial applications and a significant torque ripple appears because of the low filtering capability of the ironless machine.

Fig. 3.22 and Fig. 3.23 show the same signals obtained with the CSI. The quality of the waveforms is superior with a current THD of about 1.1% and the peak-to-peak torque ripple is reduced at 0.16 Nm with a switching

Table 3.4: Motor Parameters

Parameter	Value
Stator Resistance R_s	1.375 Ω
Stator Inductance L_s	3.9 mH
Poles Number	8
PM Flux Linkage λ_{PM}	0.16 Vs
Rated Torque T	3.67 Nm
Rated Current I_s	1.375 A_{rms}
Poles	8
Reference Speed ω_{ref}	6000 rpm

Table 3.5: Inverters Parameters

VSI

Parameter	Value
Input Capacitor C_{DC}	100 μF

CSI

Parameter	Value
Input Inductor L_{DC}	10 mH
Output Capacitors C_f	5 μF
Output Resistors R_f	10 $m\Omega$

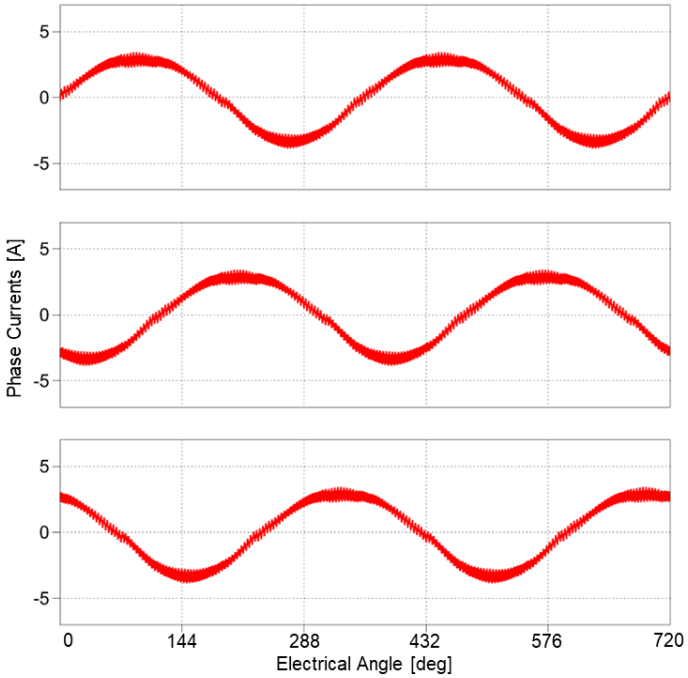

Figure 3.20: Phase currents obtained with VSI-fed drive at $f_{sw} = 40kHz$ [47].

frequency of 40 kHz .

As for the inverter losses, the average value over one switching period and the efficiency in steady-state were computed. Even if CSI has more devices because of the presence of the pre-stage, its losses are slightly lower with a value of about 80 W compared to the 108 W of the VSI at 40 kHz switching frequency. In fact, CSI losses are mainly composed of the pre-stage losses that are about twice the losses of the actual inverter stage (56 W and 25 W,

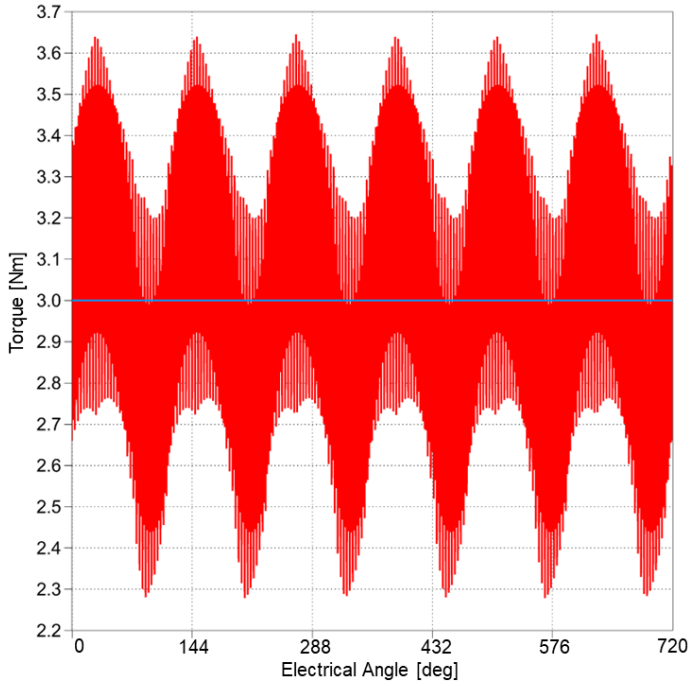

Figure 3.21: Output torque obtained with VSI-fed drive at $f_{sw} = 40kHz$ [47].

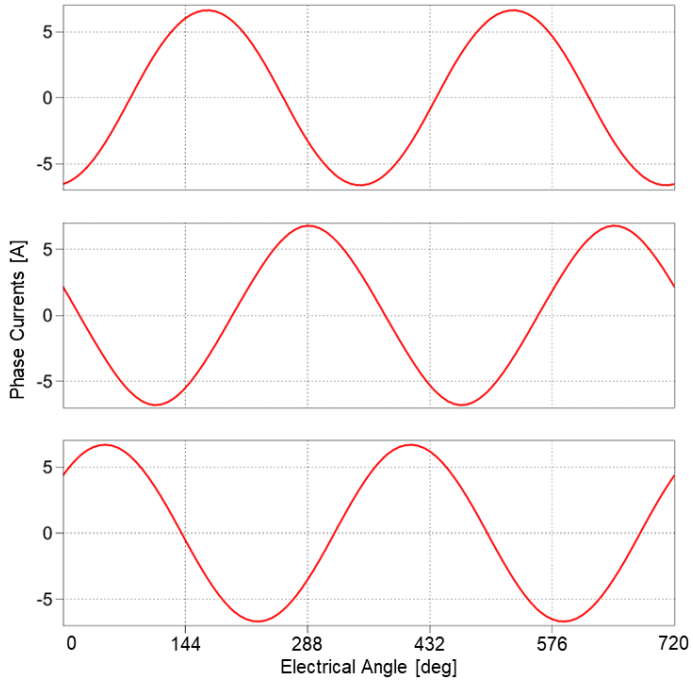

Figure 3.22: Phase currents obtained with CSI-fed drive at $f_{sw} = 40kHz$ [47].

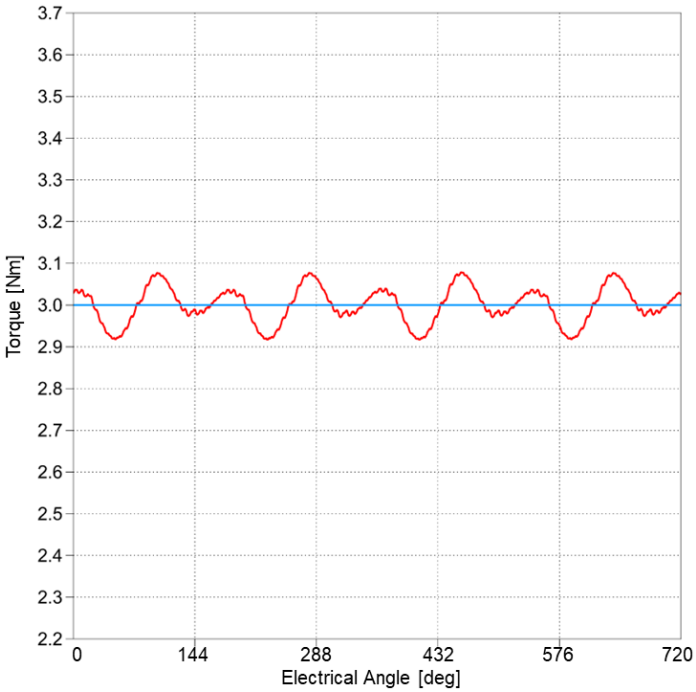

Figure 3.23: Output torque obtained with CSI-fed drive at $f_{sw} = 40kHz$ [47].

respectively).

The estimated values for current THD, percent peak-to-peak torque ripple and inverter efficieny are displayed in Fig. 3.24 and Fig. 3.25 for increasing values of the switching frequency. As visible, CSI's current waveforms and torque ripple are highly superior even at lower frequencies; the efficiency is slightly superior too. Hence, CSI outperforms VSI in this specific application.

Here, the comparison is based on inverter losses only. The performance of CSI-fed drives would be even when we consider motor losses also. In fact, the torque ripple decreases the performance of the machine and hence, its conversion efficiency. In addition to that, losses in the permanent magnets highly depend on the current ripple and a low THD of the current is required to prevent the risk of magnet demagnetization and overheating. These benchmarks are even more important for the FESS applications, where all the losses must be minimized in order to increase the self-discharge duration time. These features will also result in a reduction of vibrations, a feature that is best suited to magnetic bearings that will be used in the final application.

Eventually, in this application it could be possible to remove the pre-stage, the main loss source for the CSI, increasing its performance even more. In fact, the pre-stage is needed only when the back-EMF is lower than the DC bus voltage. In FESS, the electric motor has to work for almost all the time at high speed and the minimum speed value is regulated to avoid energy consuming start-ups. Hence, the pre-stage would be needed only during the initial start-up, and, once high speed is reached, CSI could be directly connected to the DC bus voltage. CSI would operate in boost mode most of the time, allowing a lower DC link voltage source.

In conclusion, CSI proves to be a highly convenient solution for the MechSTOR prototype and FESS application.

In order to enrich this investigation, also motor mechanical losses and electromagnetic losses at different frequencies can be considered for the comparison of both drives.

3.2.4 Vibration Analysis

As exposed in the previous sections, MechSTOR was specifically designed and optimized to minimize electromagnetic losses and increase the self-discharge duration time.

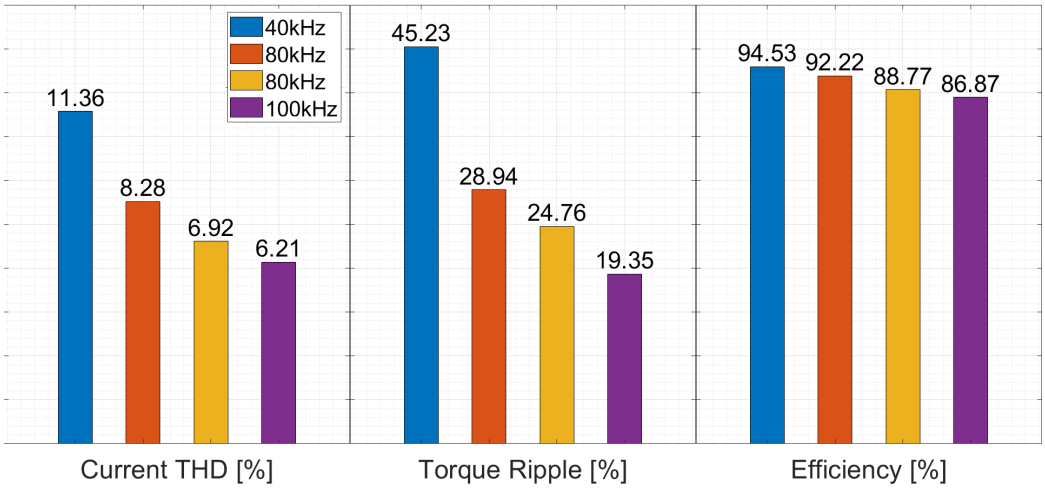

Figure 3.24: Current THD, torque ripple and efficiency obtained for VSI at different switching frequencies [47].

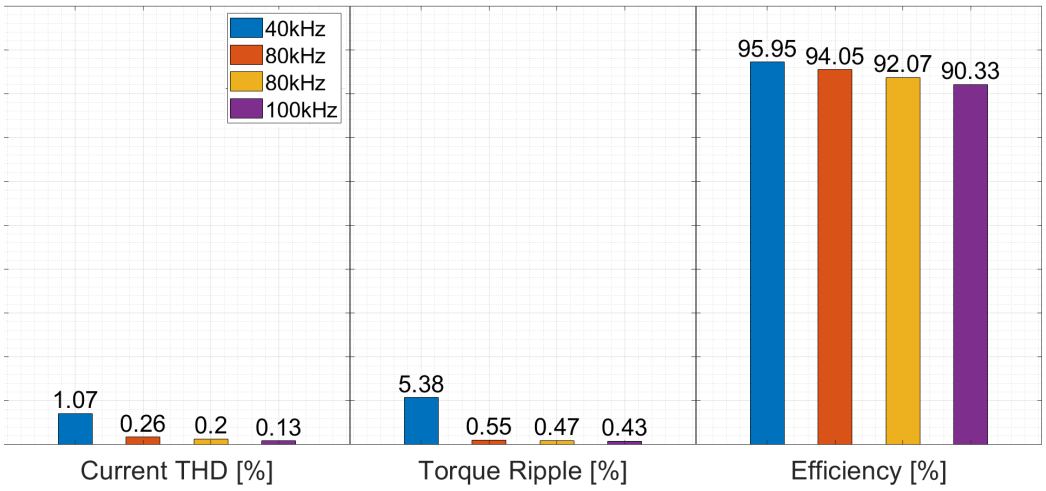

Figure 3.25: Current THD, torque ripple and efficiency obtained for CSI at different switching frequencies [47].

Total FESS losses, however, include not only electromagnetic sources but also mechanical sources. Hence, also the mechanical transmission and structure need an optimal design in order to minimize the overall losses. Part of the mechanical losses can be addressed by some external devices. For example, the solution to ventilation losses has been defined as to seal the entire system in a vacuum container. As for the transmission losses, high performances bearings will be employed. In the current prototype, standard ball bearings were used but magnetic bearings are targeted as a promising solution for future development. This kind of bearings is highly sensitive to radial forces, which in this application are caused mainly by vibrations due to possible imperfections of the system, such as unbalanced rotor and/or the presence of faulty components. Thus, vibration analysis is an essential step needed to make sure that no relevant radial forces will be developed during the normal working condition of the machine. Specifically, the entity of the vibration gets considerably high if the operating frequency of the machine is near the resonant frequency of the system.

Vibration analysis is a fundamental methodological step for the development and optimization of the overall system and it is based on both non-stationary and stationary experiments. Frequency and time-frequency

analyses of radial vibration allow to identify the resonant frequencies of the system that are a key element to steer re-design of mechanical transmission. Fig. 3.26 shows a 3D CAD model of the mechanical housing and transmission for MechSTOR.

Theoretical Basis

The second order differential equation describing the forced response of a simple 1-degree-of-freedom system is the following:

$$m\ddot{x}(t) + c\dot{x}(t) + kx(t) = F(t) \tag{3.11}$$

where m is the mass, c is the damping constant, k is the elastic constant, $F(t)$ is the forcing input.

For the system in exam, i.e. MechSTOR machine, $x(t)$ is the radial vibration signal and, in healthy condition, $F(t)$ can be reasonably modeled as:

$$F(t) = A\Omega^2 \cdot \cos(\Omega t) \tag{3.12}$$

where $\Omega = 2\,\pi\,f_r$, and f_r is the mechanical rotational frequency.

The amplitude of the forcing input is assumed to be proportional to the square of Ω as this is the typical case for not perfectly statically-balanced rotating machinery.

The amplitude X_0 of the system response $x(t)$ at the frequency Ω is [50]:

$$X_0 = \frac{\frac{A}{m}\,(\frac{\Omega}{\omega_n})^2}{\sqrt{(1-\frac{\Omega^2}{\omega_n^2})^2 + (2\,\xi\,\frac{\Omega}{\omega_n})^2}} \tag{3.13}$$

where ω_n and ξ are the natural frequency and damping ratio, respectively:

$$\omega_n = \sqrt{\frac{k}{m}} \tag{3.14}$$

$$\xi = \frac{c}{2\,m\,\omega_n} \tag{3.15}$$

The amplitude of the response will be maximum if the system is excited

at its resonant frequency ω_{peak}:

$$\omega_{peak} = \omega_n \sqrt{1 - 2\xi^2} \tag{3.16}$$

At the resonant frequency, the amplitude of the vibration may be considerably high, hence the exciting frequency must be far from ω_{peak} in order to avoid damage to the system.

The above equations depict an oversimplified model. Actually, real systems have infinite modes of vibration, hence many different natural frequencies. In addition to that, mechanical components as rolling bearings may introduce their characteristic frequencies in the spectrum of the overall system response if certain conditions are met. As for the input excitation, it is more complex than the single-spectral-line force and and a number of harmonics of the fundamental frequency of the input may be non-negligible. For this reason, the system resonant frequencies appearing in proper broad band (at least a few hundreds Hz) should be determined. Once the resonant frequencies are identified, it is possible to assess if the normal working point of the machine is sufficiently distant from these critical frequencies.

A time-frequency analysis of motor signals measured during experimental acquisitions was performed in order to determine the resonant frequencies of the system.

Materials and Methods

In the test bench realized for the experimental acquisitions, MechSTOR is coupled with an electric drive that mimics the flywheel's inertial load, as shown in Fig. 3.27. A triaxial accelerometer is placed on the machine (Fig. 3.28) and coupled to an automated measurement system that samples electrical (line voltages and currents) and mechanical quantities (torque, speed, triaxial accelerometer signals) at $2kHz$.

As the prototype does not include the flywheel, the vibration analysis does not investigate the contribution of friction and ventilation to mechanical losses. However, these are residual with respect to mechanical transmission and bearings, because the final system will be sealed in a vacuum container.

Radial axes signals were acquired both in variable speed conditions and stationary conditions. For the variable speed test, the prototype is operated with a velocity ramp covering the whole range of speed of interest, with discrete steps. The data are processed based on a time-frequency analysis, exploiting the Short Time Fourier Transform. Variable speed test is meant to get a preliminary evaluation of the most critical frequencies in terms of amplitude response of the measured signal, which is an acceleration, $a(t) = \ddot{x}(t)$. Specifically, amplitude peaks in the signal spectrum at low frequencies are the most critical ones because they are linked to higher vibrations. In fact, because of the double integration in the time domain, the amplitude spectrum of the vibration signal $x(t)$ ($|X(j\omega)|$) is obtained by dividing the amplitude spectrum of $a(t)$ ($|A(j\omega)|$) by the square of the frequency:

$$a(t) = \ddot{x}(t) \rightarrow |X(j\omega)| = |A(j\omega)|/\omega^2 \tag{3.17}$$

Once the most critical frequencies and, hence, the corresponding rotational speeds are estimated, the speed range is narrowed around these speeds. In this way, ramp steps are decreased and data are collected with a better velocity resolution, allowing a more accurate detection of the critical speeds.

Finally, stationary tests are performed at the identified critical speeds. These longer acquisitions are meant to confirm the conclusion of the variable speed tests and to estimate with higher accuracy the resonant frequencies of

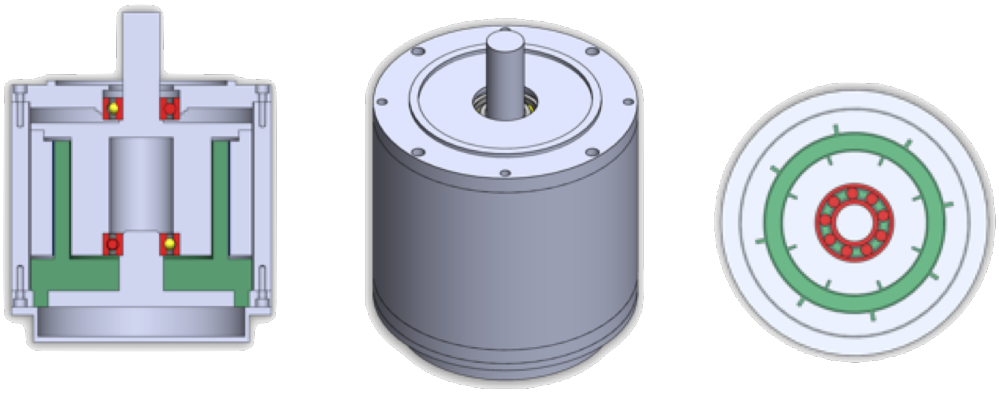

Figure 3.26: 3D model of MechSTOR mechanical housing and transmission [51].

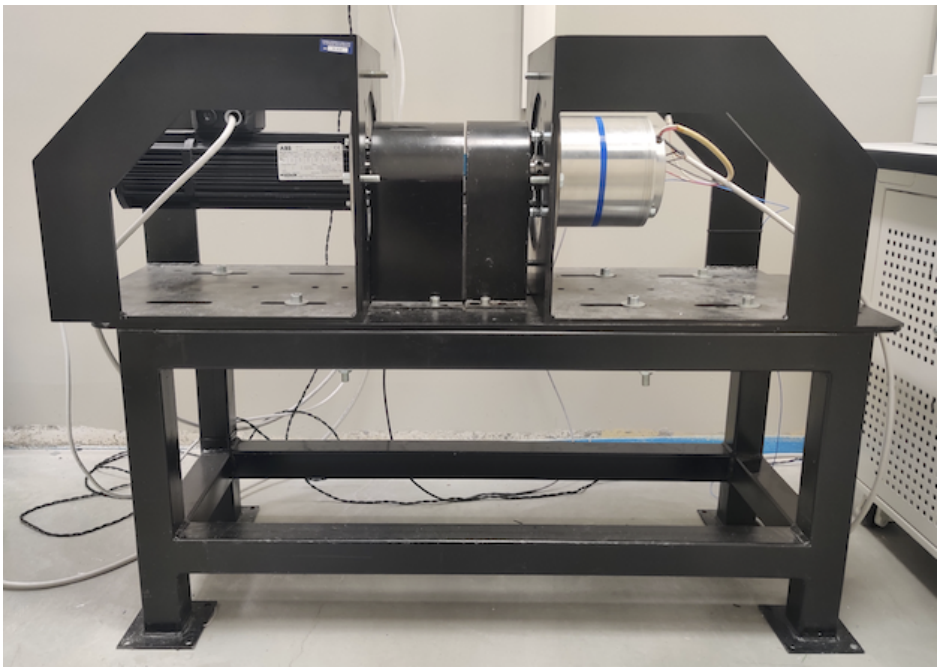

Figure 3.27: Test bench with MechSTOR and load motor [51].

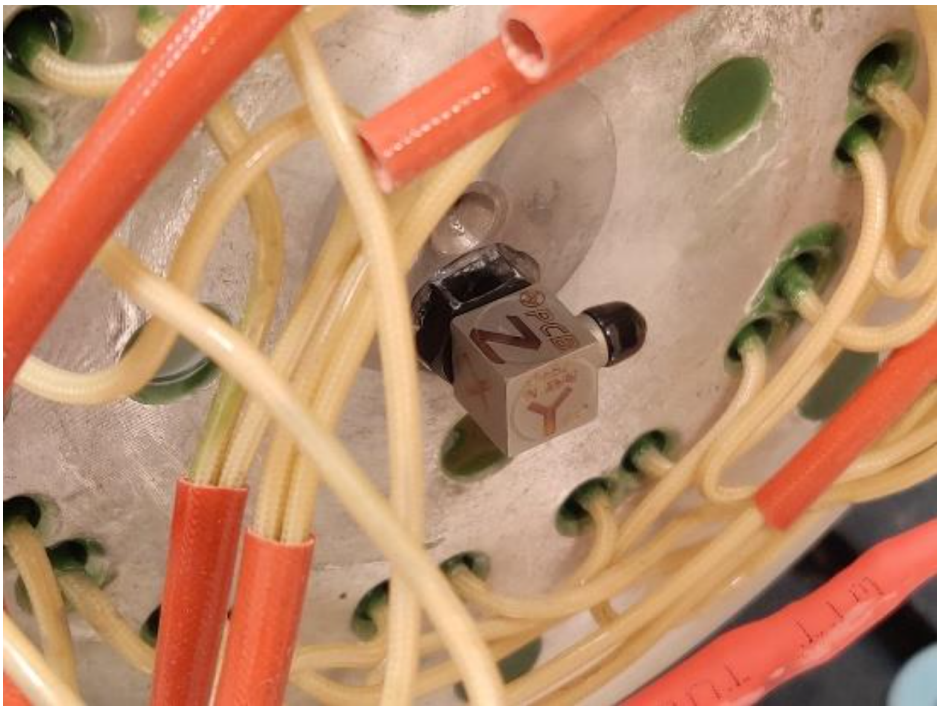

Figure 3.28: Triaxial accelerometer detail [51].

the system.

Results

For variable speed tests, the machine was operated with a speed discrete ramp, ranging from 0 to $1000rpm$, with steps of $50rpm$ lasting $10s$. Fig. 3.29 shows the spectrogram of the radial X-axis signal.

As exposed, the input excitation is composed of multiple harmonics of rotational frequency $k \cdot f_r = k \cdot n_r/60$, where n_r is the shaft speed in rpm. In the spectrogram, amplitude peaks with a diagonal arrangement are visible and they have been highlighted by red lines superimposed to the figure. These amplitude peaks represent the system response to the harmonics of the forcing frequency. In fact, as the rotating speed is almost linearly increasing, the amplitude peaks of the response move towards higher frequencies as the time goes on. Given the great number of harmonics, at each time instant there is at least one of the multiple harmonics that excites one of the resonant frequencies of the system. Therefore, these peak frequencies are highlighted by a sequence of amplitude peaks, resulting in clearly visible horizontal lines.

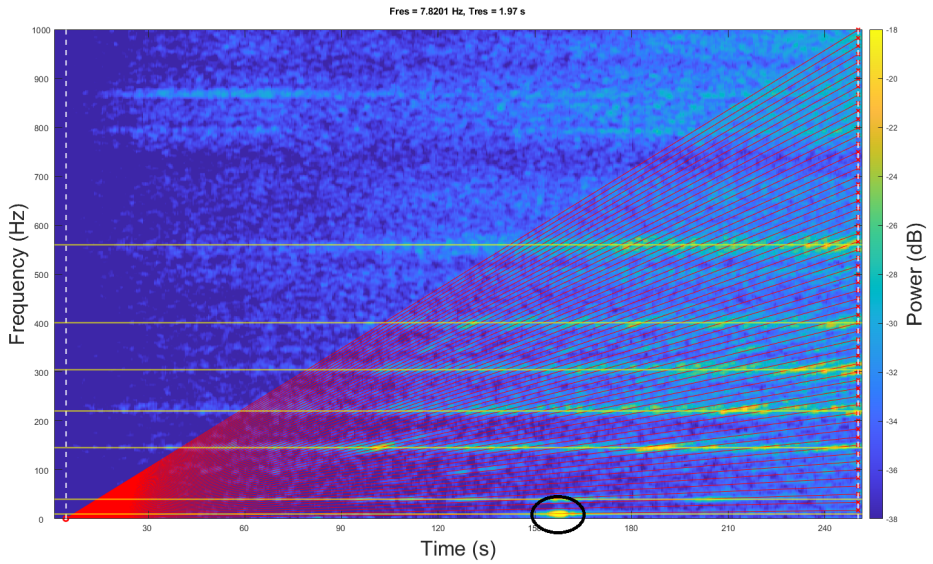

Figure 3.29: Spectrogram of the radial vibration signal during a speed ramp from 0 to 1000 rpm. Multiple harmonics of mechanical rotational frequency (red lines); Resonant frequencies of the system (yellow lines); Critical amplitude peak (black circle) [51].

From this spectrogram it is possible to identify the most critical rotating speeds corresponding to the higher amplitude peaks. Specifically, the most salient amplitude peak is the highlighted one, happening at around $160s$ at low frequencies. As shown, amplitude peaks at low frequencies are linked to higher vibrations. The corresponding rotational speed is about $600rpm$.

A second variable speed test was performed in a narrower range around $600rpm$ with a better speed resolution: discrete speed ramp from 500 to $800rpm$, with steps of $10rpm$ lasting $10s$. Fig. 3.30 shows the spectogram of the radial X-axis signal for this second variable speed test. As for the first test, it is clearly visible the diagonal arrangement for the input frequencies, and the presence of the resonant frequencies (horizontal lines). Thanks to the improved speed resolution, it is possible to better locate the critical point. The highest amplitude response happens at around $100s$ and it corresponds to around $10Hz$ frequency and to $600rpm$ velocity. Therefore, this speed value was selected for the stationary condition test.

For stationary tests, as the speed is constant, the radial accelerometer signal was simply processed with the Power Spectral Density plot, as shown

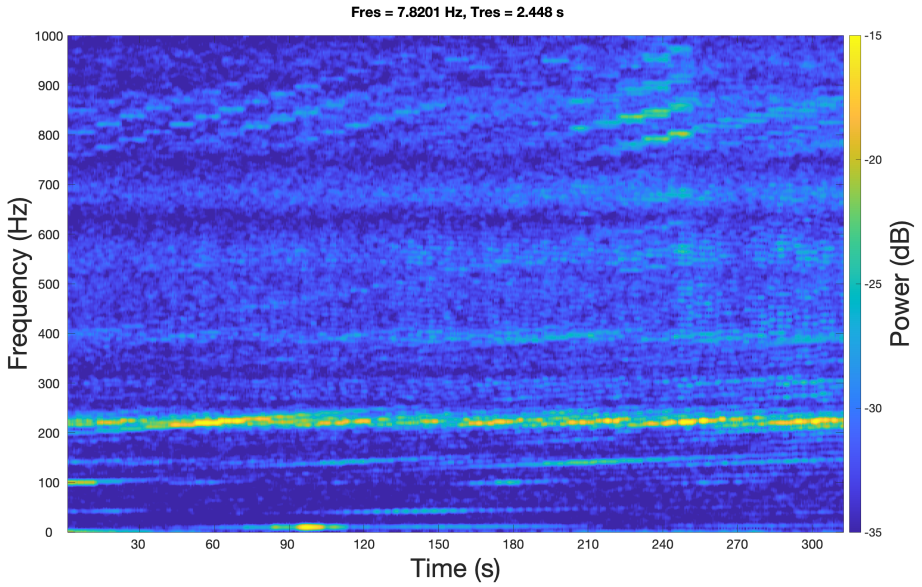

Figure 3.30: Spectrogram of the radial vibration signal during a speed ramp from 500 to 800 rpm [51].

in Fig. 3.31). In the spectrum, it is clearly visible an amplitude peak at around $10Hz$, corresponding to around $600rpm$ velocity. The results are consistent with the variable speed tests and allow to better locate the most critical resonant frequency of the system.

The located resonance frequencies are mostly inherent to the test setup alone. In fact, MechSTOR rotor was balanced before the tests and other sources of unbalance can be excluded. A test run of MechSTOR without braking motor connected showed that, in case of load unbalance or small eccentricity of the rotor, MechSTOR is less prone to radial unbalanced force increasing, thanks to the ironless core [36].

Having located the resonant frequencies of the system, it is possible to make sure that they are sufficiently far from the normal working frequencies of the machine. If this is not the case, then this vibration analysis paves the way for a future modal analysis and an optimal redesign of mechanical transmission and bearings.

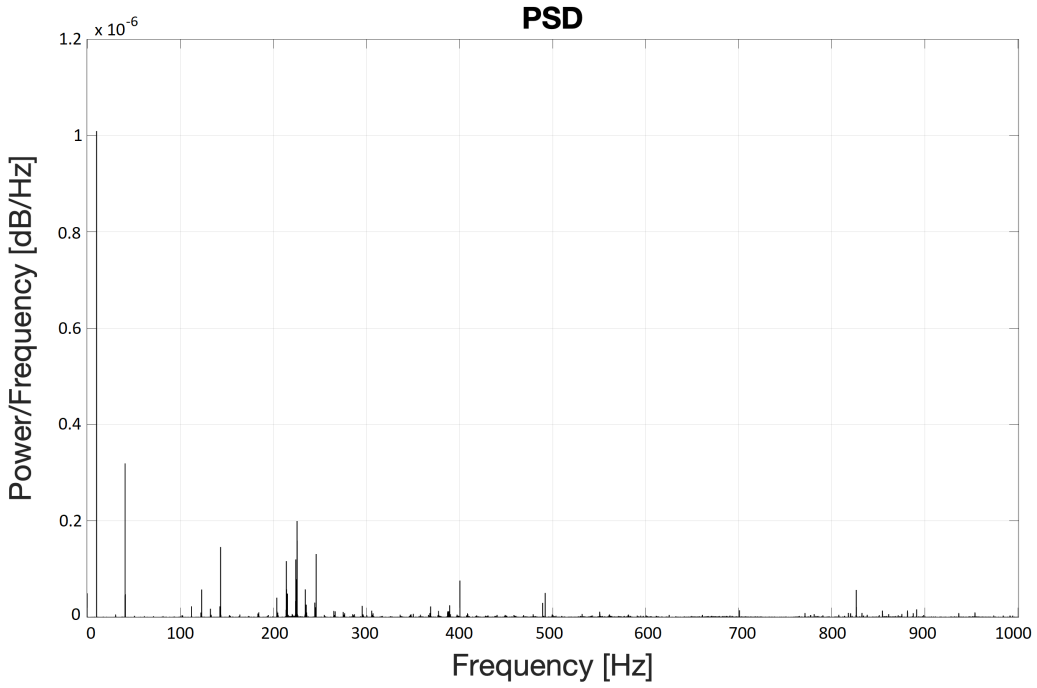

Figure 3.31: Power Spectral Density of the radial accelerometer signal for SC test at 600 rpm [51].

3.3 FESS for Residential Renewables

3.3.1 Standalone and Hybrid Energy Storage Systems

As previously exposed, thanks to their advantages, flywheel energy storage systems could become an interesting alternative to chemical batteries for energy storage at residential level. First of all, FESS feature a high lifetime (about 20 years), high round trip efficiency and lower costs for operation and maintenance which result in a very low effective cost per cycle [52]. Moreover, the impact of FESS is lower than chemical batteries, since they use simpler materials. FESS have a fast time response, and do not show depth of discharge effects; they can provide full power in less than 50-60 ms and change their operation mode (storing v. supplying power) in 10 ms [53]. FESS are competitive for applications that need frequent charge/discharge at a large number of cycles and fast response time, as in a domestic application [54]. As said, they feature, however, a lower self-discharge duration time. In fact, they suffer about 20% of self-discharge per hour [55], [56].

One idea could be to combine FESS and chemical batteries in hybrid systems in order to benefit from the specific advantages of both technologies. In this configuration, FESS serve for peak shaving by absorbing high energy peaks, thanks to their fast response and ruggedness. Then, the energy is transferred to a chemical battery at controlled rate, as batteries have a longer self-discharge duration time. Example applications can be found both in power facilities for frequency regulation purposes [57], [58]; and on smaller scale, for example in micro grids with renewables and EV charge stations [59], [60].

The profitability in terms of energy and cost savings of this hybrid system largely depends on the optimal sizing of the components and on an effective control of the power flow. In fact, the complete system consists in multiple nodes exchanging power bidirectionally.

In the following, two case studies for FESS will be presented. In the first one, a FESS is used as a standalone system for residential renewables energy storage. Specifically, FESS is coupled to a domestic photovoltaic panel as

a replacement for a standard chemical battery, as depicted in Fig. 3.32. In the second one, FESS is included in a hybrid energy storage system (HESS) for a university dorm and library building. A nodes scheme of the complete system considering also the chemical battery is depicted in Fig. 3.33.

In both case studies, performance of the complete system are assessed by means of simulations. A simulation model was developed in Matlab/Simulink environment reproducing the bidirectional power flow between all the nodes of the complete system. Thanks to its structure, it is possible to easily include additional nodes to consider different storing systems and scenarios [62]. The electric machine driving the flywheel is the ironless motor/generator prototype (MechSTOR) [36] whose losses were modeled by 2D Finite Element Analysis (FEA), but any kind of machine can be considered once its loss model is known.

The model is based on an optimal control of the power flow between all the system's nodes and was developed in order to estimate the best match

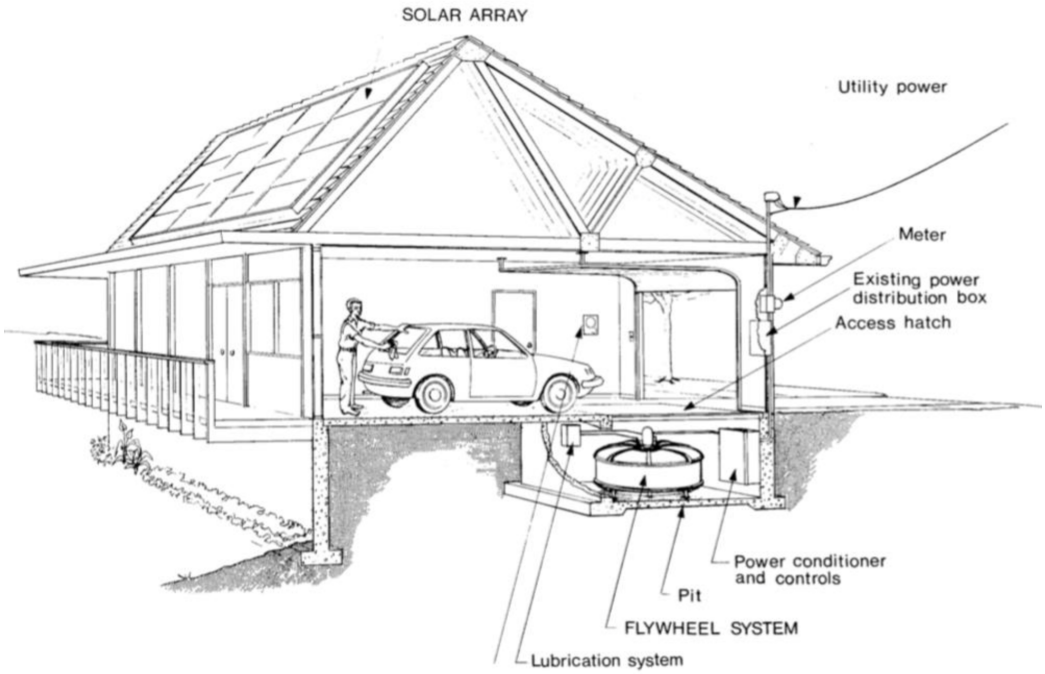

Figure 3.32: Conceptual image of a flywheel energy storage system coupled to a residential PV array [61].

between peak power output of the installed PV array, and the FESS and battery power and energy ratings. It allows to simulate different possible combinations for all the design variables of the system and to select the one best suited to the PV generation and load profiles. Energy savings are estimated for different scenarios and the performance is assessed by means of quantitative indicators.

3.3.2 Modeling of the System

Design Variables of the System

In the model, a few parameters can be tuned to achieve the best energy savings. These parameters are listed in the following:

- Power generation and electric loads:
  - Installed peak PV power (P_{PV}^{pk});

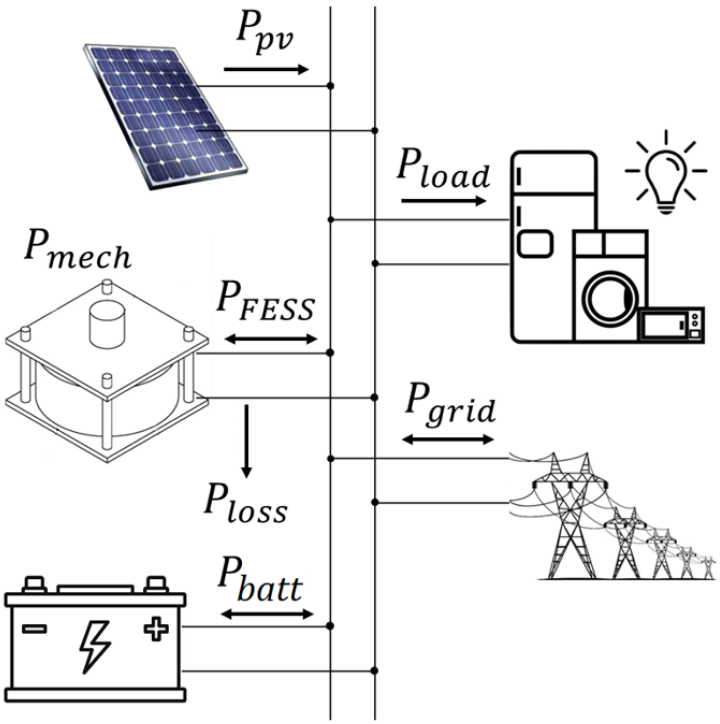

Figure 3.33: Block model of a hybrid system with PV, electric load, FESS and chemical battery.

  - Average annual consumption of the building (E_{load});

- Motor/generator design variables:

  - Type of electric machine;
  - Rated Torque (T_{max});
  - Rated speed (w_{max});

- Flywheel mechanical inertia $J = \pi\rho R^4 H/2$:

  - Radius (R) and height (H) of the flywheel;
  - Density of the flywheel's material (ρ);
  - Number of flywheels (N);

- Chemical battery:

  - Maximum charge/discharge power ($P_{batt,max}$);
  - Battery capacity (C_{batt}).

Modeling of the Flywheel Energy Storage System

The system is represented by a high level model that simulates the FESS with Matlab/Simulink continuous blocks. It is not aimed at modelling in detail the electric and mechanical behaviour of all the components involved in the system (PV array, power converters, electric machine, flywheel, bearings...) Its purpose is to estimate the daily cycles and final energy savings on the basis of the power flow for a given PV array size and a given electric load.

The motor/generator driving the FESS is assumed as an ideal mechanical system, modeled by the following equations:

$$P_{mech} = P_{FESS} - P_{loss} = T\omega, \tag{3.18}$$

$$J\frac{d\omega}{dt} = T, \tag{3.19}$$

where:

- P_{mech}: mechanical power developed by the electric machine;
- P_{FESS}: power flowing to/from the electric machine;
- P_{loss}: power losses of the flywheel and of the electric machine;
- J: moment of inertia of the FESS;
- ω: mechanical speed;
- T: mechanical torque;

Then, the instantaneous speed of the FESS can be computed combining (3.18) and (3.19):

$$\frac{d\omega}{dt} = \frac{P_{mech}}{Jw}. \tag{3.20}$$

Finally, the instantaneous energy stored in the FESS is given by the flywheel' s kinetic energy:

$$E_{FESS} = \frac{1}{2} J\omega^2. \tag{3.21}$$

Power losses are modeled with look-up tables (LUT) based on the instantaneous speed and torque of the machine (Fig. 3.34). Core and PM losses are proportional to machine speed. Hence, the losses computed are stored in a LUT as a function of ω. On the other hand, Joule losses are mainly proportional to the input current, i.e. to the developed torques. Hence, Joule losses are stored in a LUT, as a function T.

The breakpoints and values of the LUTs are computed by a 2D Finite Element Analysis (FEA) of MechSTOR. As previously stated, Joule losses represent the the more relevant loss source for MechSTOR. It should be highlighted that any type of electric machine can be easily included in the model provided that a loss model of the machine is available.

In summary, (3.20) is used to compute ω, then the instantaneous energy stored in the flywheel is estimated.

At start-up a large mechanical torque is required to spin the flywheel. For this reason, a minimum value ω_{min} for the speed was set. Hence, given the

operating speed range from ω_{min} to rated speed ω_{max}, the FESS's capacity can be expressed as:

$$C_{FESS} = E_{FESS,max} - E_{FESS,min} = \frac{1}{2} J(\omega_{max}^2 - \omega_{min}^2). \tag{3.22}$$

Completely discharging the flywheel would be more convenient in terms of energy savings, but this would require designing an electric machine with an high rated torque. Moreover, in order to keep the speed higher than ω_{min}, power must be drawn from the grid during idling time. This is apparently a paradox, but it allows a lower rated torque and, hence, lower electric machine size. Bigger dimensions mean more encumbrance (not suited for domestic applications), more losses (detrimental for the self-discharge time) and higher costs. In fact, the developed torque is given by:

$$T = \frac{\pi}{4} D_s^2 L_{stk} \hat{K}_s \hat{B}_g, \tag{3.23}$$

where:

- D_s: stator diameter;
- L_{stk}: stack length;
- $\hat{K}_s$: electric loading;
- $\hat{B}_g$: magnetic loading.

A higher T can be obtained by increasing L_{stk} and keeping the other parameters constant. For example, assuming to double T by doubling L_{stk} also Joule, PM and core losses will approximately double because the conductor length, PM length and core length will double.

Modeling of the Chemical Battery

For the chemical storage, a commercial home battery from LG Energy Solutions was considered (LG Prime) [63]. The modeling of the battery is simpler than the modeling of the FESS. In fact, the discharge duration time of a chemical battery is quite higher than the one of a FESS. Thus, the discharge

time of the battery was considered negligible for the system dynamics and no loss model was inserted. Only the conversion efficiency η_{batt} was considered in order to take into account the losses involved in the charge/discharge of the battery. Hence, the instantaneous energy stored in the battery can be simply modeled as:

$$E_{batt}(t) = E_{batt}(0) + \int_0^t \eta_{batt} P_{batt}(t)\, dt, \tag{3.24}$$

where:

- $E_{batt}(0)$: energy stored at the start of the simulation (assumed to be 0);
- η_{batt}: conversion efficiency;
- P_{batt}: power flowing to/from the battery.

Power Flow Control Logic

The main core of the model is the logic subsystem controlling the bidirectional power flow between PV, electric load, FESS and the grid where:

- P_{pv}: power output from the PV array;
- P_{load}: power demand by the domestic load (absolute value);

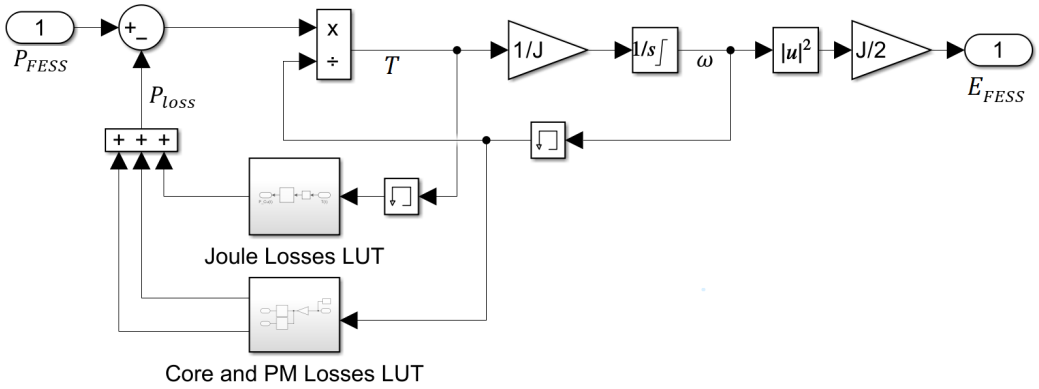

Figure 3.34: FESS block model.

- $P_{net} = P_{pv} - P_{load}$: net available/required power;
- P_{loss}: electric machine's losses (absolute value);
- P_{FESS}: power flowing to/from the flywheel;
- P_{grid}: power flowing to/from the grid;
- P_{batt}: power flowing to/from the chemical battery;
- E_{batt}: energy stored in the battery.

The control system takes into account all the possible four scenarios with their different priorities, as summarized in Table 3.6:

- Surplus in the PV generated power ($P_{net} - P_{loss} > 0$):

(1) MOTOR: If the speed is below the rated value ($\omega < \omega_{max}$), the energy can be stored in the flywheel as kinetic energy and no power is exchanged with the grid ($P_{FESS} = P_{net}$, $P_{batt} = 0$);

(2) HIGH SPEED IDLING: Else ($\omega >= \omega_{max}$) the FESS is only fed to cover the losses and keep it at ω_{max}. The remaining amount of power is fed to the battery. ($P_{FESS} = P_{loss}$, $P_{batt} = P_{net} - P_{loss}$);

- PV power output is not enough to cover domestic load demand ($P_{net} - P_{loss} < 0$):

(3) GENERATOR: If $\omega > \omega_{min}$, the kinetic energy of the flywheel is converted again in electric form and no power is exchanged with the grid ($P_{FESS} = P_{net}$, $P_{batt} = 0$);

(4) LOW SPEED IDLING: Else ($\omega <= \omega_{min}$), the required power is drawn from the grid. The FESS is disconnected from the PV and the load, but fed by the grid to cover losses and keep it at the minimum speed ω_{min} ($P_{FESS} = P_{loss}$, $P_{batt} = P_{net} - P_{loss}$).

In addition to that, there are four more cases nested in the main scenarios when a chemical battery is included:

(2)* If the battery is fully discharged ($E_{batt} = 0$) the required power is drawn from the grid instead;

*(2**)* If the battery is not fully discharged but the power is higher than the maximum discharge power of the battery ($P_{batt} < -P_{batt,max}$), the extra amount is drawn from the grid.

(4)* If the battery is fully charged ($E_{batt} = C_{batt}$) the power is fed to the grid instead;

*(4**)* If the battery is not fully charged but the power is higher than the maximum charge/discharge power of the battery ($P_{batt} > P_{batt,max}$), the extra amount is fed to the grid.

After this control subsystem, an additional block was inserted in order to limit P_{FESS} to the rated values for MechSTOR. If the requested torque is higher than T_{max}, P_{FESS} is decreased and the exceeding amount of is exchanged with the grid. This means that, in case *(1)* less energy is stored in the FESS and, in case *(3)* more energy is drawn from the grid. In both cases, this entails a decrease in the energy savings. One possible solution would be to increase the power ratings of the machine by increasing the rated torque, but in this case the losses would be higher, as explained previously.

In the standalone FESS case study, the power flow control follows the same principle to privilege self-consumption but it is more simple as the chemical battery node is not included.

Quantitative Indicators

In order to evaluate the performance of the system, three quantitative indicators were considered.

The first one is the *efficiency*, defined as the energy saving due to the FESS as a fraction of the energy that would have been drawn from the grid without a FESS:

$$\eta = \frac{\widetilde{E}^{-}_{grid} - E^{-}_{grid}}{\widetilde{E}^{-}_{grid}}. \tag{3.25}$$

Table 3.6: Control Logic of the Bidirectional Power Flow

	$P_{net} - P_{loss} > 0$	$P_{net} - P_{loss} < 0$
$\omega > \omega_{max}$	$P_{FESS} = P_{loss}$, $P_{grid} = P_{net} - P_{loss}$ ***(2)***	
$\omega \in [\omega_{min}, \omega_{max}]$	$P_{FESS} = P_{net}$, $P_{grid} = 0$ ***(1)***	$P_{FESS} = P_{net}$, $P_{grid} = 0$ ***(3)***
$\omega < \omega_{min}$		$P_{FESS} = P_{loss}$, $P_{grid} = P_{net} - P_{loss}$ ***(4)***

In addition to that, the two following indicators, presented in [64], were adopted.

The *self-sufficiency* is defined as the amount of energy required by the load that was *not* drawn from the grid:

$$\xi = \frac{E_{load} - E^{-}_{grid}}{E_{load}}. \tag{3.26}$$

The *self-consumption* is defined as the amount of energy produced by the PV that was *not* fed back to the grid:

$$\gamma = \frac{E_{PV} - E^{+}_{grid}}{E_{PV}}. \tag{3.27}$$

where:

- $\widetilde{E}^{-}_{grid}$: energy drawn from the grid without FESS;
- E^{-}_{grid}: energy drawn from the grid with FESS;
- $\widetilde{E}^{+}_{grid}$: energy fed to the grid without FESS;
- E^{+}_{grid}: energy fed to the grid with FESS;
- E_{load}: energy required by the load;

- E_{PV}: energy produced by the PV array.

These parameters quantify not only the maximization of the self-consumed PV generated energy but also the minimization of the grid fed-in energy. In fact, feeding the self-generated electricity to the grid is less profitable than self-consumption [65].

Electric Load and Generation Profiles in the Standalone FESS

For the standalone FESS case study, two different domestic electric load profiles were considered, based on two datasets available on online repositories.

The first power profile was extracted from 'MICENE' project's data [66] (*Load 1*). This dataset provides an averaged electric load profile of a typical household in Italy, with an average annual consumption of 3633 kWh. This power profile was obtained by averaging many households and has a timespan of a day. Hence, it may not be sufficiently accurate but still valid for a preliminary qualitative analysis.

For this reason, a second electric load profile was extracted from 'UCI Machine Learning Repository' [67] (*Load 2*). This archive contains real measurements of the consumed active power of a house in Sceaux, France, from 2006 and 2010. The average annual consumption is 9415 kWh.

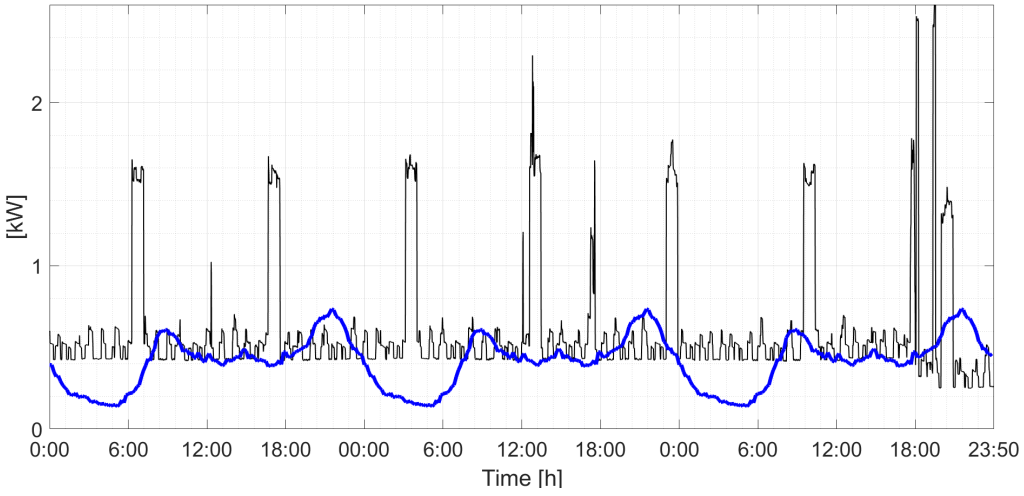

Figure 3.35: Electric load profiles over three days: *Load 1* from MICENE's data (blue) [66] and *Load 2* from UCI's data (black) [67].

Table 3.7: Load Types and PV Array Size

Load Type	Peak PV Power P_{PV}^{pk}	Annual Consumption	House Location	Dataset Source
Load 1	3 kWp	3633 kWh	Cesena, IT	[66]
Load 2	9 kWp	9415 kWh	Sceaux, FR	[67]

Table 3.8: Simulation Parameters

Case	Electric Machine		Flywheel	
I	w_{max}	9000 rpm	R	0.34 m
	w_{min}	25% w_{max}	H	0.15 m
	T_{max}	3 Nm	ρ	7850 kg/m^3
			J	24.7 $kg \cdot m^2$
			C	2.86 kWh
II	-	-	R	0.4 m
	-	-	J	47.35 $kg \cdot m^2$
	-	-	C	5.48 kWh
III	w_{min}	10%	C	3.02 kWh

Fig. 3.35 shows a comparison of the two power profiles for three days. *Load 2* (black) features many peaks and may be more accurate in representing the power flow. *Load 1* (blue) was repeated three times and it is an averaged profile but, being more smooth, is is useful for a qualitative analysis of the daily cycles, as it will be shown in the following sections.

The PV generation profile, on the other hand, was obtained by means of 'PVGIS' tool [68]. By choosing the installed PV peak power and its geographical location it is possible to simulate its power profile over the selected year.

As the two considered electric loads feature different total annual consumption and location, two different PV power profiles were generated to allow comparisons. For the first electric load profile, a 3 kWp PV system located in Cesena, Italy was selected. For the second electric load profile, a 9 kWp PV system located in Sceaux, France was selected.

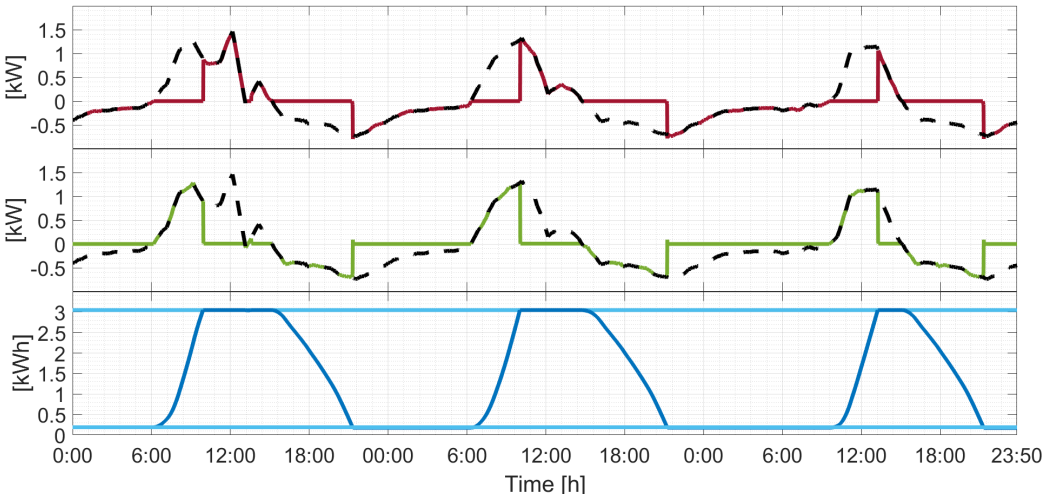

Figure 3.36: P_{net} (black dashed), P_{grid} (red), P_{FESS} (green) and E (blue) during three daily cycles in November [62].

The tool allows to run parametric simulations by changing the values of the design variables and to find the optimal combination once the system specifications are fixed.

At first, an example application was made, considering *Load 1* and a PV system with a peak power of 3 kWp. This simulation was performed to validate the model and to assess the impact of capacity on performance. Different combinations of the parameter's values were considered to increase the capacity of the FESS and the performance of each solution was evaluated.

After this qualitative analysis, another simulation was performed with the more accurate data of *Load 2* in order to obtain realistic results. In this case, a PV system with a peak power of 9 kWp was chosen. Also for this load type, different sizing combinations were considered. The details of each load type are summarized in Table 3.7. Energy savings were estimated on annual simulations in order to take into account seasonal variability.

The qualitative analysis with *Load 1* was performed with the parameters summarized in the first row of Table 3.8 (*Case I*). Fig. 3.36 shows three daily cycles of the power and energy profile during the month of November. The typical operating sequence starts with idling: the energy stored in the FESS is at its minimum value, so the required net power P_{net} and the power

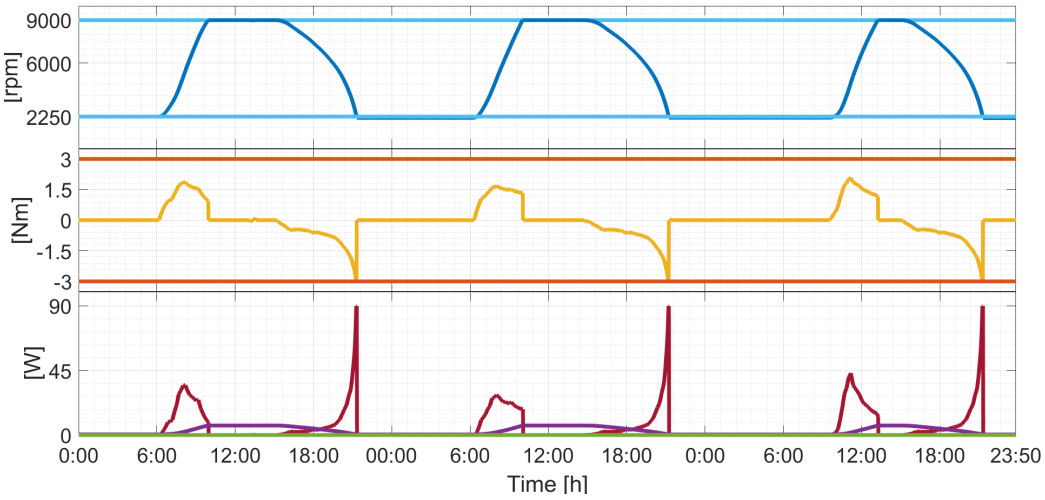

Figure 3.37: Three daily cycles of speed (blue), torque (yellow), Joule losses (red), core losses (green) and PM losses (purple) [62].

to cover the FESS losses are drawn by the grid *(4)*. Then, during daylight, P_{net} becomes positive and the FESS charges *(1)*. When the stored energy reaches E_{max}, idling starts again *(2)*. In the evening, P_{net} becomes negative: now, the FESS is able to cover the power request and discharges until E_{min} *(3)*. Then, the sequence repeats with idling *(4)*.

Fig. 3.37 shows the profiles of FESS speed (blue), torque (yellow) and the three power losses components. With chosen limits for w_{min} (Table 3.8) the torque never exceeds the rated values, hence, the FESS will not require an external start-up but for the initial start-up. As for the power losses, Joule losses (red) are the most relevant component while core losses (green) and PM losses (purple) are negligible. In addition to that, Joule losses are negligible during idling time, when the developed torque is low. Hence, the FESS will be able to keep the stored energy without discharging for longer.

Fig. 3.38 shows the profile of the power drawn from the grid during the same three daily cycles, comparing the case with FESS (blue line) and without FESS (black line). The green areas represent the daily energy savings because in this timespan, the power drawn by the grid with a FESS is lower than the power that would have been drawn without a FESS.

By comparing Fig. 3.37 and Fig. 3.38, it is possible to see that the

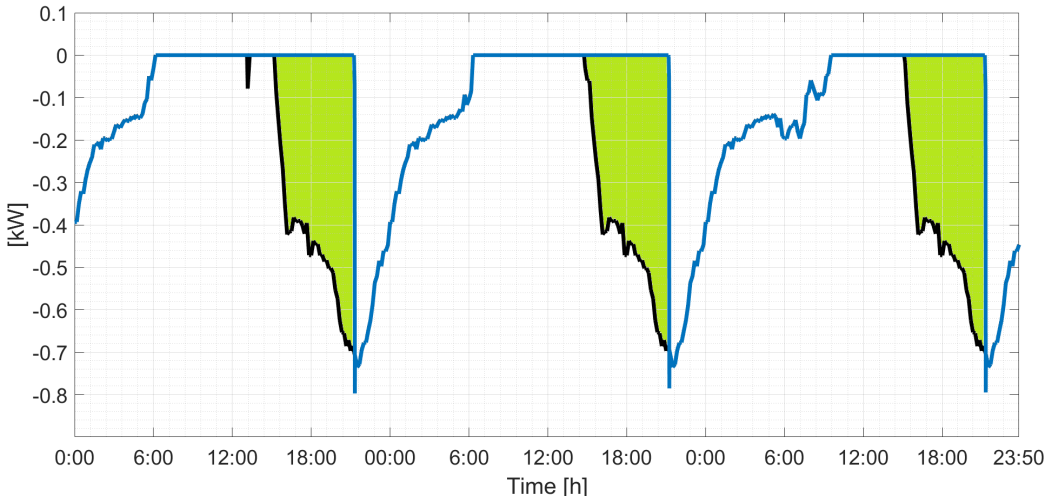

Figure 3.38: Power drawn from the grid without a FESS (black) and with a FESS (blue) and energy savings (green area) during three daily cycles [62].

extension of the green area is limited to the motoring interval *(1)*. If the FESS capacity was higher, the timespan of this discharging interval could be longer and the green area would increase. Hence, a higher capacity can reduce idling time and improve the energy savings. For this reason, two additional combinations of the design variables values were considered to increase FESS capacity . From (3.22), there are two sizing solutions to obtain an higher capacity. The first is to increase the moment of inertia J of the flywheel. Hence, *Case II* was considered by setting $R = 0.4\ m$, with a resulting capacity of 5.48 kWh. The second option is to increase the speed range, either by increasing w_{max} or lowering w_{min}. Hence, for *Case III*, w_{min} was decreased to $10\% \cdot w_{max}$, with a resulting capacity of 2.98 kWh. The three sizing scenarios are summarized in Table 3.8.

Energy exchanges with the grid for each solution were estimated by annual simulations. Fig. 3.39 shows the values of the energy drawn and fed to the grid for each case and compares them to the values obtained without a FESS (red frame). The values of the performance indicators are shown in Fig. 3.40. As visible, a FESS is profitable in terms of energy savings for all the three cases. Considering, for example, *Case II*, a FESS could allow a 69% reduction in the energy purchased by the grid (η), to cover 69% of the load demand

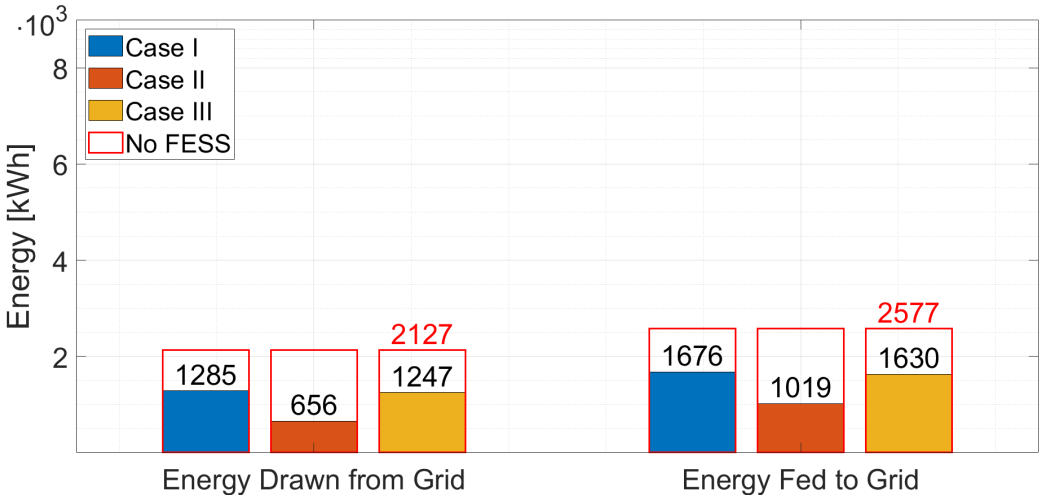

Figure 3.39: Energy exchanged with the grid over one year for *Load 1* for each different sizing: *Case I* (blue), *Case II* (orange), *Case III* (yellow) and case without a FESS (red frame) [62].

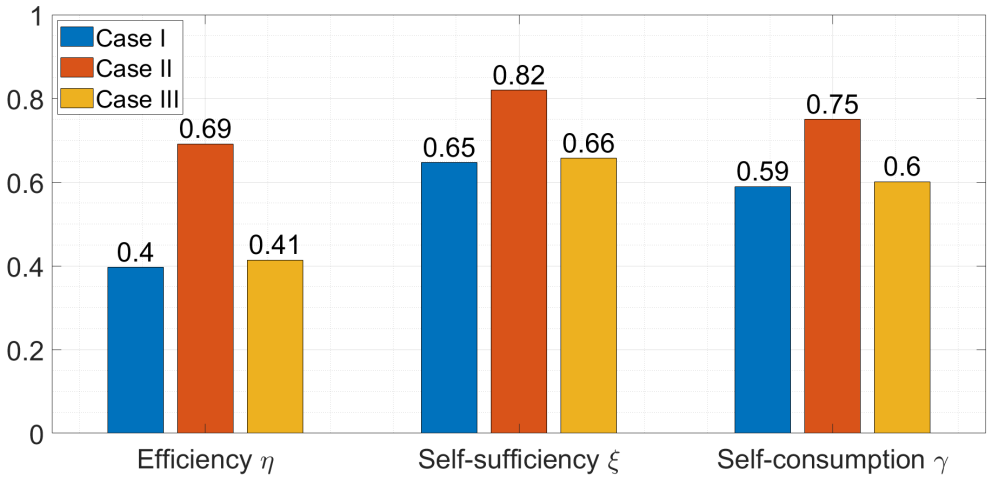

Figure 3.40: Efficiency η, self-sufficiency ξ and self-consumption γ for *Load 1* for each different sizing: *Case I* (blue), *Case II* (orange) and *Case III* [62].

with self-generation (ξ) and to use 75% of PV generated power (γ).

In case of an 'ideal' FESS, the performance indicators would reach the maximum values, i.e. unity. For the self-sufficiency ξ, this would mean that the load demand is completely covered by self-generation, without drawing any power from the grid. For the self-consumption γ, this would mean that all the self-generated energy is consumed by the user, without feeding extra

amounts to the grid (which is less profitable than self-consumption, as previously stated [65]). For these two indicators, high values are more easily achievable. For example, unity could be reached with a FESS with a really high capacity. As for the efficiency η, an unity value would mean that no energy at all is drawn by the grid. A minimum amount of power must be drawn by the grid to cover the power losses of the FESS during idling time. Hence, only a FESS with no losses could achieve an unity value.

Case II performance are the highest because of the higher capacity value obtained by this sizing solution, as expected. On the other hand, *Case III* does not offer significant improvements with respect to *Case I* because, increasing the speed limits has a lower effect on the capacity than increasing J. Still, the performances in each case appear satisfying.

It should be underlined, however, that the *Load 1* is far from the load power profile of a real house. Hence, the following section proposes the same study with a load profile obtained by real measurements in order to provide more realistic estimations.

The same simulations were performed with *Load 2* to obtain more realistic estimations as this dataset includes real measurements of the consumed power from a residential building. Fig. 3.41 shows the values of the energy exchanges with the grid for each case. The total energy consumption of the house and PV peak power are higher than in the previous case (*Load 1*). Hence, to do a comparison between the two load types, the normalized indicators of Fig. 3.42 should be considered. As visible, with a more realistic load type, the values of the performance indicators are lower. Still, the difference between the three sizing solutions show a similar behaviour to *Load 1*. *Case II* gives the best performance in term of energy savings, with a 25% reduction in the energy purchased by the grid (η), a 50% covering of the total load demand with self-generation (ξ) and a 50% use of total PV generated power (γ). As in the previous simulations with *Load 1*, *Case III* does not offer significant improvements with respect to *Case I*.

It should be underlined, however, that the lower values for the performance indicators cannot be attributed exclusively to the fact that, this time, a non-ideal load type was considered. In fact, as seen, the optimal match

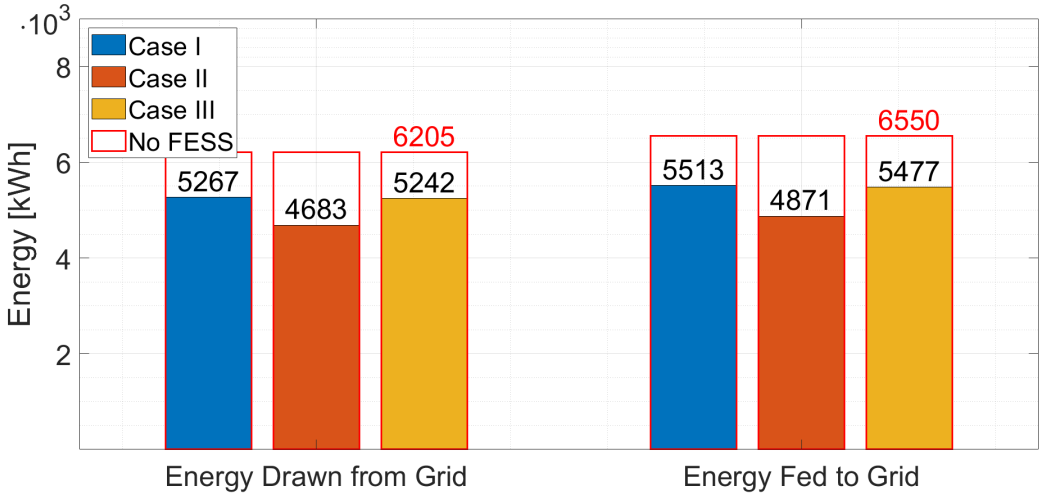

Figure 3.41: Energy exchanged with the grid over one year for *Load 2* for each different sizing: *Case I* (blue), *Case II* (orange), *Case III* (yellow) and case without a FESS (red frame) [62].

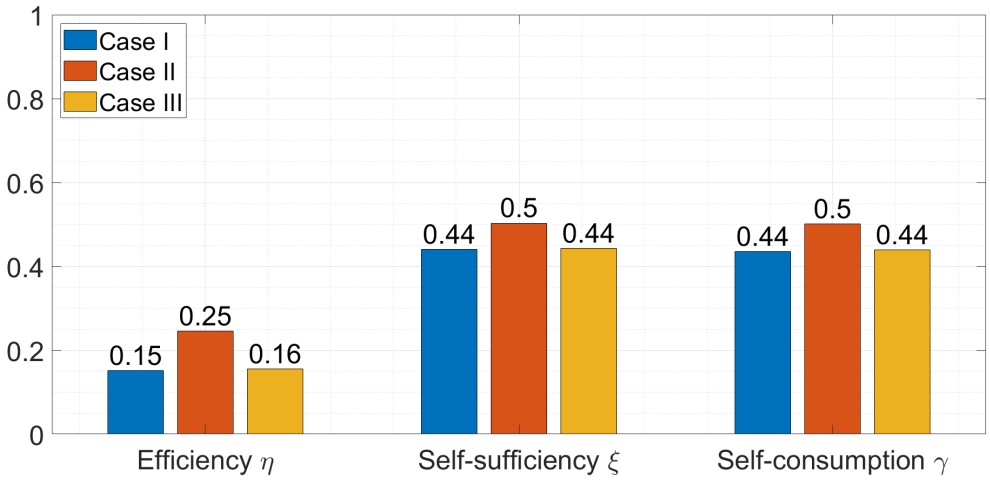

Figure 3.42: Efficiency η, self-sufficiency ξ and self-consumption γ for *Load 2* for each different sizing: *Case I* (blue), *Case II* (orange) and *Case III* [62].

between PV peak power, load request and flywheel capacity is of primary importance for the profitability of the system. As *Load 2* has a significantly higher size than *Load 1*, FESS capacity should be increased even more to improve system performance. In order to achieve that, however, it is necessary to further increase the dimensions of the flywheel. The total volume of the overall machine, however, must not increase too much in order to remain

compliant with the maximum space available for the FESS in the basement and in the vacuum chamber.

Another solution could be to increase the rated speed, but this would require a complete re-design of the electric machine and the bearings. Considering the fact that this is a household application, it is not possible to reach excessive speed because of safety issues. In addition to that, higher speed ratings would entail higher costs and complexity for the electric machine, bearings and mechanical parts.

Thus, in this kind of application, it is mandatory to ascertain as first the values of load request and PV power generation in order to proceed with an ad hoc design of the electric machine.

Electric Load and Generation Profiles in the HESS

The model was applied also for a real case study considering a building of the University of Bologna including a dorm and a library, located in Cesena, Italy (Fig. 3.43).

A bank of 5 FESS with a capacity of about 3 kWh and a battery with a capacity of 16 kWh were chosen, for a gross total of 31 kWh storage capacity and simulation were carried out for different months in order to assess the impact of seasonal variability to the energy savings. The values of these and of the remaining design variables are displayed in Table 3.9.

The electric load profile was obtained by the real consumed active power of the university building. The available data span from June 2022 to October 2023 and are sampled every 15 minutes. The average annual consumption for this building is about 138 MWh.

Similarly for the standalone FESS case study, the PV generation profile was obtained with PVGIS by considering an installed peak power of $30.36kWp$.

The tool allows to select the date and the number of days of the simulation. As could be expected, performance of the system vary with the different seasons of the year. For this reason, at first a qualitative analysis was conducted in order to validate the model and check that the daily cycles

Table 3.9: Parameters for HESS Simulations

FESS		Battery		PV and Load	
Parameter	**Value**	**Parameter**	**Value**	**Parameter**	**Value**
w_{max}	9000 rpm	C_{batt}	16 kWh	P_{PV}^{pk}	30.36 kWp
R	0.34 m	$P_{batt,max}$	7 kW	E_{load}	kWh
w_{min}	25% w_{max}				
H	0.15 m				
T_{max}	3 Nm				
ρ	7850 kg/m^3				
J	24.7 $kg \cdot m^2$				
C	2.86 kWh				
N	5				

Figure 3.43: Picture of the university building roof with the installed PV arrays.

of the exchanged power were correct. Then, energy savings and the values of the performance indicators were computed for a 5 days span (working week) for four different months of the year, in order to take into account seasonal variability.

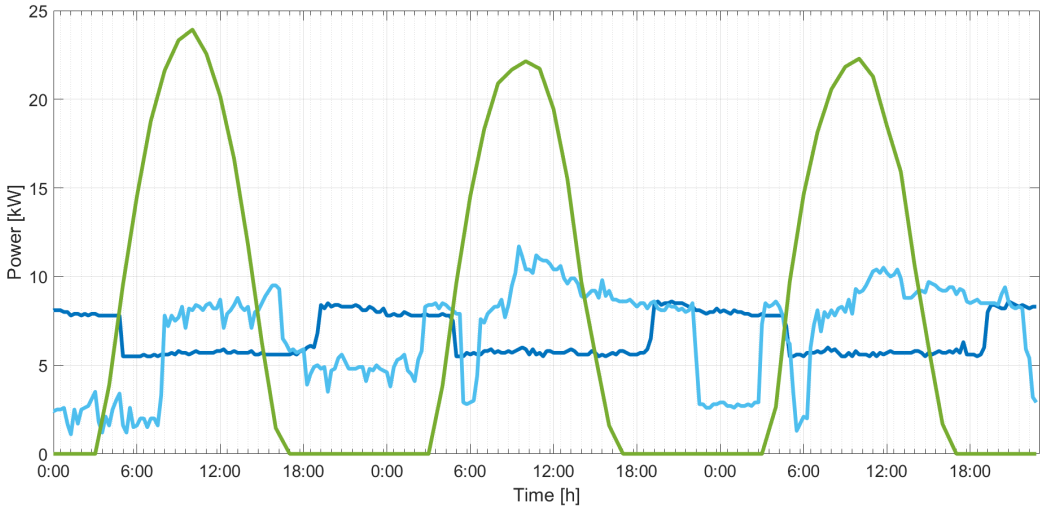

Figure 3.44: Three days of the PV generation profile (green) and load profile (blue for the dorm and light blue for the library) for the month of May.

The qualitative analysis was performed considering two different season of the year: the month of May for spring and the month of July for summer.

Fig. 3.44 shows three days of the PV generation profile (green) and load profile (blue for the dorm and light blue for the library) for the month of May. As visible, spring is a profitable season for PV energy production as the power generation is higher than the load request. In this condition, the use of energy storage could significantly improve energy savings by peak shaving. Fig. 3.45 shows three daily cycles of the simulated power and energy profile with the considered HESS. The operating sequence is similar to the standalone FESS case: it starts with idling *(4)*, then FESS charges during daylight *(1)*. The difference consists in that, When the stored energy reaches E_{max} *(2)*, the power is now fed to the battery until it reaches its mximum capacity; only after that, the remaining power s fed to the grid. Similarly, when in the evening the FESS discharges until E_{min} *(3)*, the required power is taken from the battery until it completely discharges and, after that, power is drawn from the grid. Then, the sequence repeats.

In Fig. 3.46, the profiles of the power drawn from the grid during the three daily cycles in the case with HESS (blue line) and without HESS (black line) are compared. As previosly mentioned, the green areas represent the daily

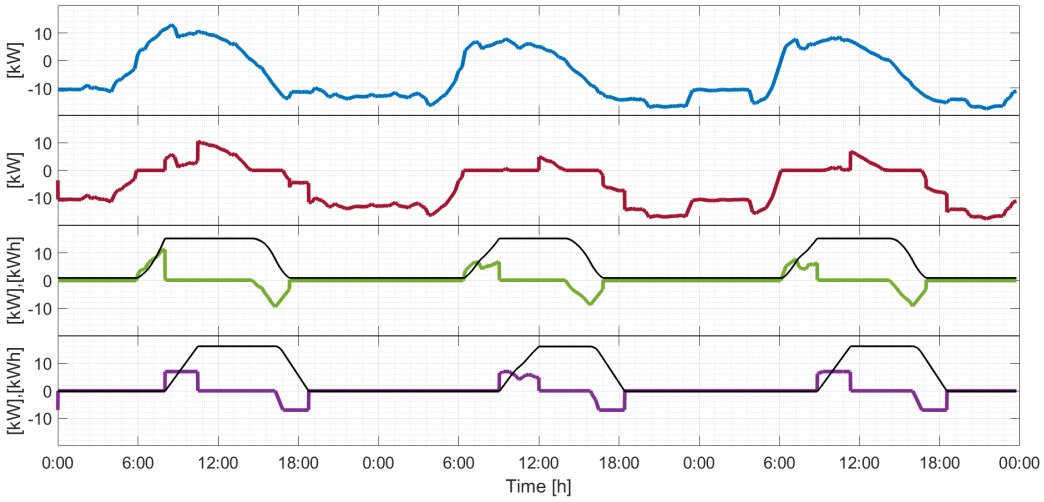

Figure 3.45: P_{net} (blue), P_{grid} (red), P_{FESS} (green) and E_{FESS} (black), P_{batt} (purple) and E_{batt} (black) during three daily cycles in May.

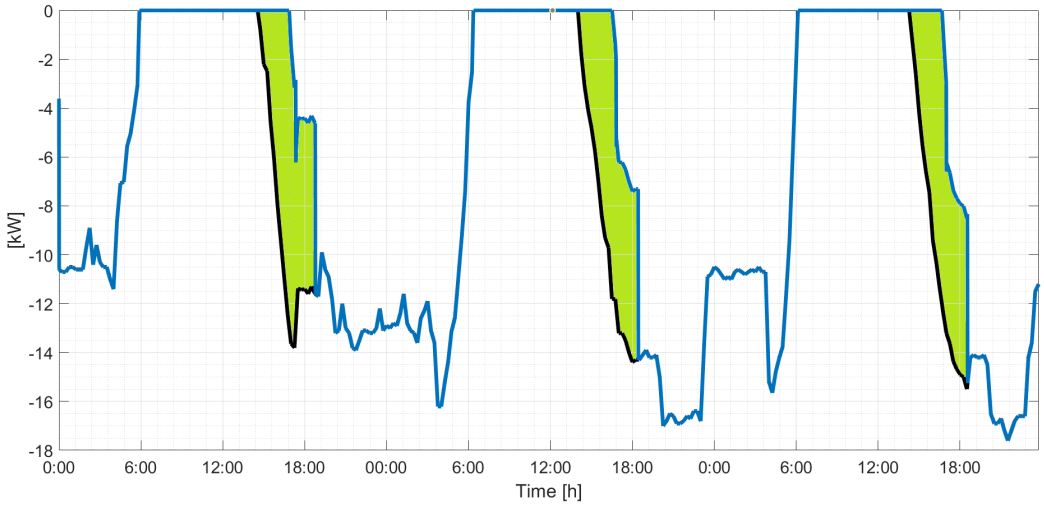

Figure 3.46: Power drawn from the grid without a HESS (black) and with a HESS (blue) and energy savings (green area) during three daily cycles.

energy savings.

As for the standalone FESS case, the extension of the green area is limited to the motoring interval of the FESS *(1)* plus the discharging interval of the battery. Thus, it is possible to increase the energy savings with a higher capacity of the overall HESS. But choosing higher values for the capacity, for example an higher number of flywheels and number of batteries, would be

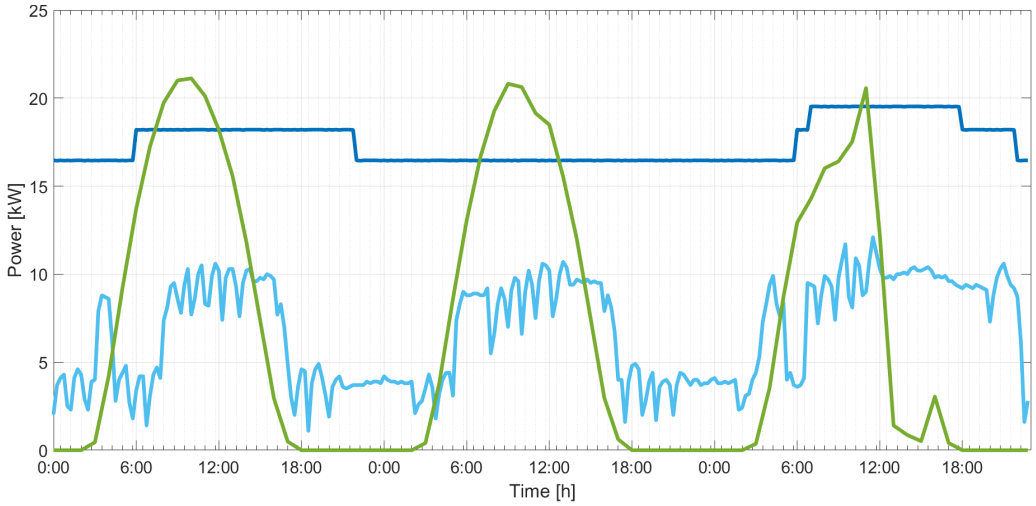

Figure 3.47: Three days of the PV generation profile (green) and load profile (blue for the dorm and light blue for the library) for the month of July.

more expensive and this choice would not be convenient for certain periods of the year. In fact, the system would be oversized for seasons in which the PV generation is low and the additional costs would not be payed back. For example, Fig. 3.47 shows three days of the PV generation profile and load profile for the month of July. As visible, in this case the HESS would never be in operation as load demand is way higher than PV generation and P_{net} is always negative.

The quantitative performance analysis was conducted only for the months of March, April, May and June. In fact, for the remaining months, the PV generation was not enough to cover load demand, hence, an energy storage system was not worth considering. For each of these months, a simulation time of 5 days (working week) was considered and energy exchanges with the grid were estimated. Fig. 3.48 shows the values of the energy drawn and fed to the grid for each month and compares them to the values obtained without a HESS (red frame). The values of the resulting performance indicators are shown in Fig. 3.49. As visible, for these months of the year, a HESS appears profitable in terms of energy savings. Considering, for example, the month of April, a FESS could allow a 26% reduction in the energy purchased by the grid (η), to cover 57% of the load demand with self-generation (ξ) and

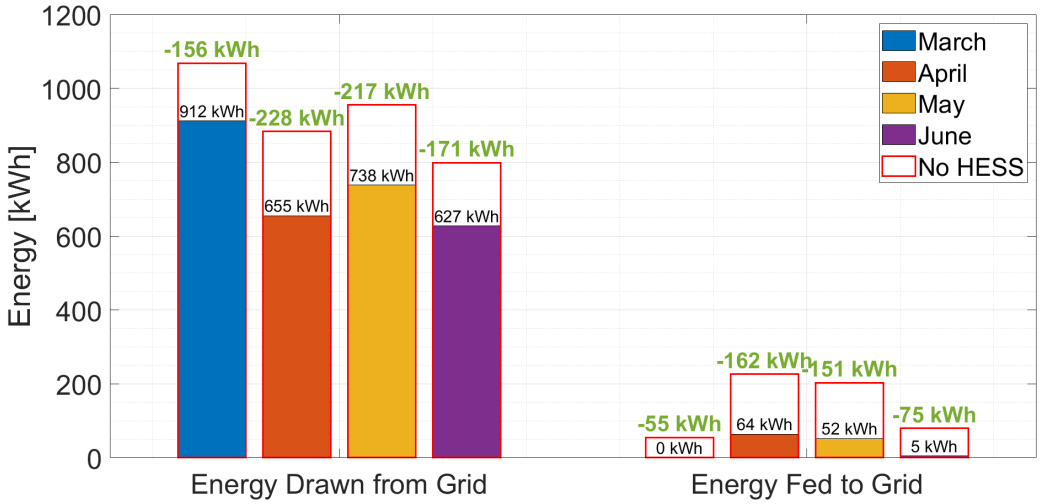

Figure 3.48: Energy exchanged with the grid during five days for different months: March (blue), April (orange), May (yellow) and June (purple) and the case without a HESS (red frame).

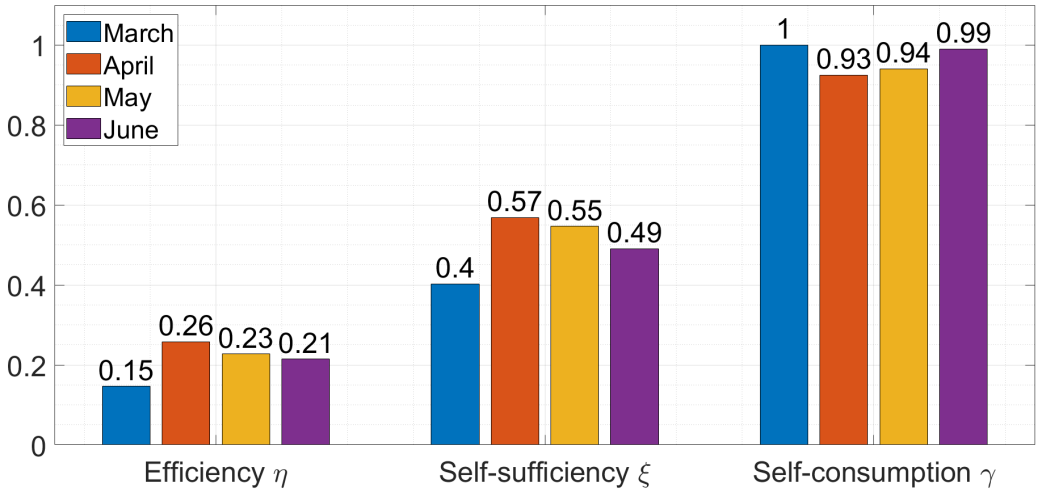

Figure 3.49: Efficiency η, self-sufficiency ξ and self-consumption γ for *Load 1* for different months: March (blue), April (orange), May (yellow) and June (purple).

to use 93% of PV generated power (γ).

As a conclusion, for the months of March, April, May and June, the HESS allows satisfying energy savings but for the other months, the PV generation is not enough to cover load demand, hence, an energy storage system is not worth considering. As a conclusion, for the months of March, April, May and June, the HESS allows satisfying energy savings but for the other months,

the PV generation is not enough to cover load demand, hence, an energy storage system is not worth considering.

Hence, for the considered load and generation profile, an energy storage system appears profitable only during certain periods of the year. The HESS should be shut down during low generation months or the installed PV peak power should be increased, provided that enough space is available.

This case study is an example application of the tool. Other possible combination of parameters, load and generation profiles and locations of the building could be easily investigated as a future development. For example, the performance of a FESS shared between different households in a Renewable Energy Community scenario could be evaluated.

Chapter 4

Case Study: Innovative Power Conversion for Wind Energy

4.1 Electric Drives for Wind Turbines

4.1.1 Onshore and Offshore Wind Farms

As shown in Chapter 1, electricity from wind generation will have a central role in the path towards the zero emissions energy system of the future. By 2050, wind farms global installed capacity (onshore and offshore) is projected to grow from the current 900 GW up to more than 10 000 GW, reaching almost one-third of the total installed capacity from renewable sources [71]. Historical evolution of wind capacity is compared to the total amount required from NZE scenario by 2030 in Fig. 4.1.

Offshore wind, especially, is recognized as one of the leading technologies to meet global climate targets within the next three decades. Its attractiveness stems from the large availability of offshore locations, its high energy output per square meter, and the possibility to build it quickly at gigawatt-scale. Offshore wind is a rapidly maturing technology and has developed significantly in the past decade: during the period from 2010 to 2022, to-

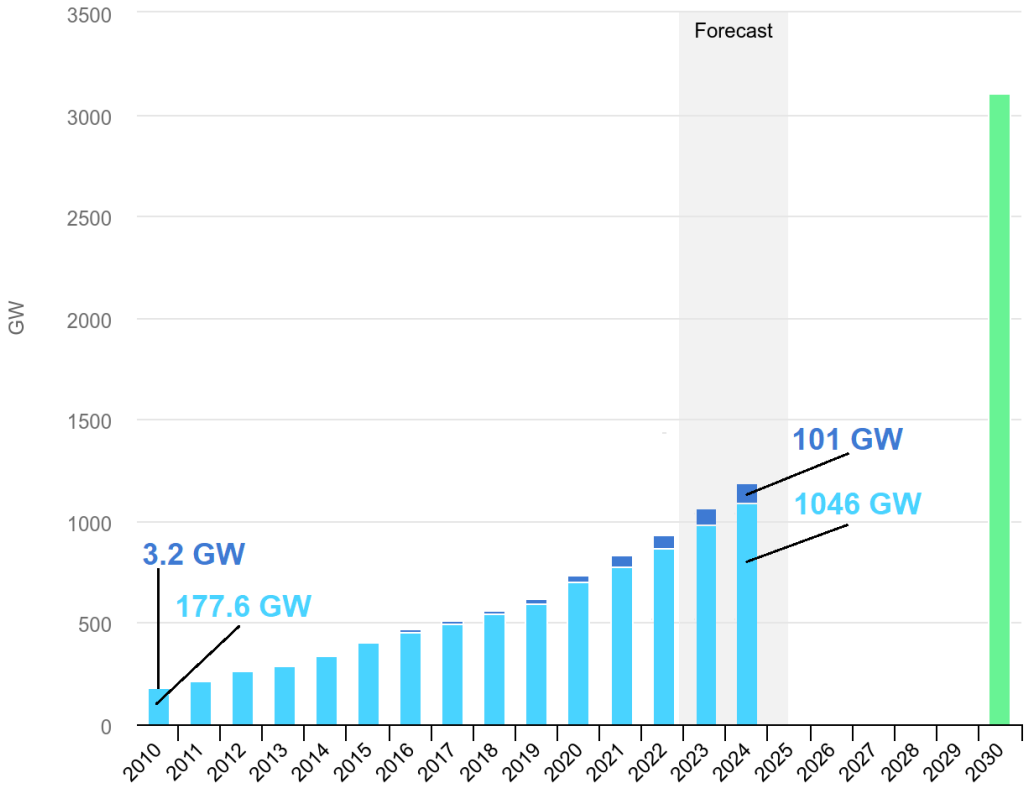

Figure 4.1: Historical and projected wind power capacity and required one for the Net Zero Scenario, 2015-2030 (adapted from [69]).

tal offshore wind installed capacity experienced a twenty-fold increase [72]. The annual offshore wind capacity additions by country from 2015 to 2022 are depicted in Fig. 4.2. North Sea countries (Belgium, Denmark, Germany and the United Kingdom) are pioneers: Denmark deployed the first operational offshore wind farm in 1991 with a capacity of 5 megawatts (MW) [73]. However, deployment is moving beyond the front runners and is broadening to China, Japan, North America and the Republic of Korea [74]. In fact, offshore solutions broaden opportunities for those countries with not enough available space for onshore wind but with consistent seabed drops. Offshore wind represents a cost-effective option to provide electricity to densely populated coastal areas. The push to move offshore wind project sites farther from shore and in deeper waters is motivated by the tremendous increase in their energy potential thanks to the higher and more consistent wind resources.

The growing interest in this technology and its varied geographical distribution amongst countries is reflected by the steady increase in international standards and technical committees in wind technology. Notwithstanding this, today, the offshore wind market remains smaller than the onshore one because of some challenges such as its integration into the energy system via new interconnections, the need for larger turbines and more robust foundations, the demand for critical materials and recycling and other logistical challenges. To exploit its full potential, policy support is needed for RD&D investments, improvements in technology and decrease costs through economies of scale.

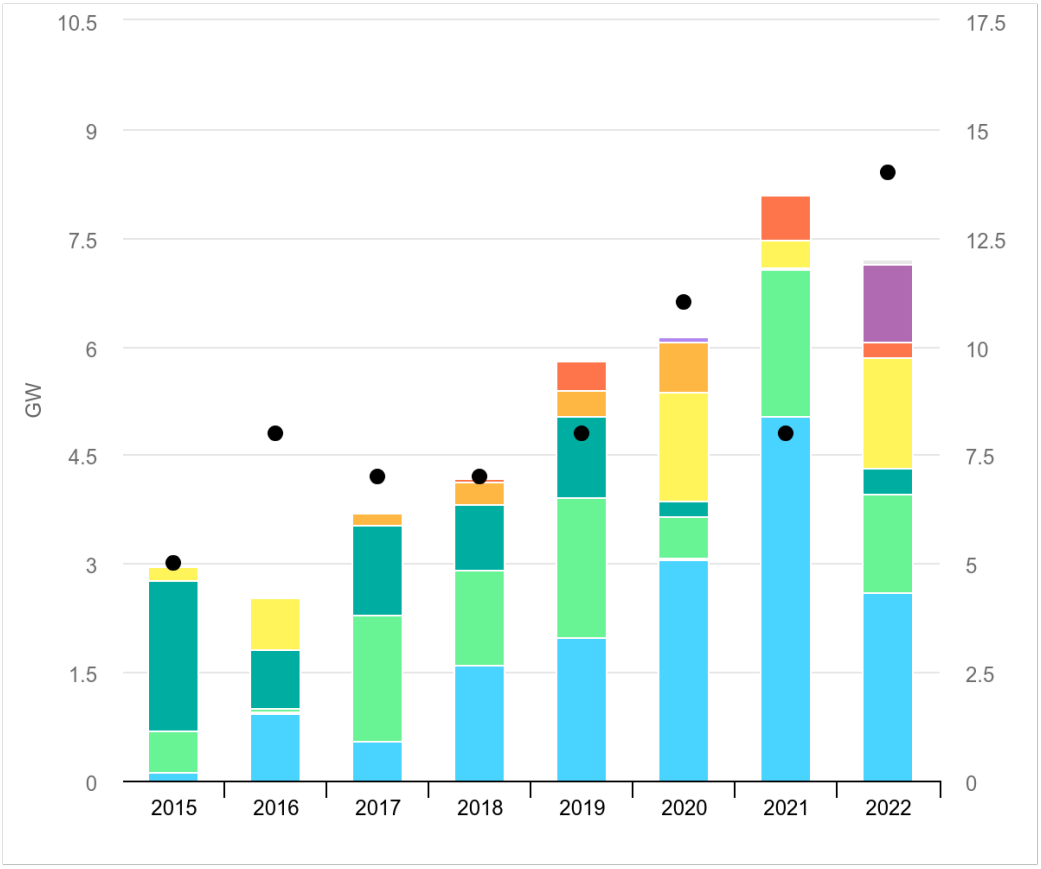

Figure 4.2: Annual offshore wind capacity additions by country/region, 2015-2022 [70].

4.1.2 Innovations and Trends in Wind Energy

In order to make the most of the offshore infrastructure, in recent years research explored some combinations of wind farms with other clean energy technologies. The first one is represented by hybrid systems where offshore wind is clustered with other renewable sources such as solar photovoltaics or ocean energy, such as wave and tidal energy. Even if both offshore solar and wave energy are at a much earlier development stage than offshore wind [71], testing station are currently being installed. In fact, hybrid system would maximise on-site power production and the efficiency of the plant. Flexibility can be enhanced, for example, with wind power providing the consistent base load, while solar and wave contributing during peak demand periods. Moreover, solar panels and wind turbines can share network infrastructure and grid connections and PV generated energy can be used on site for turbine operation. In addition to that, combination of wind farms and clean hydrogen production units is also being explored. In this way, it is possible to make use of the surplus energy during periods of overproduction to produce green hydrogen, an essential instrument for the decarbonization of some hard-to-abate end-use applications. In recent years, installations have grown significantly driven by innovation in electrolysers for clean hydrogen production, the supportive environment of national hydrogen strategies developed by over 30 countries [75] and the economic attractiveness of producing hydrogen offshore [76]. Finally, innovations are arising in the foundation technology of the turbines also. Fixed-bottom turbines are the dominant configuration in the offshore wind sector, but floating offshore wind is gaining traction among the offshore wind industry [77]. In this configuration, wind turbines are installed on floating sub-structures designed to counteract thrust, inertial forces and pitch motions. The turbines themselves are the same as those used for fixed-bottom configurations but this installation gives access to plentiful wind resources at greater water depths. In addition to that, it is possible to select high wind speed sites with greater flexibility, helping to minimize any social and environmental impact.

4.1.3 Wind Power Conversion Systems

Wind turbine systems are composed by the following main elements: a turbine rotor, a gearbox, a generator, a power electronic converter and a transformer for grid connection, as illustrated in Fig. 4.3. The power from the wind is captured by the turbine blades in the form of low-speed, high-torque mechanical power and is adapted to the high-speed, low-torque required by the generator through a gearbox. In case of a multi-pole generator, the gearbox may not be required. The generator converts mechanical power into electrical power which is fed to the grid through power electronic converters, a transformer with circuit breakers and electricity meters, in order to meet the requirements of grid connections.

Maximum Power Point Tracking

The early electric drives for wind turbines were based on squirrel-cage induction generators (SCIGs), operated at constant speed and directly connected to the grid. Nowadays, systems have developed toward a variable-speed approach. In fact, turbine speed control allows to achieve higher efficiency and becomes more and more important as the power level of the turbines increases. In addition to that, power limitation during higher wind speeds is of the utmost importance and this can be achieved both mechanically (stall control, active stall, or pitch control) and electronically (by a proper control of the generator and power converter). The rise in efficiency allowed by variable-speed operation comes from the fact that, to achieve maximum power conversion, there is an optimal rotor speed that depends on the wind

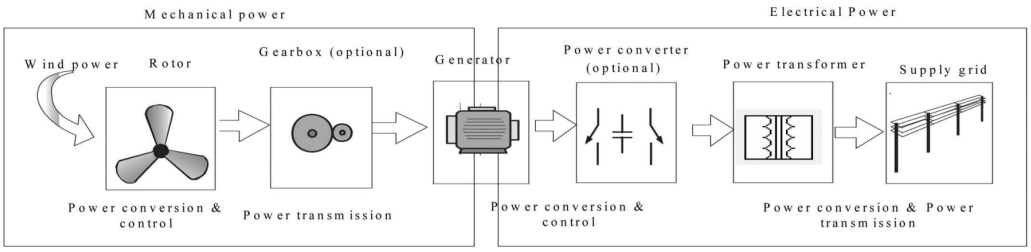

Figure 4.3: Main components of a wind turbine system [78].

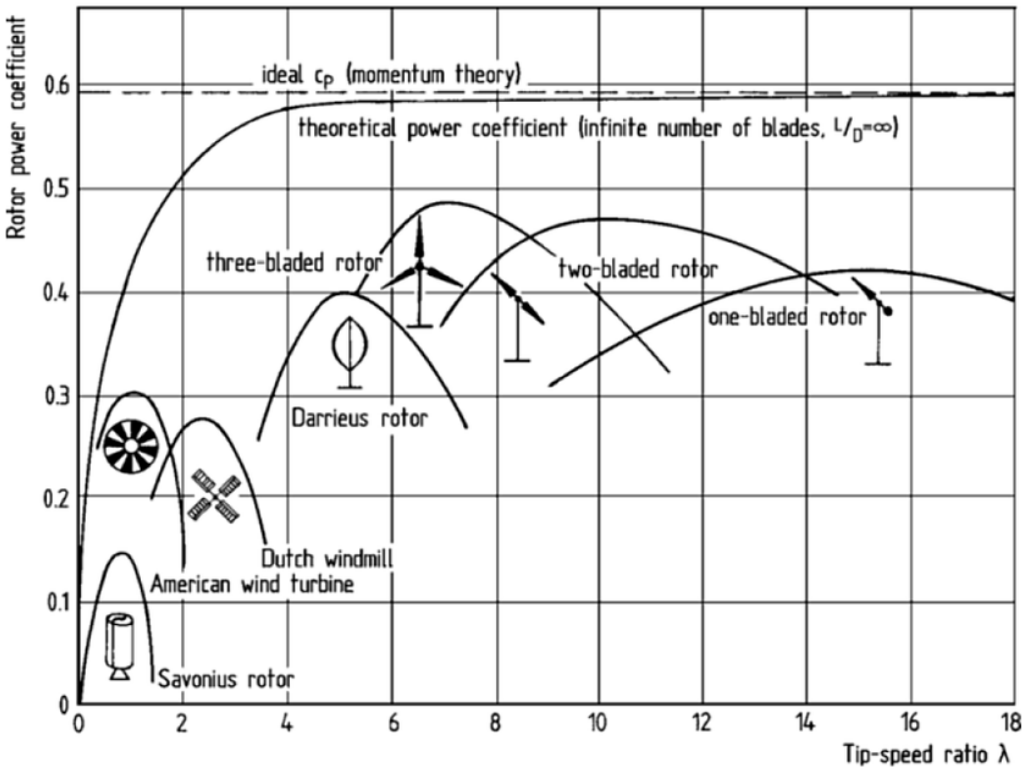

Figure 4.4: Power conversion efficiency and tip speed ratio relationship curve for different wind turbine designs [79].

speed. The power generated by a wind turbine can be expressed as:

$$P = \frac{1}{2}\rho\pi R^2 V^3 C_p(\lambda) \tag{4.1}$$

with ρ as the air density ($[kg/m^3]$), R as the turbine rotor radius, V as the wind speed, and $C_p(\lambda)$ is the turbine power coefficient.

$C_p(\lambda)$ represents the power conversion efficiency of a wind turbine and is a nonlinear function of the tip speed ratio λ given by:

$$\lambda = \frac{Rv}{V} \tag{4.2}$$

with v as the rotational speed of the wind turbine.

The rotor efficiency curve $C_p(\lambda)$ is determined by the blade design and the pitch angle and has a point of maximum. The maximum theoretically

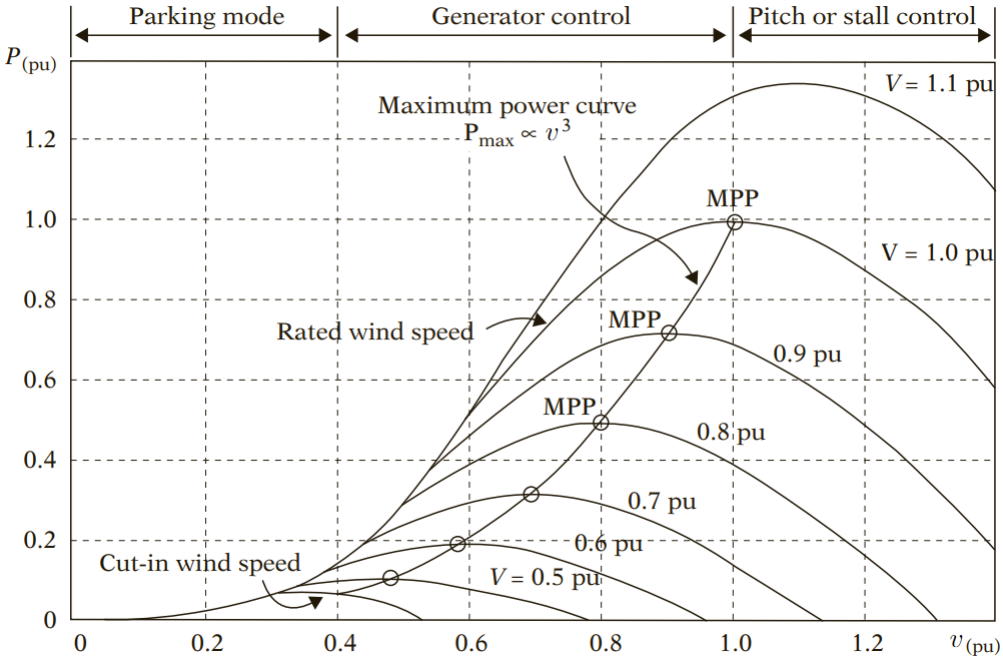

Figure 4.5: Wind turbine power-speed characteristics and maximum power point (MPP) curve (adapted from [80]).

possible turbine power coefficient is known as the Betz limit and has a value of $C_p(\lambda)_{theo} = 16/27$ [78]. $C_p(\lambda)$ and λ relationship is plotted for different wind turbine designs in Fig. 4.4.

Hence, for each wind velocity, there is a turbine speed that gives a maximum output power. Fig. 4.5 shows the developed power as a function of the turbine speed for different wind speeds. Values are expressed in per units, normalized on the rated speed and on the rated power. The maximum power points (MPP) are highlighted by the maximum power curve, which is provided by the manufacturer of the specific wind turbine.

In variable-speed operation, the rotor speed is controlled to keep it at the optimal one and and follow CP,max, thus, capturing the maximum power up to the rated speed. Fig. 4.6 shows an example of the relationship between wind speed and power generated by a given turbine. If the wind speed is below the cut-in speed, the turbine is not activated because the generated power would not be enough to compensate the losses. The range from cut-in

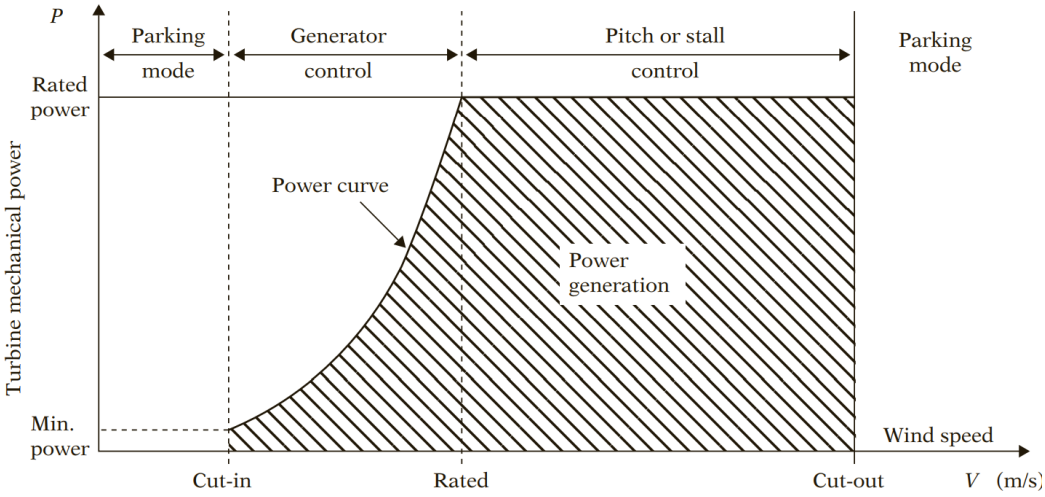

Figure 4.6: Output power of a wind turbine as a function of the wind speed (adapted from [80]).

speed and nominal speed is called optimal efficiency wind speed range, during which the rotor speed is adjusted to follow $C_{p,max}$ through electrical control of the generator. During this range, the delivered power is proportional to the cube of the wind speed. Between the nominal and the cut-out wind speed, power delivery is limited through mechanical control in order to avoid overloading. The system generates nominal power, which is also the rated output power of the generator. Once reached the cut-out speed, the turbine is stopped in order to avoid damages.

In order to practically achieve maximum power point tracking, many controls methods have been developed. Most of them, are based on feedback control in order to follow the optimal tip speed ratio or delivered power for the instantaneous wind speed. All of them, however, require an external anemometer to measure the wind speed, increasing the complexity and cost of the system. In some cases, the knowledge of the maximum power curve of the turbine might be required, which can be obtained through simulations and experimental tests. Another method is represented by the Hill Climbing Searching (HCS) control, similar to the one used in photovoltaic systems, where turbine speed and delivered power are monitored. When working in the optimal conditions, an increase in speed entails an increase in power too.

If this is not the case, then turbine speed should be decreased. However, in case of really large wind turbines, the speed adjustment is not fast, and this method could not be viable. Thus, a combination of many of the previous methods may be adopted [81]. Regardless of the specific method, tracking happens by a proper signal control for the power converter paired to the generator.

Generators and Power Converters Architecture

Wind turbine drivetrain systems are dominated by two types: the gearbox, with doubly fed induction generators (DFIG), and direct-drive systems, with permanent magnet synchronous generators (PMSG) and electrically excited synchronous generators (EESG). The most important factors in choosing between them are given by cost, power density, size, weight and reliability. In addition to that, the selection of the best suiting generator type changes between onshore and offshore applications. Specifically, offshore wind farms require cost-effective option over the turbine's total lifecycle because the logistics for regular maintenance takes more resources. Direct-drive systems have higher efficiencies, but, for large capacities, generators become heavier and larger. In this case, generator size can be reduced using permanent magnets that allow higher power density. Moreover, PM machines are superior to electricity-excited machines not only in terms of power-to-weight ratio but also efficiency and reliability. Thus, PMSGs have become the main generator technology for offshore wind turbine applications. In fact, in 2018, PMSGs were used in 76% of offshore wind turbines worldwide and almost all in Europe [82]. However, risks related to rare earth elements (neodymium and smaller quantities of dysprosium) supply for PM generators are raising concerns in the industry [83]. Some alternatives that make no use of permanent magnet exist, but they lack the efficiency and power density that is mandatory for offshore applications. Thus, it is crucial to diversify rare earth supply through global partnerships and innovation, as happens for other clean energy technologies.

Power electronic converters play a major role in wind power conversion

systems, especially for variable-speed configurations and PMSGs. In fact, synchronous generator requires a full-rated power electronic converter to decouple it from the grid. In addition to that, power electronics is essential to deal with the grid connections requirements that have been redefined with the recent expansion of wind farms. The converter must deal with harmonics and flickers but also contribute to frequency and voltage control by adjusting active and reactive power supplied to the grid. Thus, variable-speed drives with a full-scale power converter are the most effective and least complicated solution to achieve high efficiency in power conversion and active grid support.

Many power converter configurations have been researched, with the main one as the back-to-back voltage source converter (VSC), shown in Fig. 4.7. The total power production is fed to the system where the grid-side converter controls active and reactive power independently while the machine-side converter controls the generator at a wide variable frequency range for optimal operation. In simpler architectures, diode rectifiers can be used as the machine-side converters, but a complete control of the whole system may be more difficult. In addition to that, the use of current-source converters is being investigated too [84], [85].

The high-frequency switching of PWM modulation produce harmonics at high frequencies that can be easily removed by small-size filters. The size of the output filters can be reduced by other VSC configurations that produce

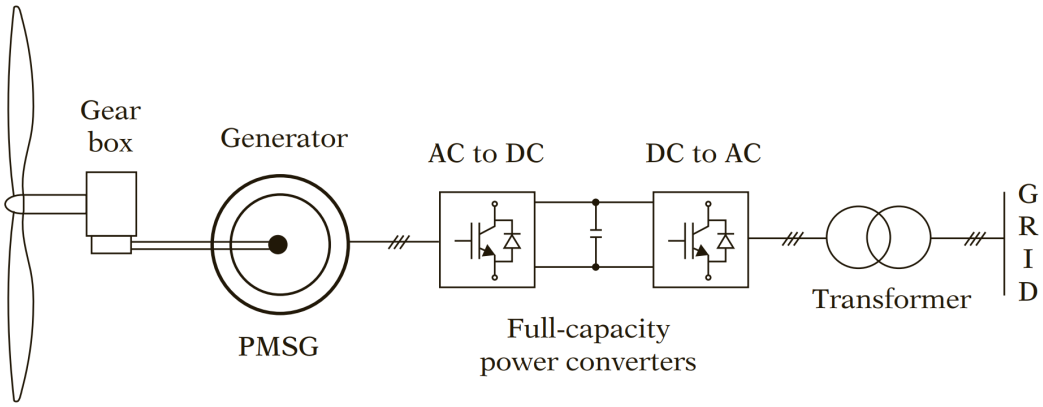

Figure 4.7: Variable-speed system with PMSG and full-scale back-to-bac VSC [80].

less harmonic content, such as matrix and multilevel converters. The matrix converter represents a compact solution to achieve direct AC-AC conversion with reduced component count but is technically more complicated. The multilevel converters, on the other hand, are very interesting thanks to their ability to satisfy the high voltage ratings of the conversion system with low voltage devices. In fact, the power rating of offshore wind energy conversion systems is growing steadily. As known, large current rating causes high power losses. In order to keep a low current rating, therefore, the voltage rating of the system must increase. As a result, devices with higher voltage rating must be used, causing an increase in the overall costs and a decrease in dynamic performance due to the low switching frequency of high voltage rating devices.

An attractive alternative for variable-speed drives of wind turbine may be represented by the dual inverter system paired to an open-end permanent magnet synchronous generator. Detailed description of architecture will be presented in the following section.

4.2 Dual Inverter Fed Open-End Winding Permanent Magnet Synchronous Motor

4.2.1 Features and Applications of the Drivetrain

In a dual inverter fed Open-End Winding Permanent Magnet Synchronous Motor (OW-PMSM), the neutral point of the stator windings is opened and each phase is controlled separately by the legs of two different inverters. The two inverters can be linked to different voltage sources or to the same DC bus, as shown in Fig. 4.8. This may look as a more complex scheme but presents several advantages with respect to a conventional single inverter drive that make it advantageous in some specific applications.

First of all, a three-level modulation effect is obtained without the use of a neutral point clamping (NPC) diode, eliminating the fluctuation issues that affect three-level NPC inverters [86].

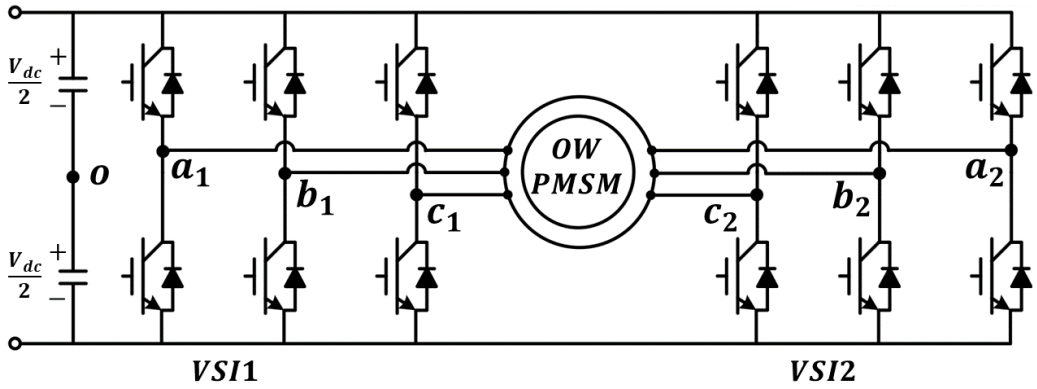

Figure 4.8: Open-end winding permanent magnet motor fed by a dual inverter with common DC bus.

Secondly, this configuration allows to increase the DC bus utilization up to double the one of a single inverter. Thus, DC voltage can be reduced by half reducing the stress on switching devices and increasing the energy density [87]. Thanks to this feature, this drive scheme gained particular interest for electric vehicles applications [88], [89], [90].

Finally, this system has an interesting fault-tolerant capability [91], [92], [93]. In fact, each phase current can be controlled separately and there is a redundancy of space vector combinations, as it will be presented in the following sections. If one inverter fails, the other can operate as a standard two-level VSI by shorting the output terminals of the faulty one [88], [94].

Advantages for Wind Power Conversion Applications

The peculiar features of the OW-PMSM coupled to a dual inverter make this architecture an interesting solution for wind turbine drivetrains. In this topology, the number of voltage levels that can be applied both on the machine-side and grid-side doubles, allowing several benefits.

First of all, power sharing between the two inverters is improved and higher power output is achieved, which is particularly useful in high-power wind turbine applications.

Secondly, DC bus voltage can be reduced by half, thus, reducing the stress on the components. Lower-rated and faster switching devices can be used

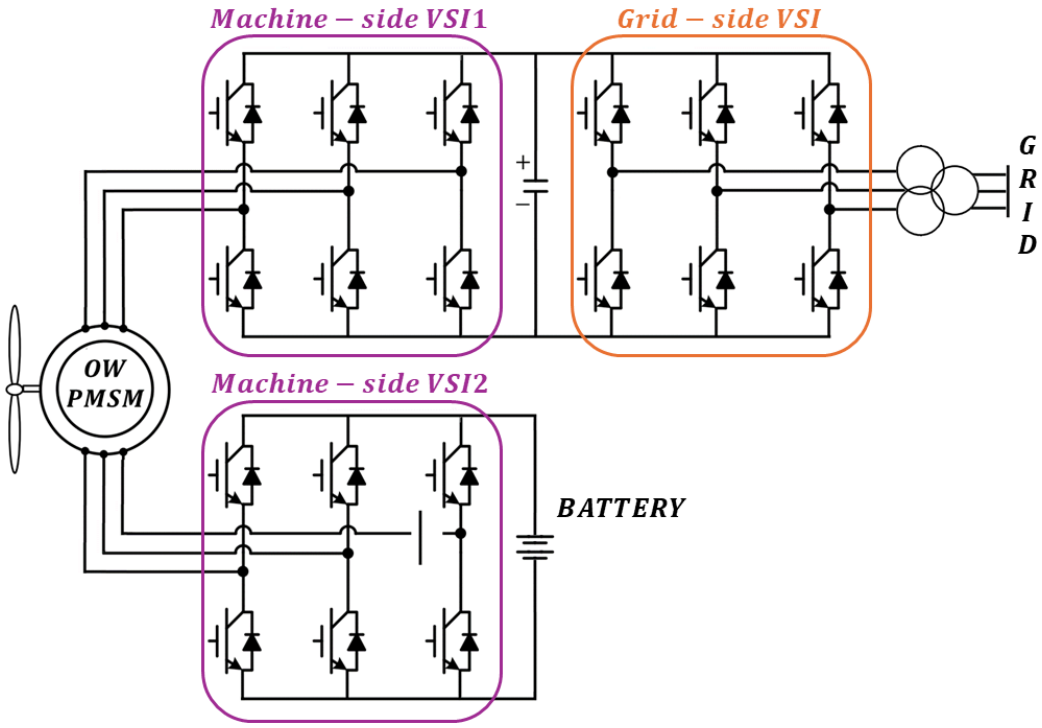

Figure 4.9: Energy storage integration in a turbine drive with a dual inverter fed OW-PMSM (adapted from [95].)

compared to a single inverter setup, resulting in reduced system costs and improved performance.

Moreover, thanks to the higher number of levels, the total harmonic distortion of the output signals is improved. This is highly beneficial on grid-side especially, improving the quality of the power fed into the transmission grid.

Finally, the dual inverter system introduces redundancy, which can be crucial in wind power systems. In case of fault in one inverter, the system can still operate at reduced capacity using the remaining healthy inverter, thus improving the reliability of the wind power conversion system.

Some works adopting the dual inverter structure and the OW-PMSM for wind power conversion applications can be found in literature In [96], the dual inverter architecture was adopted to feed a brushless doubly fed turbine generator. In [97], OW-PMSM was used as a turbine generator and was coupled to a series multilevel converter. Both dual inverter and OW-PMSM are used in [95]. This drivetrain exploits the dual inverter structure on the

machine side for efficient energy storage integration. One inverter feeds the DC bus while the other feeds a battery, as shown in Fig. 4.9. Finally, in [98], the dual inverter structure was adopted both on the machine-side converter and on the grid-side converter to make the most of all its advantages. In addition to that, in this configuration all the converters share the same DC bus, as shown inf Fig. 4.10. The common DC bus architecture allows a more compact and simple structure, highly advantageous given the limited space available on turbine's nacelle. However, the common DC bus presents some challenges that must be dealt with proper modulation of the converters.

Drawbacks of the Common DC-Bus Configuration

The dual inverter fed OW-PMSM architecture poses two main challenges.

The first one is caused by the use of a common DC bus. In fact, with this topology a path for the circulation of a zero sequence current (ZSC) is opened. This path has a low equivalent inductance and is not able to filter out the high frequency components of the ZSC which are triple the

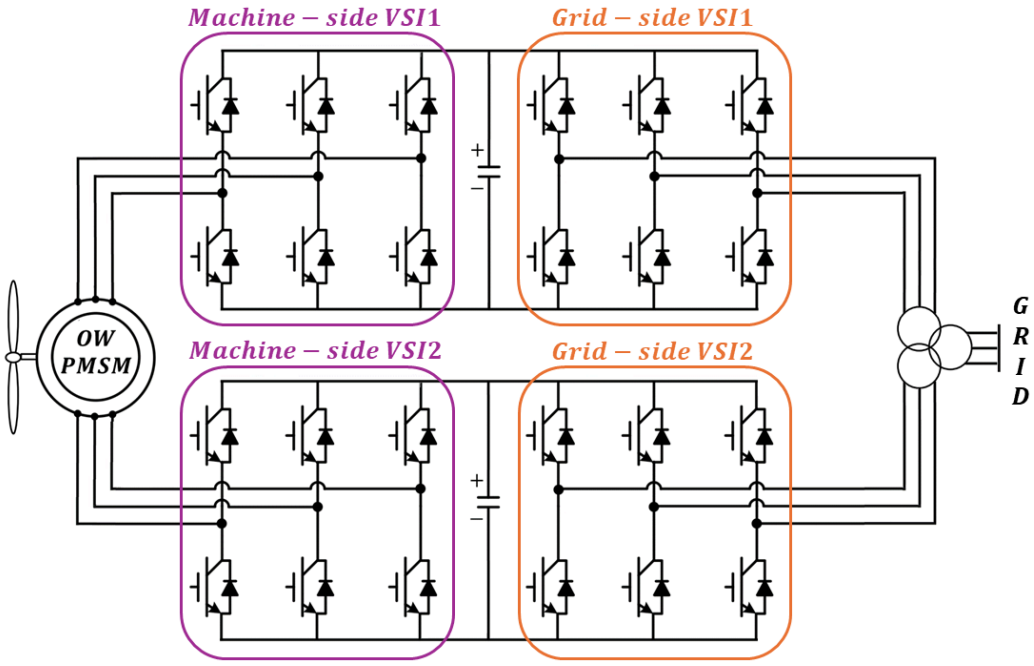

Figure 4.10: Turbine drive with OW-PMSG and dual inverter both on machine-side and grid-side (adapted from [98].)

fundamental frequency and change with the operating speed [99]. Thus, high-frequency, high-magnitude current ripple is produced which translates in a torque ripple at six-times the fundamental frequency [100]. Whether the ZSC magnitude is acceptable, it depends on the machine parameters, but this usually causes a significant degradation of the performance of the system. In order to suppress circulation of the ZSC, the common mode voltage difference at the ends of the ZSC path must be minimized. This zero sequence voltage (ZSV) is generated by different sources.

First of all, a main source comes from PWM modulation itself. It is represented by the difference between the common mode voltages of the two inverters and can be directly controlled through proper modulation.

Secondly, ZSV is generated by the third harmonic component of the back electromotive force (EMF). This is a specific problem arising from the application of the dual inverter to an OW-PMSM [101].

Finally, other minor ZSV sources derive from the cross-coupling voltages in the ZSC path caused by the d- and q-axis currents and from the dead time and voltage drop of switching devices [102], [103].

Compensation of all these different sources can be achieved by introducing some changes in the conventional PWM modulation of the inverters. The common approach consists in tuning the first directly controllable PWM source to counteract the other ZSV source. Typically, a PWM modulating signals 120° rotation is adopted to obtain the same common mode voltage in the two inverters [104], [103]. Thus, the major ZSV source is eliminated, and the other disturbances become easier to counteract. After this, modulating signals are tuned to further modulate the common mode voltages of the two inverters. This is carried out by redistributing the dwell times of the zero vectors only, because the final phase voltages applied to the windings must not be affected. In fact, the dwell time of the active vectors determine inverter's voltage output while the ZSV is determined by the dwell time of the two zero vectors. This technique is known as zero vector dwell time redistribution (ZVR).

Many variants of this method can be found in the literature. In [100] ZSV is modulated by redistributing the dwell time between zero vectors (000) and

(111) with Space Vector PWM (SVPWM). In [105], instead, this is achieved by signals phase shifting with Sinusoidal PWM (SPWM). Both methods use opposite reference voltages for the two VSI instead of 120° phase-shift rotation, with a semi-PR controller generating the ZSV reference in order to suppress ZSC. In both cases, the available modulation range for the ZSV reference is limited: it reduces as the modulation index increases.

Modulating ZSV with these techniques, however, requires more switching actions, hence, increases the switching losses. This has a relevant impact for the dual inverter architecture, especially. In fact, another main drawback of this topology is that losses are double the ones of a conventional single inverter. For this reason, in previous works, many methods have been attempted to reduce the switching losses of this system. In [87], different technologies are utilized for the two VSI. VSI1 is IGBT-based and is modulated 6-step with a low switching frequency, hence, its common mode voltage is predictable. VSI2 is SiC-based and is SVPWM modulated at high switching frequency to act as an active filter and compensate both the high harmonics introduced by 6-step modulation of VSI1 and its common mode voltage. Instantaneous ZSV is compensated but the other ZSV disturbances are not addressed. In [106], ZSC is assumed to be relatively small and negligible in a certain range, hence, it is not suppressed. Resulting torque ripple is eliminated by injecting a reference current in the 0-axis controller to counteract the effect of ZSC. In this way, switching losses decrease but there is an increase in losses due to current distortion: convenient for heavy load and high switching frequency applications. [91], [92], [93].

An alternative to reduce switching losses is to adopt discontinuous (DPWM) schemes [107]. In [108] and [109], DPWM was successfully adopted but in a OW induction motor (OW-IM) only. The OW-IM is not subject to the third harmonic component of the back-EMF, hence, the suppression of the instantaneous ZSV is sufficient. For an OW-PMSM, however, ZSV is mandatory to guarantee the proper operation of the system but it is more difficult to achieve with DPWM. In fact, less degrees of freedom are available with DPWM: in each switching period, only one of the two available zero voltage vectors is used. Thus, in order to modulate the ZSV without changing the

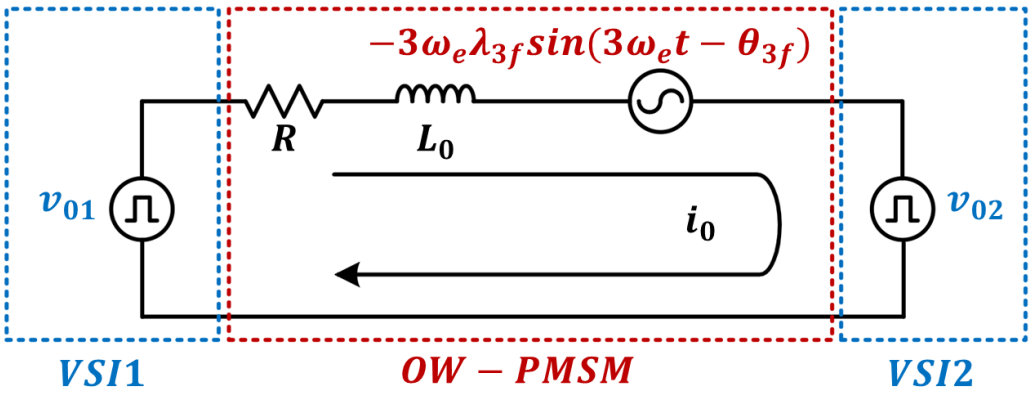

Figure 4.11: Zero-sequence equivalent circuit with ZSV sources: PWM modulation (blue) and third harmonic back-EMF (red).)

final phase voltages applied to the motor, thorough analysis and complex modulating signal tuning are required.

In the following section, the analytical model of the complete system will be presented in detail. Moreover, a technique to achieve ZSV modulation with DPWM in the dual inverter fed OW-PMSM will be proposed.

4.2.2 Modeling of the Complete System

Mathematical Model of OW-PMSM

In an OW-PMSM, the flux linkage harmonics produce zero-sequence harmonics in the back-EMF, with the third harmonic component as the dominating one. Considering a $dq0$ rotating reference frame, the flux equations can be expressed as:

$$\begin{bmatrix}\lambda_d\\ \lambda_q\\ \lambda_0\end{bmatrix} = \begin{bmatrix}L_d & 0 & 0\\ 0 & L_q & 0\\ 0 & 0 & L_0\end{bmatrix}\begin{bmatrix}i_d\\ i_q\\ i_0\end{bmatrix} + \begin{bmatrix}\lambda_f\\ 0\\ \boldsymbol{\lambda_{3f}cos(3\omega_e t-\theta_{3f})}\end{bmatrix} \tag{4.3}$$

with L_d, L_q, L_0, i_d, i_q and i_0 as the inductances and currents components in the $dq0$ reference, λ_f and λ_{3f} as the amplitudes of fundamental and third harmonic flux linkages, and ω_e as the electrical angular speed of motor. In

case of an interior PMSM, the fundamental and third harmonic flux linkages are not in phase [110]. Hence θ_{3f} represents the phase lag between the fundamental and third harmonic flux linkages. The voltage equations in the $dq0$ frame can be expressed as:

$$\begin{cases} v_d = L_d \frac{di_d}{dt} + Ri_d - \omega L_q i_q \\ v_q = L_q \frac{di_q}{dt} + Ri_d + \omega(L_d i_d + \lambda_f) \\ \boldsymbol{v_0 = L_0 \frac{di_0}{dt} + Ri_0 - 3\omega_e \lambda_{3f} sin(3\omega_e t - \theta_{3f})} \end{cases} \tag{4.4}$$

with R as the stator resistance.

Because of the open neutral point, a ZSC path allows circulation of i_0. Additionally, because of the negative mutual inductance, the $0-$axis inductance is smaller than the $d-$ and $q-$axis inductances [105], hence, i_0 is easily generated by any v_0 disturbances. The ZSV v_0 and ZSC i_0 can be expressed as:

$$\begin{cases} v_0 = (v_a + v_b + v_c)/3 \\ i_0 = (i_a + i_b + i_c)/3 \end{cases} \tag{4.5}$$

where v_a, v_b, v_c are the phase voltages and i_a, i_b, i_c the phase currents of the motor.

The ZSC circuit is schematized in Fig. 4.11 where ZSV sources are represented as equivalent generators: inverters' CMV disturbance due to PWM modulation v_{01} and v_{02} (blue) and third harmonic component of the back-EMF (red).

Finally, the electromagnetic torque can be expressed as:

$$T = \frac{3}{2} P[\lambda_f i_q + (L_d - L_q) i_d i_q \boldsymbol{- 6\lambda_{3f} sin(3\omega_e t - \theta_{3f}) i_0}] \tag{4.6}$$

with P as the pole pairs number.

ZSC generates a six times the fundamental frequency torque ripple, which is harmful for the operation and mechanical components of the motor and causes extra power loss for the system. Hence, ZSC suppression is required for proper operation.

Dual Inverter Space Vector Model

With the dual inverter configuration, the phase voltages v_a, v_b and v_c applied to the stator's windings are given by the difference between the pole voltages generated by the two inverters, as follows:

$$\begin{bmatrix} v_a \\ v_b \\ v_c \end{bmatrix} = \begin{bmatrix} v_{a1} - v_{a2} \\ v_{b1} - v_{b2} \\ v_{c1} - v_{c2} \end{bmatrix} \tag{4.7}$$

where 1 subscript stand for VSI1 and 2 for VSI2. The ZSV due to modulation can therefore be expressed as the difference between the two inverters' CMVs v_{01} and v_{02}:

$$v_0 = v_{01} - v_{02} = \tag{4.8}$$
$$= \frac{v_{a1} + v_{b1} + v_{c1}}{3} - \frac{v_{a2} + v_{b2} + v_{c2}}{3} = \frac{v_a + v_b + v_c}{3}$$

Each pole voltage is controlled by the corresponding inverter leg's switching state, hence, for the dual inverter, there are $2^6 = 64$ switching states generating 19 different state vectors on the space vector plane, as in a three-level inverter. These state vectors are shown in Fig. 4.12 as the vertices of the black, orange and dashed hexagons plus zero vector at the origin. In order to obtain a zero ZSV, however, only the combinations of VSI1 and VSI2 state vectors with the same CMVs can be used. Hence, the number decreases to 6 active vectors at the vertices of the orange hexagon and one zero vector at the origin. The corresponding state vector couple for single inverters is indicated in red for VSI1 and blue for VSI2. In order to synthesize the 7 zero ZSV state vectors, the 120° phase shift is adopted so that the two inverters have the same common mode voltage. Specifically, the reference vectors of the two single inverters are leading the total reference vector by 30° and 150° for VSI1 and VSI2, respectively. The opposite sequence can be adopted too, with a 30° lag for VSI1 and 150° lag for VSI2. It must be noted, however, that with this choice the voltage utilization of the DC bus is reduced by about 13%. The dual inverter would allow twice the voltage utilization of the single inverter, while with the 120° phase shift it is limited to $\sqrt{3}$ times. Still, the

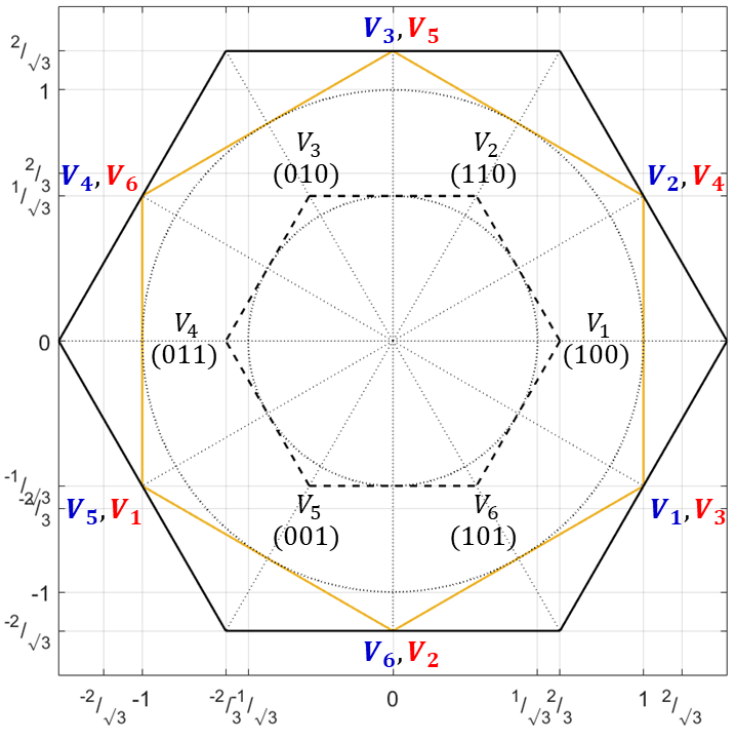

Figure 4.12: State Vectors on the space vector plane for single inverter (dashed hexagon) and dual inverter (solid hexagon). Dual inverter state vectors with zero ZSV belong to the orange hexagon. Values are normalized over Vdc.

voltage utilization is higher than in the single inverter case. The radius of the circle inscribed in the hexagons indicates the maximum amplitude of the space voltage vector under the linear modulation range, which is $V_{dc}/\sqrt{3}$ for the single inverter and V_{dc} for the dual inverter.

As a summary, VSI1 and VSI2 reference vectors can be generated as:

$$V_{VSI1} = (1/\sqrt{3}) \cdot V_{tot} \cdot e^{\pi/6}$$

$$V_{VSI2} = (1/\sqrt{3}) \cdot V_{tot} \cdot e^{5\pi/6} \tag{4.9}$$

with $V_{tot} = V_{VSI1} - V_{VSI2}$ as the total reference vector.

Once the major ZSV source is eliminated with 120° phase shift reference voltage generation, it is possible to further modulate the ZSV in order to counteract the back-EMF effect and suppress ZSC. How to achieve this depends on the chosen PWM modulation method.

4.2.3 A New Modulation Strategy for Losses Reduction

DPWM Modulation for Switching Losses Reduction

In DPWM schemes, phase voltages are periodically and alternately clamped to $V_{dc}/2$ and $-V_{dc}/2$ for a total of 120° in a fundamental period. Thus, each phase ceases switching for one-third of the time and this allows a reduction in switching losses with respect to continuous PWM.

Generalized DPWM60 methods are parameterized by the modulator phase angle ψ which represents the distance from the intersection of the two reference phase voltages (60°) to the start of the voltage clamping. For example, DPWM60-0, DPWM60-1 and DPWM60-2 are obtained with a ψ value fixed to 0°, 30°, and 60°, respectively. Once ψ is set, a zero-sequence signal is computed and added to the three original modulation signals to obtain DPWM60 reference voltages. An extensive explanation can be retrieved in [107].

In the proposed method, optimal DPWM60 was adopted. In this case, ψ is varied depending on the power factor angle to start the clamping around current peaks and, hence, to maximize the switching loss reduction [111]. Given ϕ as the power factor angle, ψ can be computed as follows:

$$\psi = \begin{cases} 0 & \text{if } -\pi/2 \leq \phi < -\pi/6 \\ \phi + \pi/6 & \text{if } -\pi/6 \leq \phi < \pi/6 \\ \pi/3 & \text{if } \pi/6 \leq \phi < \pi/2 \end{cases} \tag{4.10}$$

If DPWM60 scheme was independently applied to both inverters, different optimal angles would be used for VSI1 and VSI2. In fact, because of the 120° phase shift, the power factor angles of VSI1 and VSI2 lead the total ϕ by 30° and -30°, respectively. This solution would maximize switching loss reduction but the CMVs of the two inverters would be different, hence, ZSV would no be suppressed. For this reason, the same optimal angle ψ has been adopted for both inverters, as presented in [109].

ZSV Modulation for ZSC Suppression

As previously stated, once the common mode voltage difference between the two VSIs is suppressed, the ZSV can be further tuned in order to counteract the other ZSC sources. The main source is represented by the third harmonic back-EMF component, whose frequency changes with the operating conditions. In order to suppress the tracking error, a proportional-resonant (PR) controller was chosen to generate the target ZSV v_0^*, as presented in [100]. The ZSC i_0 is computed as one third the sum of the measured phase currents while the reference i_0^* is set to 0. The error is fed to the PR controller, with resonant frequency set to three-times the fundamental one and cut-off

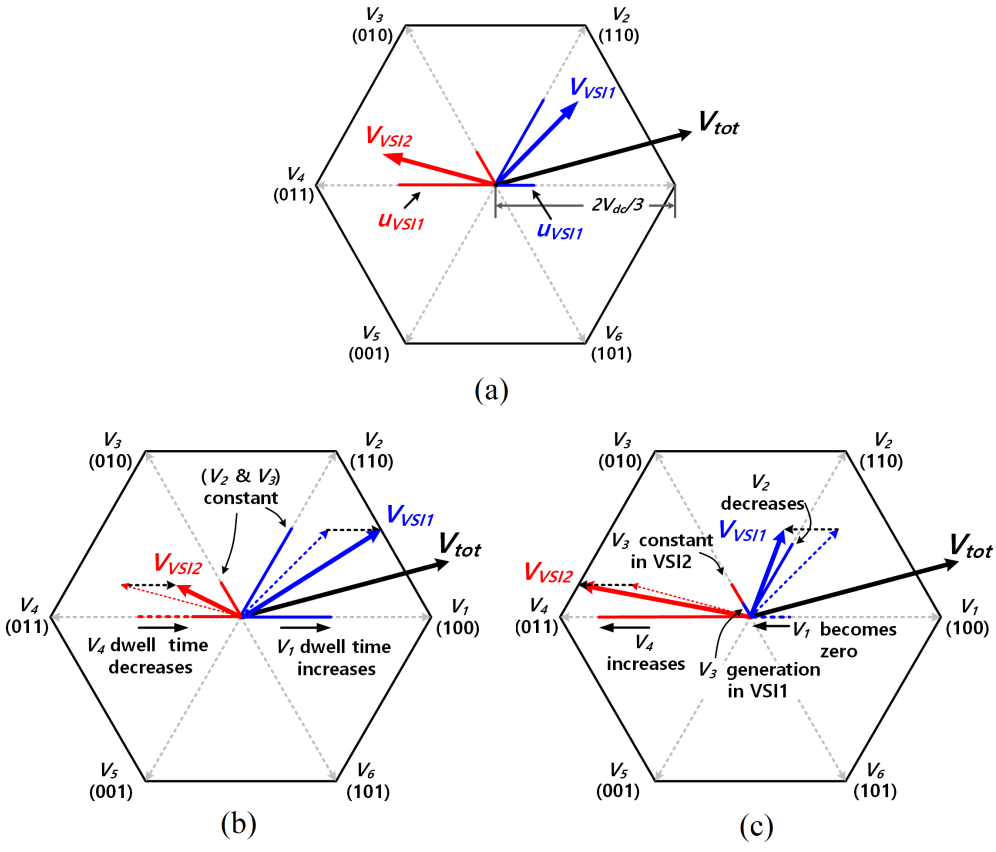

Figure 4.13: V_{tot} (black), V_{VSI1} (solid blue) and V_{VSI2} (solid red), with their components on the space vector plane (dashed). u_{VSI1} (blue dashed) and u_{VSI2} (red dashed) are varied and V_{tot} is unaffected. Before ZSV modulation (a), after ZSV>0 modulation (b) and after ZSV<0 modulation (c).

frequency set to 2-5 [rad/s].

With the conventional solutions adopting SVPWM, the ZSV reference v_0^* is obtained thanks to ZVR. In fact, the dwell times for zero vectors switching states (000) and (111) are equally divided in SVPWM. By adopting DPWM, however, only one of the two states is applied in each switching time, hence, there are less degrees of freedom.

Considering a single VSI, if the zero vector dwell time is varied, also the dwell time of one of the two active vector will vary, affecting the final output voltage vector. To overcome this issue, both VSIs should be considered at the same time, remembering that the final voltage vector applied to the motor windings is the difference between VSI1 and VSI2 vectors, as in Eq. (4.8).

Fig. 4.13a shows the total output voltage vector V_{tot} decomposed between the single VSI1 and VSI2 reference vectors, V_{VSI2} and V_{VSI2}, respectively. Both vectors have two components on the state vectors of the space vector plane. From this example, it is possible to see that if only the opposite components, denoted as u_{VSI1} and u_{VSI2}, are changed in the opposite way, the final output vector will not be affected. The single V_{VSI1} and V_{VSI2} will rotate but their sum V_{tot} will not change, as visible in Fig. 4.13b and Fig. 4.13c. In the figure, a positive target ZSV has been considered; in case of a negative ZSV, the components should be varied in the opposite way. In Fig. 4.13b, a positive target ZSV has been considered, hence, u_{VSI1} is increased and u_{VSI2} is decreased. In Fig. 4.13c, a negative target ZSV has been considered, hence, u_{VSI1} is decreased and u_{VSI2} is increased.

With proper expedients, it is possible to change the dwell time of the ac-

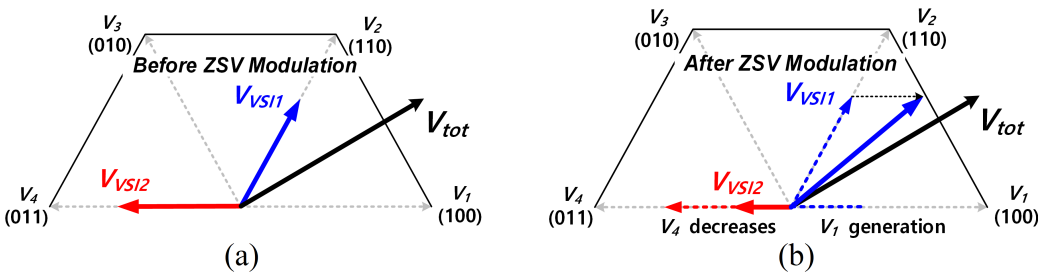

Figure 4.14: Special condition when V_{tot} phase angle is $\pi/6$: before (a) and after (b) ZSV modulation.

tive vectors without changing the resulting V_{tot}. This allows ZSV modulation in a similar manner to ZVR method.

There are some special conditions that should be considered separately. These happens when V_{tot} phase angle is an integer multiple of $pi/6$: V_{VSI2} and V_{VSI2} have no components but lie on one single state vector. In this case, one of the two vectors is directly changed while for the other one an opposite component is generated, as shown in Fig. 4.14.

Fig. 4.15a shows the PWM waveforms of both inverters during one switching time T_{sw}, along with their CMVs and the final ZSV (reference dashed line is placed at $0V$). In this example, DPWM60-1 method was considered with V_{tot} positioned in the space vector plane as in Fig. 4.13. In this condition, phase $c1$ and $a2$ are clamped to $-V_{dc}/2$ and only zero voltage vector switching state (000) is available. As visible, with the 120° reference signal

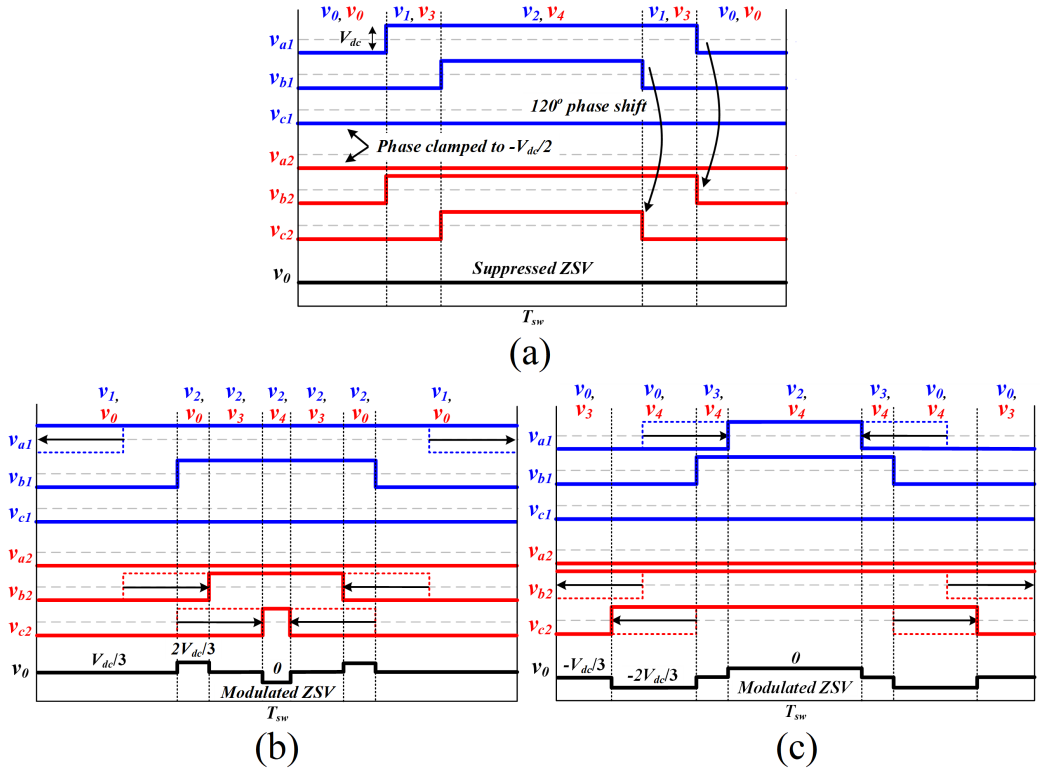

Figure 4.15: PWM waveforms during one switching time. Phase voltages of VSI1 (blue) and VSI2 (red) with CMVs of both inverters and total ZSV (black).Before ZSV modulation (a), after ZSV>0 modulation (b) and after ZSV<0 modulation (c).

rotation, the CMVs of the two inverters are equal and ZSV is suppressed.

In order to obtain a positive ZSV, u_{VSI1} should increase and u_{VSI2} should decrease, while the other two components must remain constant, as shown in Fig. 4.15b. In terms of dwell times, this means:

- For VSI1: decreasing the zero vector dwell time and increasing the active vector V_1 dwell time;
- For VSI2: increasing the zero vector dwell time and decreasing the active vector V_4 dwell time.

Hence, ZSV can be modulated until phase $a1$ duty cycle becomes 1 (zero vector dwell time becomes null) and until phase $c2$ duty cycle becomes 0 (V_4 dwell time becomes null).

In case of a negative ZSV, dwell times should be varied in the opposite way , as shown in Fig. 4.15c. Modulation is achievable until the duty cycle of phase $a1$ becomes 0 or that of $b2$ becomes 1. As the duty of phase $a1$ decreases, the active vector V_1 dwell time is reduced. When the duty of phase $a1$ and $b2$ are the same, V_1 dwell time totally disappears. As the duty of phase $a1$ further decreases, the active vector V_3 is generated and V_2 dwell time is reduced. Keeping in mind the geometry of the space vector plane, a decrease in V_2 can be considered as an increase in V_5. The sum of V_3 and V_5 generates the V_4 component. This cancels out the V_4 increase in VSI2. Therefore, the final V_{tot} does not change.

In this work, carrier-based principle is adopted for DPWM modulation [107]. The addition or subtraction of a zero-sequence signal shifts the reference signal in the vertical direction. Hence, changing the dwell times to modulate the ZSV means injecting the reference v_0^* to the phase reference signals. For this example, v_0^* is subtracted to both v_{b2}^* and v_{c2}^* reference signals of VSI2 and added to v_{a1}^* only for VSI1.

Generally, this procedure depends on sector and phase clamping, hence, on the runtime phase angle of V_{tot} . The rules can be summarized in the following:

1) In Sectors I, III, V:

- If Phase Clamping to $V_{dc}/2$:
  - Add v_0^* to all non-clamped VSI1 Reference Signals
  - Subtract v_0^* only to the lowest VSI2 Reference Signal
- If Phase Clamping to $-V_{dc}/2$:
  - Add v_0^* only to the highest VSI1 Reference Signal
  - Subtract v_0^* to all non-clamped VSI2 Reference Signals

2) In Sectors II, IV, VI:

- If Phase Clamping to $V_{dc}/2$:
  - Add v_0^* only to the lowest VSI1 Reference Signal
  - Subtract v_0^* to all non-clamped VSI2 Reference Signals
- If Phase Clamping to $-V_{dc}/2$:
  - Add v_0^* to all non-clamped VSI1 Reference Signals
  - Subtract v_0^* only to the highest VSI2 Reference Signal

ZSV modulation, therefore, is limited by how much the reference signals can be increased or decreased before reaching the clamping condition. The positive margin up to $V_{dc}/2$ and the negative margin down to $-V_{dc}/2$ are computed for all the reference signals that will be modified. The minimum of these margin represent the ZSV modulation limit. For the example case considered in Fig. 4.13b and Fig. 4.15b:

$$\begin{cases} \delta_{a1}^{+} = V_{dc}/2 - v_{a1}^{*} \\ \delta_{b2}^{+} = V_{dc}/2 - v_{b2}^{*} \\ \delta_{c2}^{+} = V_{dc}/2 - v_{c2}^{*} \end{cases} \quad \begin{cases} \delta_{a1}^{-} = -V_{dc}/2 + v_{a1}^{*} \\ \delta_{b2}^{-} = -V_{dc}/2 + v_{b2}^{*} \\ \delta_{c2}^{-} = -V_{dc}/2 + v_{c2}^{*} \end{cases} \tag{4.11}$$

$$lim^{+} = min(\delta_{a1}^{+}, -max(\delta_{b2}^{-}, \delta_{c2}^{-}))$$

$$lim^{-} = max(\delta_{a1}^{-}, -min(\delta_{b2}^{+}, \delta_{c2}^{+}))$$

with δ_{a1}^{+}, δ_{b2}^{+}, δ_{c2}^{+} as the positive margins for v_{a1}^{*}, v_{b2}^{*}, v_{c2}^{*} reference signals, δ_{a1}^{-}, δ_{b2}^{-}, δ_{c2}^{-} as the negative margins and lim^{+}, lim^{-} as the positive and negative limits for ZSV modulation, respectively.

As visible, ZSV modulation in case of DPWM is more complex than in the SVPWM case. In SVPWM method, $v_0^*/2$ is evenly added and subtracted to all the six pole reference signals. With DPWM, instead, v_0^* is added and subtracted to three selected pole reference signals only. For this reason, modulation limits for ZSV modulation depend not only on the chosen modulation index and V_{tot} phase angle, but also on the selected clamping angle. In case of optimal DPWM60, this means that the limits will vary with the output power factor, hence, the operating condition of the electric machine.

Fig. 4.16 and Fig. 4.17 show lim^{+} (blue) and lim^{-} (orange) for different values of V_{tot} modulation index and phase angle, for DPWM60-0 and DPWM60-1, respectively. Limits profiles for DPWM60-2 are the same as DPWM60-1 but flipped horizontally. ZSV modulation limits and V_{tot} modulation index m are normalized over V_{dc}. The sectors and the different phase clamping regions are denoted in the top of the picture: pink for phase a, green for phase b and yellow for phase c, with positive clamping (solid lines) and negative clamping (dashed lines).

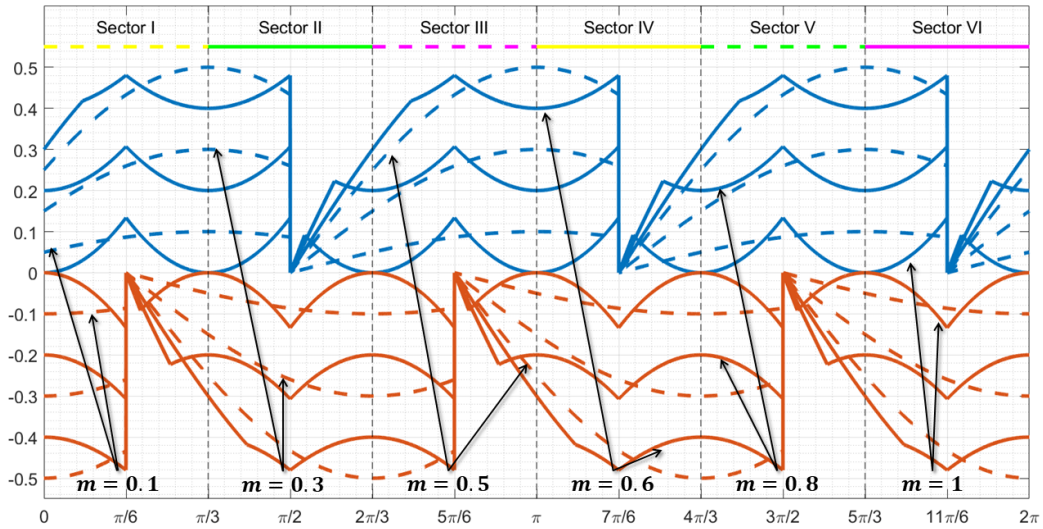

Figure 4.16: ZSV modulation limits as a function of V_{tot} modulation index and phase angle with DPWM60-0.

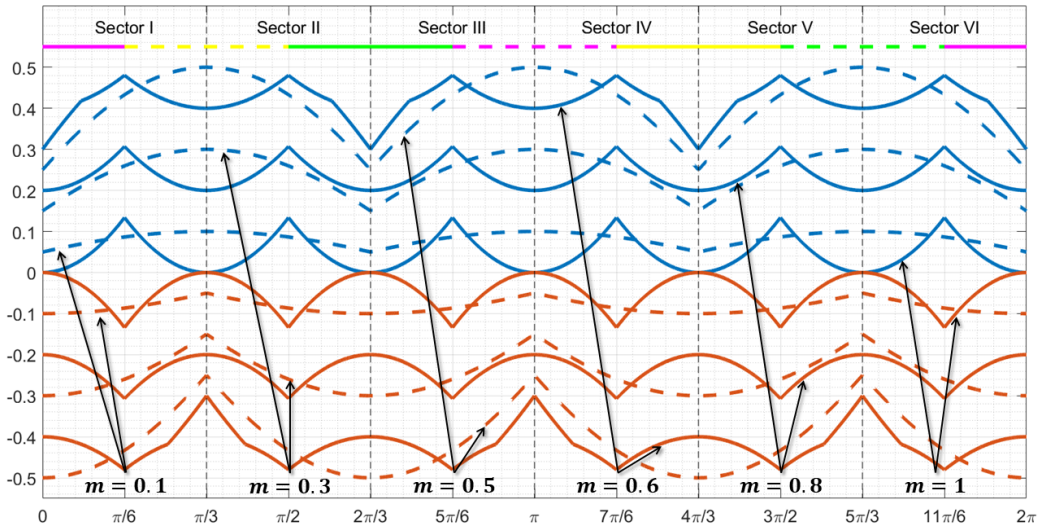

Figure 4.17: ZSV modulation limits as a function of V_{tot} modulation index and phase angle with DPWM60-1.

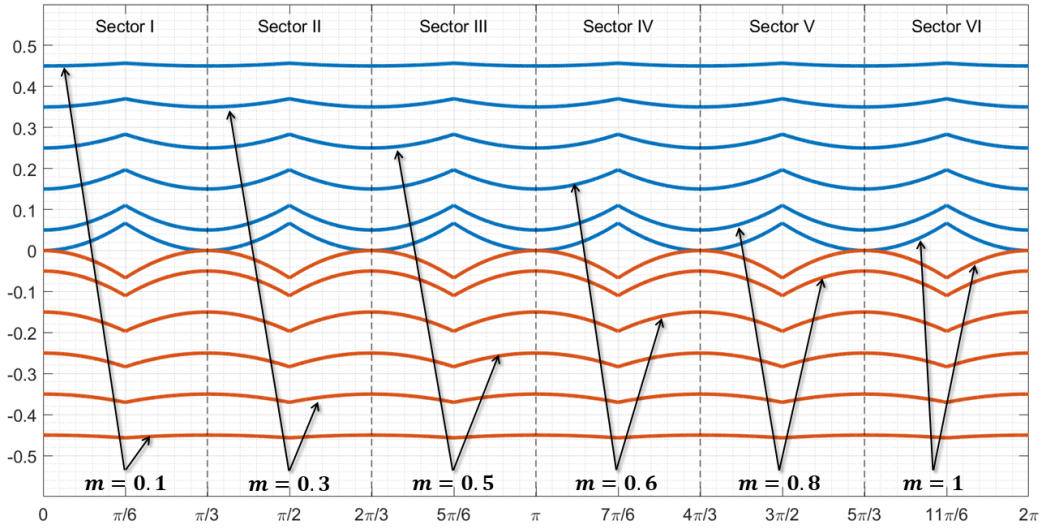

Figure 4.18: ZSV modulation limits as a function of V_{tot} modulation index and phase angle with SVPWM.

ZSV modulation limits are narrow for low values of m and increase with medium m values. When m is higher than about 0.5, however, ZSV modulation limits shrink again. That is because ZSV modulation relies not only on zero vector dwell times, as in ZVR, but also on the active vectors' ones.

For comparison, Fig. 4.18 shows ZSV modulation limits in case of con-

ventional SVPWM. As visible, in this case, ZSV modulation limits shrink for higher Vtot modulation indexes. That is because, for lower Vtot modulation indexes, zero vector dwell times are longer, hence, there is more margin for zero vector dwell time redistribution.

In addition to that, for DPWM60-0 and DPWM60-1, there are periodical discontinuities where the limits become zero. That is because one of the reference signals to be modified has a null margin in that instant. This means that, in these time instants, it is not possible to modulate ZSV. These cases represent the extremes for the optimal angle. For lower ψ values, the discontinuities are gradually smoothed out, finally reaching DPWM60-1, the most convenient condition in terms of modulation limits ($\psi = \pi/6$). Hence, if v_0^* is not within the runtime computed limits, it is possible to reduce *psi* to extend them. An algorithm to change ψ at runtime is proposed in the following section. With this choice, however, for high power factor angles sub-optimal DPWM60 is used, representing a trade-off between switching losses minimization and ZSV modulation capability.

Complete Control Scheme

The complete control of the OW-PMSM with dual inverter is summarized by the block scheme of Fig. 4.19. As previously stated, 0-axis current reference is set to 0 and the error is fed to a PR regulator in order to obtain reference v_0^* for ZSV modulation. Speed control is achieved with q-axis reference current i_q^* generation, while i_d^* is set to 0. The error between reference and measured current is fed to PI regulators with back-EMF compensation for

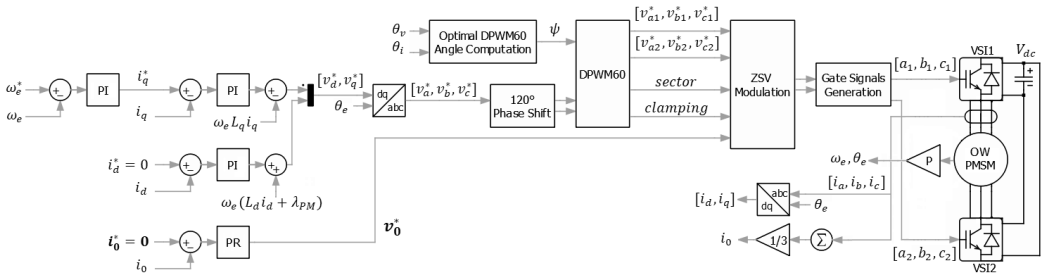

Figure 4.19: Complete control block scheme for the system.

axis decoupling and the reference stator phase voltages v_a^*, v_c^* and v_c^* are obtained. From these, 120° phase shift rotation to suppress ZSV is performed and the reference waves for VSI1 and VSI2 generated. Power factor angle is computed at runtime in order to obtain the optimal angle ψ and generate DPWM60 waveforms. Finally, ZSV modulation is obtained based on corresponding sector and clamping region and v_0^* reference. Modulation limits are computed at runtime.

If the target ZSV is outside the modulation limits, ψ is switched to $\pi/6$, which is the most convenient value in terms of modulation limits and DPWM60-1 is used. Simultaneously, optimal angle ψ and its relative modulation limits are continuously computed. If, after a change in v_0^* or ψ, ZSV modulation limits become wide enough, the optimal angle is used and the modulation method is switched back from DPWM60-1 to optimal DPWM60, as planned.

Experimental Tests

In order to assess the performance of the proposed method, experimental tests have been conducted on a OW-PMSM coupled to a load machine (PM motor). Torque control is performed on the OW-PMSM fed by the dual inverter system while speed control is performed on the load machine fed by an additional inverter. Experimental set-up is shown in Fig. 4.20 while motor drive parameters are listed in Table 4.1. The 0-axis inductance value

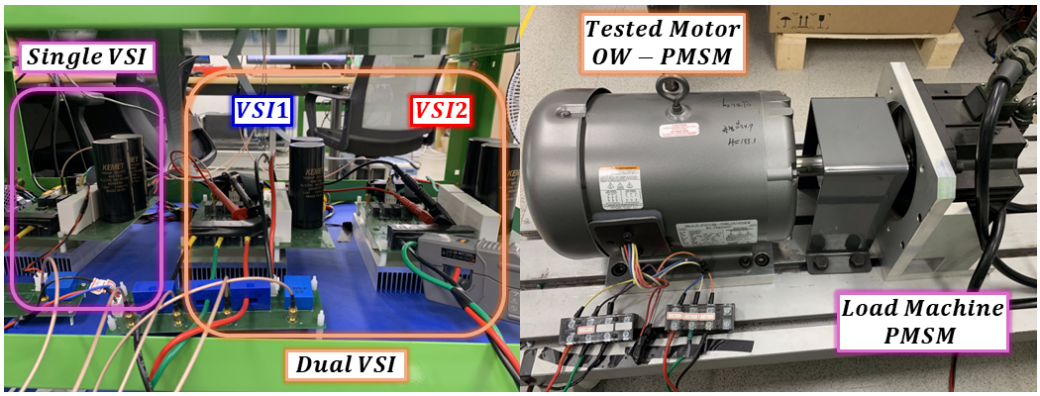

Figure 4.20: Experimental set-up.

Table 4.1: Parameters of OW-PMSM Drive

Parameter	Symbol	Value
Stator Resistance	R	0.5 Ω
d-axis Inductance	L_d	15.9 mH
q-axis Inductance	L_q	45.6 mH
Pole Pairs Number	P	2
Rated Current	I_{nom}	13.9 A_{rms}
Flux Linkage (Fundamental)	λ_f	0.246 Vs
Flux Linkage (Third)	λ_{3f}	0.0087 Vs
DC-link Voltage	V_{dc}	300 V
Switching Frequency	f_{sw}	10 kHz

was estimated through experimental tests. With the ZSV control, the output of the PR resonant controller is measured. Without the ZSV control, the 0-axis current is measured. Hence, the leakage inductance L_0 can be computed. Motor signals were monitored through the D/A converter in the control board.

Fig. 4.21a shows a signal comparison with ZSV modulation disabled (left) and enabled (right) at 1500rpm speed and 5Nm load torque: ZSC i_0 (grey), measured phase a current i_a (green), VSI1 reference voltages v_{a1}^* (pink) and v_{b1}^* (cyan). ZSC i_0 was computed from the measured phase currents as in Eq. (4.5). The red box highlights the change in v_{a1}^* due to the injection of v_0^* for ZSV modulation. As visible, only a small change in the reference voltages is needed to modulate ZSV and effectively suppress ZSC. In addition to that, Fig. 4.21b shows target ZSV v_0^* (pink) and measured ZSV v_0 (cyan) in the same conditions before and after ZSV modulation.

Fig. 4.22 shows a comparison between the conventional SVPWM-based method (left) and the proposed DPWM60-based scheme (right) at 1500rpm speed and 10Nm load torque, with VSI1 PWM pole voltage v_{a1} in cyan. As visible, ZSC suppression is preserved when the method switches to DPWM60 and one-third less switching actions are required. For SVPWM, computed total harmonic distortion (THD) of phase current i_a is 4.2% for both methods and phase voltage v_a THD is 15.5% for SVPWM and 12.6% for DPWM60. Fourier analysis and THD values of phase current and phase voltage are

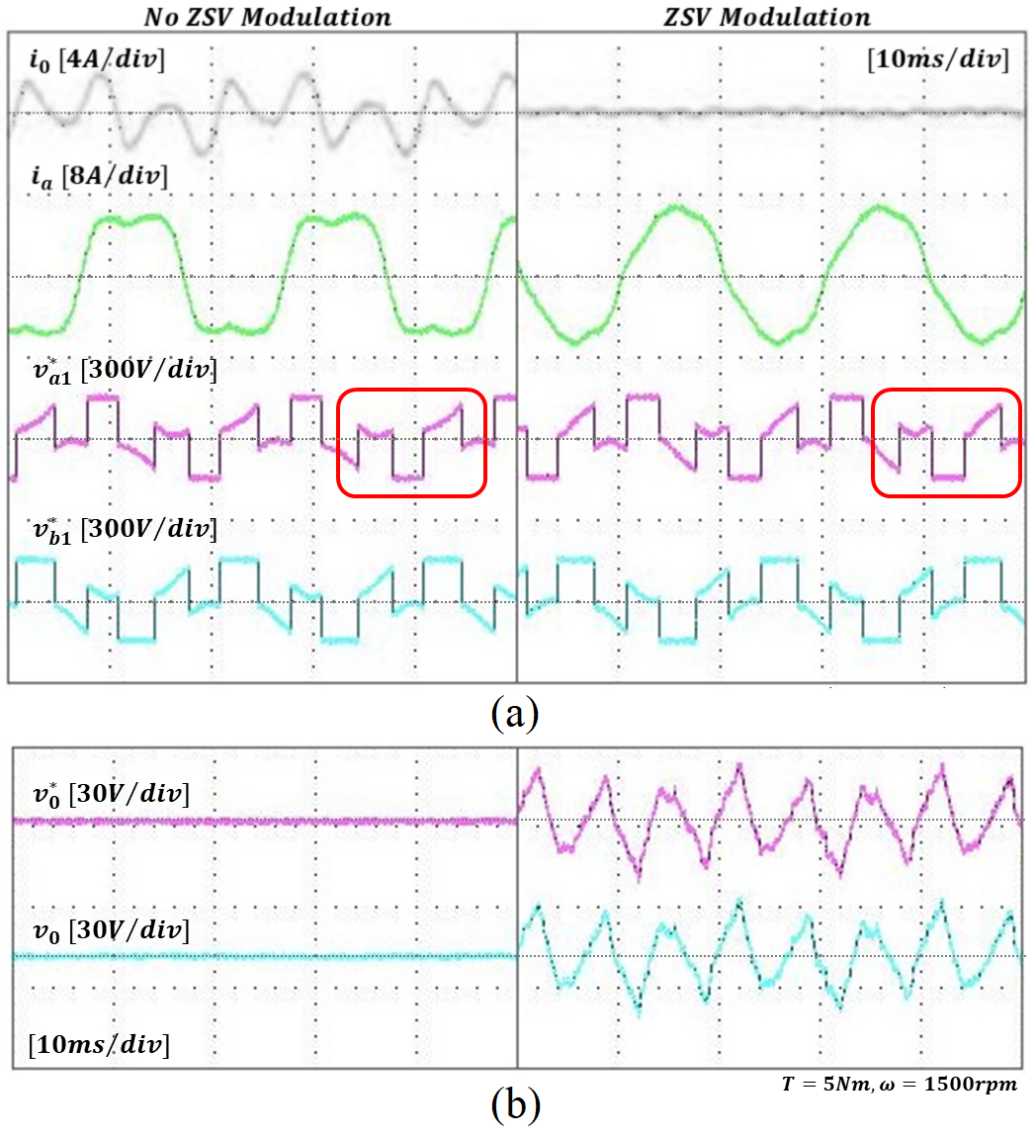

Figure 4.21: Comparison of signals without ZSV modulation (left) and with ZSV modulation (right) ($5Nm$, $1500rpm$).

displayed in Fig. 4.23 for both methods.

Fig. 4.24 shows the previous signals in case of a torque ramp from 0 to $10Nm$ at a constant speed of $1200rpm$. In addition to that, at the bottom of the figure, the runtime computed ZSV modulation limits are shown: positive limit (pink) and negative limit (blue). For low torque values, the motor power factor angle is small, hence, the optimal angle ψ is near $\pi/6$ and

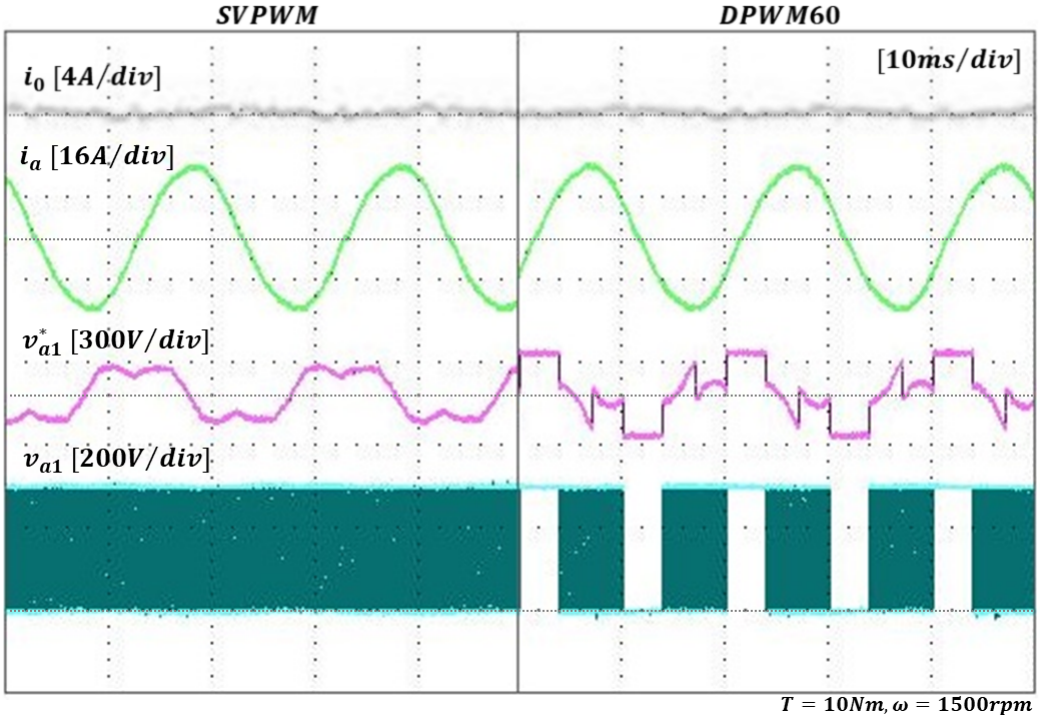

Figure 4.22: Comparison of ZSC suppression with SVPWM (left) and with DPWM60 (right) ($10Nm$, $1500rpm$).

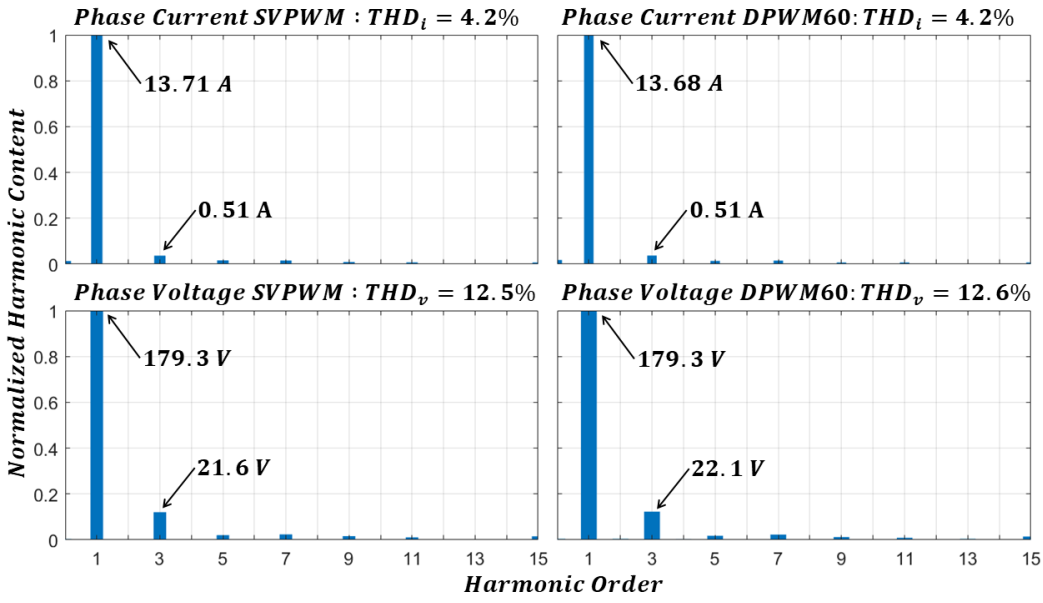

Figure 4.23: Fourier analysis and THD values of phase current and phase voltage for SVPWM and DPWM60 schemes.

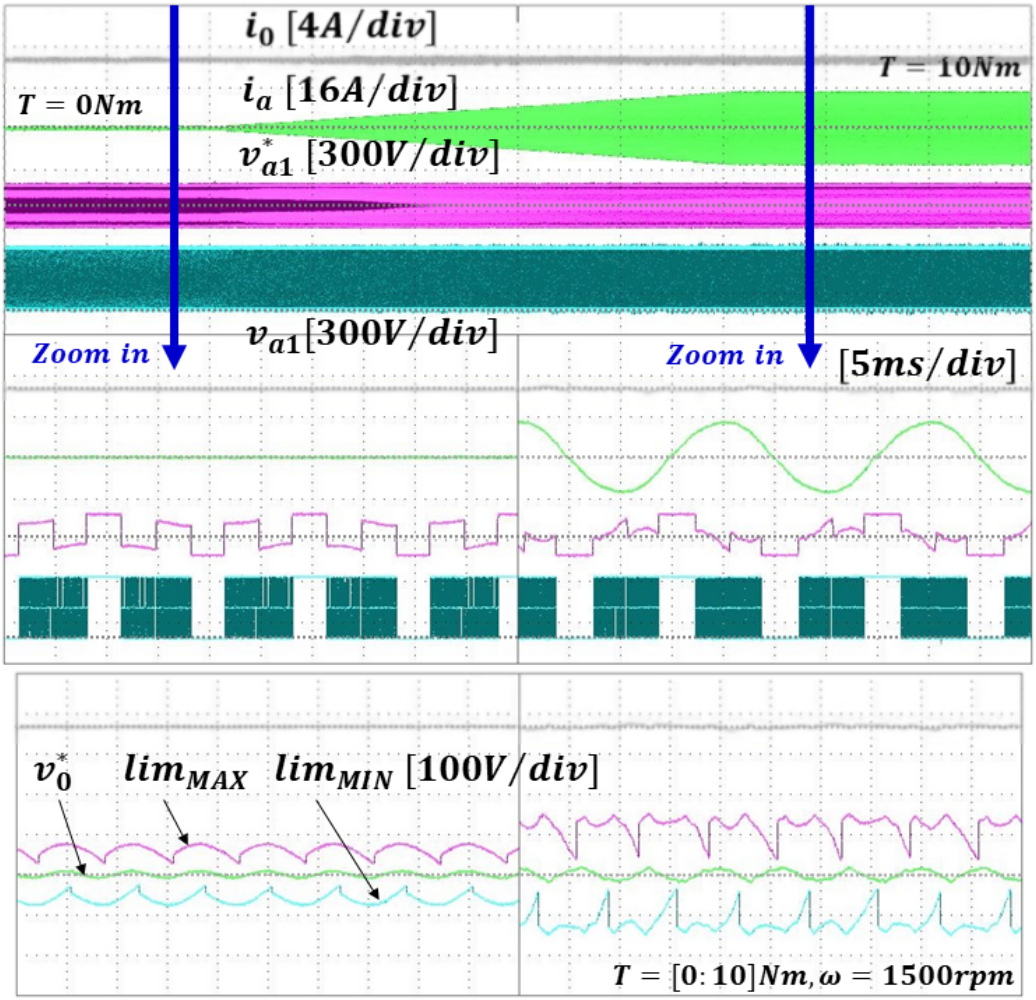

Figure 4.24: Comparison of signals and ZSV modulation limits during a torque ramp from 0 to $10Nm$ ($1500rpm$).

the reference ZSV (green) is well within the limits. With higher torque values, both the power factor angle and the reference voltage modulation index increase, leading to a decrease in the modulation margin. However, v_0^* is still within the limits and ZSC suppression is preserved.

Then, the DC-link voltage was decreased from $300V$ to $200V$ in order to assess the performance of the method when v_0^* is outside the modulation limits. Fig. 4.25 shows ZSC i_0 (grey), DPWM clamping angle ψ (green), ZSV modulation positive limit (pink) and negative limit (cyan) during a torque ramp from 0 to $5Nm$ at a constant speed of $1200rpm$. As for the previous

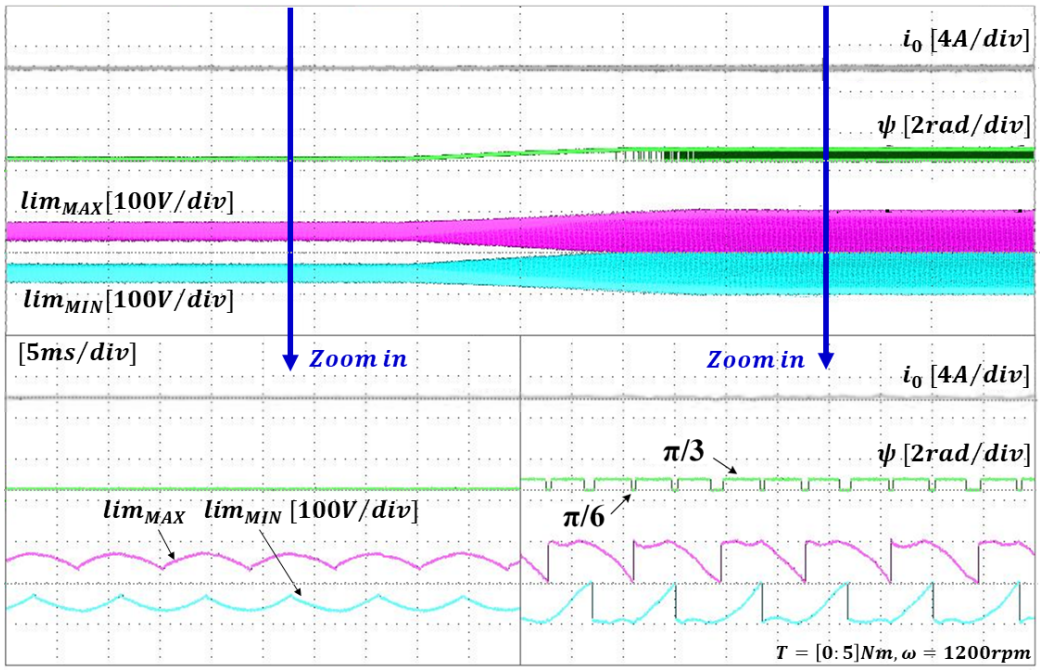

Figure 4.25: Torque ramp from 0 to $5Nm$ ($1200rpm$). Left frame (low torque): target ZSV within the modulation limits, optimal clamping angle is used. Right frame (high torque): when target ZSV is higher than the modulation limits, $\pi/6$ clamping angle is used (algorithm in action).

test, for low torque values, the optimal angle ψ is $\pi/6$ and the reference ZSV is within the limits. With higher torque values, the optimal angle ψ increases to $\pi/3$. With a $200V$ DC-link, however, the ZSV modulation limits are not wide enough. In fact, in the frame on the right, it is possible to see the action of the algorithm previously presented. During the time intervals when v_0^* would be outside the modulation limits obtained with the optimal angle, ψ is set to $\pi/6$ to extend the limits. When v_0^* is again within the limits, ψ is switched back to the computed optimal angle.

In order to compare systems losses between SVPWM and DPWM60, dual inverter input power P_{in} was measured for different values of set speed and torque. Fig. 4.26 shows P_{in} difference between SVPWM method and DPWM60 method (left) and the percentage difference with respect to SVPWM method P_{in} (right). Speed axis in the two graphs is flipped to allow better visibility. Since overall conduction losses do not vary significantly with the

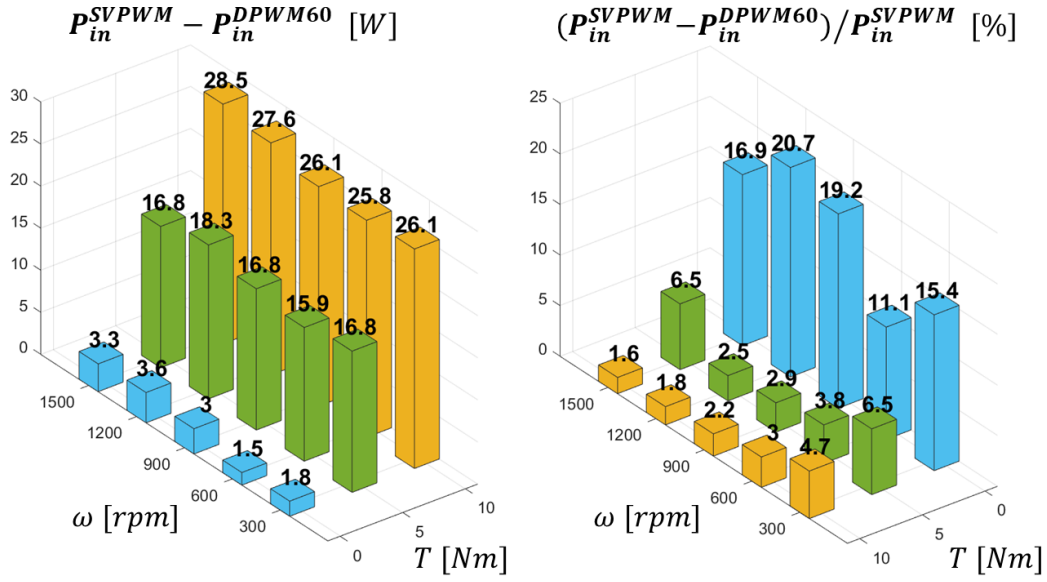

Figure 4.26: Dual-VSI Input power difference between SVPWM and DPWM60 (left) and normalized difference (right).

adopted method [111], [112], the displayed values are a good estimation of the difference in switching losses between SVPWM and DPWM60 method, hence, represent the switching losses reduction achieved by the proposed method.

As switching losses depend on supply current, switching frequency and modulation method, the absolute difference (left) is almost constant with the speed and increases with higher torque (higher supply current). The percentage difference (right), on the other hand, increases with low torque values. Hence, DPWM60 allows consistent losses reduction with respect to SVPWM.

The experimental results confirm that ZSC suppression capability with the proposed method is the same as in conventional SVPWM-based methods. Moreover, DPWM60 scheme allows a consistent absolute decrease in overall inverter losses. Thus, the proposed method successfully achieves both ZSV modulation and switching losses reduction.

This Ph.D. thesis has addressed the critical challenges associated with renewable energy integration and efficient energy storage, focusing on the development and optimization of innovative technologies at the system, com-

ponent, and control levels. The primary motivation behind this work stems from the global push toward decarbonization and the increasing need for reliable, scalable, and efficient solutions for renewable energy management. Specifically, the issues of energy intermittency, storage efficiency, and system scalability were tackled through the design and assessment of advanced energy storage and conversion systems. Two distinct case studies were explored: the optimization of flywheel energy storage systems (FESS) for residential applications and advanced power conversion systems for wind energy

At the system level, the research proposed and evaluated a Hybrid Energy Storage System (HESS) combining Flywheel Energy Storage Systems with chemical batteries for residential applications. This approach demonstrated the potential for enhanced energy savings and self-sufficiency by optimizing the interplay between short-term and long-term storage capabilities.

The component level development included the design of MechSTOR prototype, an ironless, dual-rotor electric machine engineered to minimize electromagnetic losses and maximize self-discharge duration.

At the control level, innovations were achieved through the implementation of advanced modulation strategies for Open-End Winding Permanent Magnet Synchronous Motors (OW-PMSM), addressing key challenges like Zero Sequence Current (ZSC) circulation and high switching losses.

The technical proposals were rigorously validated through simulation and experimental results. The HESS showed promising performance during high PV generation months, enabling relevant reduction in grid energy purchases and increase in self-consumption. MechSTOR prototype demonstrated superior fault tolerance and efficiency, while the novel modulation strategy for OW-PMSM delivered lower switching losses and improved system reliability. Despite these advantages, some limitations were noted, such as the cost implications of increased storage capacity and the need for careful sizing to avoid seasonal over-dimensioning.

Scalability remains a crucial consideration for the proposed solutions. The HESS concept shows strong potential for widespread adoption, particularly in community energy-sharing scenarios, provided that economic feasibility and infrastructure support are addressed. The scalability of power and energy

capacities for larger plants would require further optimization of component sizes and system architectures to maintain efficiency and cost-effectiveness.

Future work should focus on advancing the Technology Readiness Level (TRL) of these systems. For the HESS, real-world pilot projects would help assess long-term performance and economic viability. The MechSTOR prototype could benefit from further mechanical optimization and the integration of magnetic bearings to minimize losses. Finally, the OW-PMSM control strategy should be tested in larger-scale wind energy applications to validate its robustness and efficiency under varying operational conditions.

In conclusion, this research contributes significantly to the development of innovative energy storage and conversion technologies, offering scalable and efficient solutions for the transition to a sustainable energy future. The methodologies and findings presented provide a solid foundation for ongoing development and future advancements in renewable energy integration.

List of Publications

Peer-reviewed Journals

- C. Bianchini, G. Bisceglie, A. Torreggiani, M. Davoli, E. Macrelli, A. Bellini, M. Frigieri, "Effects of the Magnetic Model of Interior Permanent Magnet Machine on MTPA, Flux Weakening and MTPV Evaluation", Machines, 2023, 11, 77

- M. Sintoni, E. Macrelli, A. Bellini, C. Bianchini, "Condition Monitoring of Induction Machines: Quantitative Analysis and Comparison", Sensors, 2023, 23, 1046

Conference Papers

- G. Piraccini, E. Macrelli, C. Bianchini, M. Troncossi and A. Bellini, "Vibration analysis of a motor/generator for flywheel batteries," 2022 IEEE Energy Conversion Congress and Exposition (ECCE), Detroit, MI, USA, 2022, pp. 1-4

- C. Bianchini, G. Sala, A. Torreggiani, N. Giannotta, M. Davoli and E. Macrelli, "Synchronous Reluctance Tubular Machine by Means of Additive Manufacturing," 2022 International Conference on Electrical Machines (ICEM), Valencia, Spain, 2022, pp. 921-927

- E. Macrelli, A. Bellini, C. Bianchini and A. Torreggiani, "Fault Tolerance Analysis of Multiphase Ironless PMSM for Flywheel Batteries," 2023 IEEE 14th International Symposium on Diagnostics for Electrical

Machines, Power Electronics and Drives (SDEMPED), Chania, Greece, 2023, pp. 154-160

- E. Macrelli, A. Bellini, C. Bianchini and A. Torreggiani, "Performance Assessment of a Flywheel Energy Storage System for Households," 2023 IEEE Energy Conversion Congress and Exposition (ECCE), Nashville, TN, USA, 2023, pp. 230-236

- C. Bianchini, G. Sala, M. Frigieri, M. Vogni, N. Giannotta and E. Macrelli, "Extended MTPA-FW Control Technique for PM Electrical Machines with CSI," 2024 International Conference on Electrical Machines (ICEM), Torino, Italy, 2024, pp. 1-7

- G. Sala, C. Bianchini, M. Vogni, E. Macrelli and A. Bellini, "Current Source Inverter Drive of an Ironless Motor for Flywheel Batteries," 2024 IEEE Energy Conversion Congress and Exposition (ECCE), Phoenix, AZ, USA, 2024, pp. 354-358

List of Tables

List of Figures

Acronyms

CMV common mode voltage

DPWM discontinuous pulse width modulation

FESS flywheel energy storage system

GHG greenhouse gas

GWP global warming potential

NZE Net Zero Emissions

OW-IM open-end winding induction motor

OW-PMSM open-end winding permanent magnet synchronous motor

PM permanent magnets

PMSM permanent magnet synchronous motor

PV photovoltaic

PWM pulse width modulation

RES renwwable energy sources

SPWM sinusoidal pulse width modulation

STEPS Stated Policies Scenario

SVPWM space vector pulse width modulation

ZSC zero sequence current

ZSV zero sequence voltage

ZVR zero voltage dwell time redistribution

Bibliography

[1] G. Myhreand, D. Shindell, F.-M. Bréon, W. Collins, J. Fuglestvedt, J. Huang, D. Koch, J.-F. Lamarque, D. Lee, B. Mendoza, T. Nakajima, A. Robock, G. Stephens, T. Takemura, and H. Zhang, *2013: Anthropogenic and Natural Radiative Forcing. In: Climate Change 2013: The Physical Science Basis. Contribution of Working Group I to the Fifth Assessment Report of the Intergovernmental Panel on Climate Change [Stocker, T.F., D. Qin, G.-K. Plattner, M. Tignor, S.K. Allen, J. Boschung, A. Nauels, Y. Xia, V. Bex and P.M. Midgley (eds.)].* Cambridge, United Kingdom and New York, NY, USA: Cambridge University Press, 2013.

[2] *Climate Watch data: GHG Emissions.* Washington, DC: Climate Watch: World Resources Institute, 2024. [Online]. Available: https://www.climatewatchdata.org/ghg-emissions

[3] *Net Zero Roadmap: A Global Pathway to Keep the 1.5 °C Goal in Reach.* Paris: IEA, 2023, Licence: CC BY 4.0. [Online]. Available: https://www.iea.org/reports/net-zero-roadmap-a-global-pathway-to-keep-the-15-0c-goal-in-reach

[4] *IPCC, 2021: Climate Change 2021: The Physical Science Basis. Contribution of Working Group I to the Sixth Assessment Report of the Intergovernmental Panel on Climate Change [Masson-Delmotte, V., P. Zhai, A. Pirani, S.L. Connors, C. Péan, S. Berger, N. Caud, Y. Chen, L. Goldfarb, M.I. Gomis, M. Huang, K. Leitzell, E. Lonnoy, J.B.R. Matthews, T.K. Maycock, T. Waterfield, O. Yelekçi, R. Yu, and B.*

Zhou (eds.)]. Cambridge, United Kingdom and New York, NY, USA: Cambridge University Press, 2021, doi:10.1017/9781009157896.

[5] *IPCC, 2022: Climate Change 2022: Impacts, Adaptation, and Vulnerability. Contribution of Working Group II to the Sixth Assessment Report of the Intergovernmental Panel on Climate Change [H.-O. Pörtner, D.C. Roberts, M. Tignor, E.S. Poloczanska, K. Mintenbeck, A. Alegría, M. Craig, S. Langsdorf, S. Löschke, V. Möller, A. Okem, B. Rama (eds.)]*. Cambridge, United Kingdom and New York, NY, USA: Cambridge University Press, 2022, doi:10.1017/9781009325844.

[6] *IPCC, 2022: Climate Change 2022: Mitigation of Climate Change. Contribution of Working Group III to the Sixth Assessment Report of the Intergovernmental Panel on Climate Change [P.R. Shukla, J. Skea, R. Slade, A. Al Khourdajie, R. van Diemen, D. McCollum, M. Pathak, S. Some, P. Vyas, R. Fradera, M. Belkacemi, A. Hasija, G. Lisboa, S. Luz, J. Malley, (eds.)]*. Cambridge, United Kingdom and New York, NY, USA: Cambridge University Press, 2022, doi:10.1017/9781009157926.

[7] *Emissions Gap Report 2022: The Closing Window - Climate crisis calls for rapid transformation of societies*. Nairobi: United Nations Environment Programme, 2022. [Online]. Available: https://www.unep.org/emissions-gap-report-2022

[8] *World Energy Outlook 2015*. Paris: IEA, 2015, Licence: CC BY 4.0. [Online]. Available: https://www.iea.org/reports/world-energy-outlook-2015

[9] *Renewables 2023*. Paris: IEA, 2024, Licence: CC BY 4.0. [Online]. Available: https://www.iea.org/reports/renewables-2023

[10] G. Dubois, B. Sovacool, C. Aall, M. Nilsson, C. Barbier, A. Herrmann, S. Bruyère, C. Andersson, B. Skold, F. Nadaud, F. Dorner, K. Moberg, J. Ceron, H. Fischer, D. Amelung, M. Baltruszewicz, J. Fischer, F. Benevise, V. Louis, and R. Sauerborn, "It starts at home?

climate policies targeting household consumption and behavioral decisions are key to low-carbon futures," *Energy Research and Social Science*, vol. 52, no. June, pp. 144–158, Jun. 2019.

[11] M. Saunois et al., "The global methane budget 2000–2017," *Earth System Science Data*, vol. 12, no. 3, pp. 1561–1623, 2020. [Online]. Available: https://essd.copernicus.org/articles/12/1561/2020/

[12] M. Etminan, G. Myhre, E. J. Highwood, and K. P. Shine, "Radiative forcing of carbon dioxide, methane, and nitrous oxide: A significant revision of the methane radiative forcing," *Geophysical Research Letters*, vol. 43, no. 24, pp. 12,614–12,623, 2016. [Online]. Available: https://agupubs.onlinelibrary.wiley.com/doi/abs/10.1002/2016GL071930

[13] *Net Zero by 2050.* Paris: IEA, 2021, Licence: CC BY 4.0. [Online]. Available: https://www.iea.org/reports/net-zero-by-2050

[14] *World Energy Outlook 2023.* Paris: IEA, 2023, Licence: CC BY 4.0 (report); CC BY NC SA 4.0 (Annex A). [Online]. Available: https://www.iea.org/reports/world-energy-outlook-2023

[15] *Unlocking the Potential of Distributed Energy Resources.* Paris: IEA, 2022, Licence: CC BY 4.0. [Online]. Available: https://www.iea.org/reports/unlocking-the-potential-of-distributed-energy-resources

[16] *Managing Seasonal and Interannual Variability of Renewables.* Paris: IEA, 2023, Licence: CC BY 4.0. [Online]. Available: https://www.iea.org/reports/managing-seasonal-and-interannual-variability-of-renewables

[17] O. Schmidt, A. Hawkes, A. Gambhir, and I. Staffell, "The future cost of electrical energy storage based on experience rates," *Nature Energy*, vol. 6, p. 17110, 07 2017.

[18] *Innovation landscape brief: Utility-scale batteries.* Abu Dhabi: IRENA, International Renewable Energy Agency, 2019.

[19] M. Ziegler and J. Trancik, "Re-examining rates of lithium-ion battery technology improvement and cost decline," *Energy & Environmental Science*, vol. 14, 04 2021.

[20] H. Ritchie, *The price of batteries has declined by 97% in the last three decades.* OurWorldInData.org, 2021. [Online]. Available: https://ourworldindata.org/battery-price-decline

[21] *Batteries and Secure Energy Transitions.* Paris: IEA, 2024, Licence: CC BY 4.0. [Online]. Available: https://www.iea.org/reports/batteries-and-secure-energy-transitions

[22] W. C. Young and R. Budynas, *Roark's Formulas for Stress and Strain, 7th edition.* McGraw Hill, New York, 2001.

[23] D. Bender, *Sandia Report: Flywheels (SAND2015-3976).* Sandia National Laboratories, Albuquerque, New Mexico and Livermore, California, 2015.

[24] R. Hebner, J. Beno, and A. Walls, "Flywheel batteries come around again," *IEEE Spectrum*, vol. 39, no. 4, pp. 46–51, 2002.

[25] G. Genta, *Flywheel Energy Storage.* Butterworths, London United Kingdom, 1985.

[26] *Flywheel UPS Systems, 50-1000 kVA using TLE or SG Series UPS.* GE Industrial Solutions, Critical Power Products, Plano, TX. [Online]. Available: https://library.industrialsolutions.abb.com/publibrary

[27] J. Beno, R. Thompson, M. Werst, S. Manifold, and J. Zierer, "End-of-life design for composite rotors [flywheel systems]," *IEEE Transactions on Magnetics*, vol. 37, no. 1, pp. 284–289, 2001.

[28] J. T. Tzeng and P. Moy, "Composite energy storage flywheel design for fatigue crack resistance," in *2008 14th Symposium on Electromagnetic Launch Technology*, 2008, pp. 1–6.

[29] *Operating Plants - Stephentown, New York.* Beacon, LCC. [Online]. Available: https://beaconpower.com/stephentown-new-york/

[30] M. Huart and L. Sonnerup, "Jet flywheel generators," *Proceedings of the Institution of Mechanical Engineers, Part A: Power and Process Engineering*, vol. 200, no. 2, pp. 95–100, 1986.

[31] A. Canova, F. Campanelli, and M. Quercio, "Flywheel energy storage system in italian regional transport railways: A case study," *Energies*, vol. 15, p. 1096, 02 2022.

[32] K. Tan and Y. Fah, "Reducing fuel consumption using flywheel battery technology for rubber tyred gantry cranes in container terminals," *Journal of Power and Energy Engineering*, vol. 5, pp. 15–33, 2017.

[33] A. Cotton, *Audi R18 (2014).* Racecar Engineering, June 1, 2014. [Online]. Available: https://www.racecar-engineering.com/cars/audi-lmp14/

[34] R. Votel and D. Sinclair, "Comparison of control moment gyros and reaction wheels for small earth-observing satellites," in *26th Annual AIAA/USU Conference on Small Satellites*, 2012. [Online]. Available: https://api.semanticscholar.org/CorpusID:52243526

[35] R. O. Bartlett, G. Brown, and J. Levinthal, "Energy storage flywheels on spacecraft," in *25th ANNUAL AAS GUIDANCE AND CONTROL CONFERENCE*, 2002. [Online]. Available: https://ntrs.nasa.gov/api/citations/20020060506/downloads/20020060506.pdf

[36] C. Bianchini, A. Torreggiani, D. David, and A. Bellini, "Design of motor/generator for flywheel batteries," *IEEE Transactions on Industrial Electronics*, vol. 68, no. 10, pp. 9675–9684, 2021.

[37] K. Liu, X. Fu, M. Lin, and L. Tai, "Ac copper losses analysis of the ironless brushless dc motor used in a flywheel energy storage system," *IEEE Transactions on Applied Superconductivity*, vol. 26, no. 7, pp. 1–5, 2016.

[38] I. M. Higginson, H. Hess, and J. D. Law, "Ironless permanent magnet synchronous machine stiffness calculations for flywheel energy storage systems," in *2011 IEEE International Electric Machines and Drives Conference (IEMDC)*, 2011, pp. 1357–1362.

[39] S.-M. Jang, D.-J. You, K.-J. Ko, and S.-K. Choi, "Design and experimental evaluation of synchronous machine without iron loss using double-sided halbach magnetized pm rotor in high power fess," *IEEE Transactions on Magnetics*, vol. 44, no. 11, pp. 4337–4340, 2008.

[40] L. Parsa, "On advantages of multi-phase machines," in *31st Annual Conference of IEEE Industrial Electronics Society, 2005. IECON 2005.*, 2005, pp. 6 pp.–.

[41] E. Macrelli, A. Bellini, C. Bianchini, and A. Torreggiani, "Fault tolerance analysis of multiphase ironless pmsm for flywheel batteries," in *2023 IEEE 14th International Symposium on Diagnostics for Electrical Machines, Power Electronics and Drives (SDEMPED)*, 2023, pp. 154–160.

[42] E. P. Wiechmann, P. Aqueveque, R. Burgos, and J. Rodriguez, "On the efficiency of voltage source and current source inverters for high-power drives," *IEEE Transactions on Industrial Electronics*, vol. 55, no. 4, pp. 1771–1782, 2008.

[43] V. Madonna, G. Migliazza, P. Giangrande, E. Lorenzani, G. Buticchi, and M. Galea, "The rebirth of the current source inverter: Advantages for aerospace motor design," *IEEE Industrial Electronics Magazine*, vol. 13, no. 4, pp. 65–76, 2019.

[44] G. Migliazza, E. Carfagna, G. Buticchi, F. Immovilli, and E. Lorenzani, "Extended speed range control for a current source inverter variable speed drive," in *IECON 2021 – 47th Annual Conference of the IEEE Industrial Electronics Society*, 2021.

[45] E. Lorenzani, F. Immovilli, C. Bianchini, and A. Bellini, "Performance analysis of a modified current source inverter for photovoltaic microinverter applications," in *IECON 2013 - 39th Annual Conference of the IEEE Industrial Electronics Society*, 2013, pp. 1809–1814.

[46] G. Migliazza, G. Buticchi, E. Carfagna, E. Lorenzani, V. Madonna, P. Giangrande, and M. Galea, "Dc current control for a single-stage current source inverter in motor drive application," *IEEE Transactions on Power Electronics*, vol. 36, no. 3, pp. 3367–3376, 2020.

[47]

[48] ROHM, "s4101 1200 v 55 a, n-channel sic power mosfet bare die," ROHM Semiconductors, Tech. Rep., 2018.

[49] ——, "s6305 1200 v 60 a, ultrafast high voltage diode," ROHM Semiconductors, Tech. Rep., 2022.

[50] W. T. Thomson, *Theory of Vibration with Applications*. London and New York: Taylor&Francis, 1993.

[51] G. Piraccini, E. Macrelli, C. Bianchini, M. Troncossi, and A. Bellini, "Vibration analysis of a motor/generator for flywheel batteries," in *2022 IEEE Energy Conversion Congress and Exposition (ECCE)*, 2022, pp. 1–4.

[52] F. Goris and E. L. Severson, "A review of flywheel energy storage systems for grid application," in *IECON 2018 - 44th Annual Conference of the IEEE Industrial Electronics Society*, 2018, pp. 1633–1639.

[53] T. Engelmann, R. Vor dem Esche, and R. Tudi, "Fast response flywheel energy storage technology for virtual power plants and microgrids," *Proc. Elect. Energy Storage Appl. Technol.*, pp. 1–11, 2017.

[54] X. Li and A. Palazzolo, "A review of flywheel energy storage systems: state of the art and opportunities," *Journal of Energy Storage*, vol. 46, p. 103576, 2022.

[55] F. Nadeem, S. M. S. Hussain, P. K. Tiwari, A. K. Goswami, and T. S. Ustun, "Comparative review of energy storage systems, their roles, and impacts on future power systems," *IEEE Access*, vol. 7, pp. 4555–4585, 2019.

[56] M. Farhadi and O. Mohammed, "Energy storage technologies for high-power applications," *IEEE Transactions on Industry Applications*, vol. 52, no. 3, pp. 1953–1961, 2016.

[57] M. E. Amiryar and K. R. Pullen, "A review of flywheel energy storage system technologies and their applications," *Applied Sciences*, vol. 7, no. 3, 2017. [Online]. Available: https://www.mdpi.com/2076-3417/7/3/286

[58] M. L. Lazarewicz and T. M. Ryan, "Integration of flywheel-based energy storage for frequency regulation in deregulated markets," in *IEEE PES General Meeting*, 2010, pp. 1–6.

[59] V. Dache and V. Sgarciu, "Performance analysis of a low-cost small-scale flywheel energy storage system," in *2021 23rd International Conference on Control Systems and Computer Science (CSCS)*, 2021, pp. 53–56.

[60] E. Bekiroglu and S. Esmer, "Peak shaving control of ev charge station with a flywheel energy storage system in micro grid," in *2023 11th International Conference on Smart Grid (icSmartGrid)*, 2023, pp. 1–5.

[61] W. M. Brobeck, *Conceptual Design of a Flywheel Energy Storage System (SAND79-7088)*. Sandia Laboratories, Albuquerque, New Mexico, 1979.

[62] E. Macrelli, A. Bellini, C. Bianchini, and A. Torreggiani, "Performance assessment of a flywheel energy storage system for households," in *2023 IEEE Energy Conversion Congress and Exposition (ECCE)*, 2023, pp. 230–236.

[63] (2024) Lg energy solutions website. [Online]. Available: https://www.lgessbattery.com/eu/home-battery/product-info.lg

[64] X. Li, N. Erd, and A. Binder, "Evaluation of flywheel energy storage systems for residential photovoltaic installations," in *2016 International Symposium on Power Electronics, Electrical Drives, Automation and Motion (SPEEDAM)*, 2016, pp. 255–260.

[65] J. Weniger, T. Tjaden, and V. Quaschning, "Sizing of residential pv battery systems," *Energy Procedia*, vol. 46, p. 78–87, 12 2014.

[66] *MICENE - Misure dei consumi di energia elettrica nel settore domestico.* eERG (end-use Efficiency Research Group), Dipartimento di Energetica, Politecnico di Milano, 2022. [Online]. Available: https://www.eerg.it/index.php?p=Progetti$_{-M}ICENE$

[67] D. D. and G. C., *UCI Machine Learning Repository.* Irvine, CA: University of California, School of Information and Computer Science, 2019. [Online]. Available: http://archive.ics.uci.edu/ml

[68] *Photovoltaic Geographical Information System.* EU-ScienceHub, European Commission. [Online]. Available: https://joint-research-centre.ec.europa.eu/pvgis-online-tool$_en$

[69] *Wind power capacity in the Net Zero Scenario, 2015-2030.* Paris: IEA, 2023, Licence: CC BY 4.0. [Online]. Available: https://www.iea.org/data-and-statistics/charts/wind-power-capacity-in-the-net-zero-scenario-2015-2030

[70] *Annual offshore wind capacity additions by country/region, 2015-2022.* Paris: IEA, 2021, Licence: CC BY 4.0. [Online]. Available: https://www.iea.org/data-and-statistics/charts/annual-offshore-wind-capacity-additions-by-country-region-2015-2022

[71] *Patent insight report: Offshore wind energy.* Vienna: EPO and IRENA, 2023. [Online]. Available: https://www.irena.org/-/media/Files/IRENA/Agency/Publication/2023/Nov/EPO-IRENA-Offshore-wind-patent-insight-report-2023.pdf

[72] *Floating offshore wind outlook.* Abu Dhabi: IRENA, International Renewable Energy Agency, 2024. [Online]. Available: https://www.irena.org/-/media/Files/IRENA/Agency/Publication/2024/Jul/IRENA-G7-Floating-offshore-wind-outlook-2024.pdf

[73] *Uniting action on climate and biodiversity.* Fredericia: Ørsted, 2023. [Online]. Available: https://orsted.com/en/insights/white-papers/uniting-action-on-climate-and-biodiversity

[74] *Tracking the impacts of innovation: Offshore wind as a case study.* Abu Dhabi: IRENA, International Renewable Energy Agency, 2021. [Online]. Available: https://www.irena.org/-/media/Files/IRENA/Agency/Publication/2021/Jun/IRENA-Impacts-Innovation-2021.pdf

[75] *Geopolitics of the Energy Transformation: The Hydrogen Factor.* Abu Dhabi: IRENA, International Renewable Energy Agency, 2022. [Online]. Available: https://www.irena.org/publications/2022/Jan/ Geopolitics-of-the-Energy-Transformation-Hydrogen

[76] *Patent insight report. Innovation trends in electrolysers for hydrogen production.* Vienna: EPO and IRENA, 2022. [Online]. Available: https://www.epo.org/news-events/news/2022/20220512.html

[77] *Floating offshore wind outlook.* Abu Dhabi: IRENA, International Renewable Energy Agency, 2024. [Online]. Available: https://www.irena.org/-/media/Files/IRENA/Agency/Publication/2024/Jul/IRENA-G7-Floating-offshore-wind-outlook-2024.pdf

[78] Z. Chen, J. M. Guerrero, and F. Blaabjerg, "A review of the state of the art of power electronics for wind turbines," *IEEE Transactions on Power Electronics*, vol. 24, no. 8, pp. 1859–1875, 2009.

[79] O. C. Castillo, V. R. Andrade, J. J. R. Rivas, and R. O. González, "Comparison of power coefficients in wind turbines considering the tip speed ratio and blade pitch angle," *Energies*, vol. 16, no. 6, 2023. [Online]. Available: https://www.mdpi.com/1996-1073/16/6/2774

[80] P. C. Sen, *Principles of Electric Machines and Power Electronics, 3rd Edition.* Wiley, 2014.

[81] Q. Wang and L. Chang, "An intelligent maximum power extraction algorithm for inverter-based variable speed wind turbine systems," *IEEE Transactions on Power Electronics*, vol. 19, no. 5, pp. 1242–1249, 2004.

[82] P. Alves Dias, S. Bobba, S. Carrara, and B. Plazzotta, "The role of rare earth elements in wind energy and electric mobility," *EUR 30488 EN, Publications Office of the European Union, Luxembourg*, vol. ISBN 978-92-76-27016-4, JRC122671, 2020.

[83] *Geopolitics of the Energy Transition: Critical Materials.* Abu Dhabi: IRENA, International Renewable Energy Agency, 2023. [Online]. Available: https://www.irena.org/Publications/2023/Jul/ Geopolitics-of-the-Energy-Transition-Critical-Materials

[84] P. Tenca, A. A. Rockhill, and T. A. Lipo, "Wind turbine current-source converter providing reactive power control and reduced harmonics," *IEEE Transactions on Industry Applications*, vol. 43, no. 4, pp. 1050–1060, 2007.

[85] S. Nishikata and F. Tatsuta, "A new interconnecting method for wind turbine/generators in a wind farm and basic performances of the integrated system," *IEEE Transactions on Industrial Electronics*, vol. 57, no. 2, pp. 468–475, 2010.

[86] H. Stemmler and P. Guggenbach, "Configurations of high-power voltage source inverter drives," in *1993 Fifth European Conference on Power Electronics and Applications*, 1993, pp. 7–14 vol.5.

[87] L. Rovere, A. Formentini, G. L. Calzo, P. Zanchetta, and T. Cox, "Zero-sequence voltage elimination for dual-fed common dc-link open-end winding pmsm high-speed starter–generator—part i: Modulation," *IEEE Transactions on Industry Applications*, vol. 55, no. 6, pp. 7804–7812, 2019.

[88] A. Dehghani kiadehi, K. El Khamlichi Drissi, and C. Pasquier, "Angular modulation of dual-inverter fed open-end motor for electrical vehicle appli-

cations," *IEEE Transactions on Power Electronics*, vol. 31, no. 4, pp. 2980–2990, 2016.

[89] J. Kim, J. Jung, and K. Nam, "Dual-inverter control strategy for high-speed operation of ev induction motors," *IEEE Transactions on Industrial Electronics*, vol. 51, no. 2, pp. 312–320, 2004.

[90] J. Hong, H. Lee, and K. Nam, "Charging method for the secondary battery in dual-inverter drive systems for electric vehicles," *IEEE Transactions on Power Electronics*, vol. 30, no. 2, pp. 909–921, 2015.

[91] T. M. Jahns, "Improved reliability in solid-state ac drives by means of multiple independent phase drive units," *IEEE Transactions on Industry Applications*, vol. IA-16, no. 3, pp. 321–331, 1980.

[92] B. Mecrow, A. Jack, J. Haylock, and J. Coles, "Fault tolerant permanent magnet machine drives," in *1995 Seventh International Conference on Electrical Machines and Drives (Conf. Publ. No. 412)*, 1995, pp. 433–437.

[93] B. Welchko, T. Lipo, T. Jahns, and S. Schulz, "Fault tolerant three-phase ac motor drive topologies: a comparison of features, cost, and limitations," *IEEE Transactions on Power Electronics*, vol. 19, no. 4, pp. 1108–1116, 2004.

[94] D. Casadei, G. Grandi, A. Lega, and C. Rossi, "Multilevel operation and input power balancing for a dual two-level inverter with insulated dc sources," *IEEE Transactions on Industry Applications*, vol. 44, no. 6, pp. 1815–1824, 2008.

[95] M. Pathmanathan and P. W. Lehn, "Control algorithm for energy storage integration with an open-winding wind turbine generator," in *IECON 2021 – 47th Annual Conference of the IEEE Industrial Electronics Society*, 2021, pp. 1–6.

[96] L. Zhu, F. Zhang, S. Jin, and D. Wang, "Maximum power point tracking control of brushless doubly-fed wind power generator with open winding fed by dual two-level inverters," in *2014 17th International Conference on Electrical Machines and Systems (ICEMS)*, 2014, pp. 1362–1367.

[97] B. Sun, C. Gao, and M. Liu, "A series multilevel converter with phase dc bus voltage fluctuation suppression for pmsg in wind power system," in *2020 IEEE 3rd International Conference on Electronics Technology (ICET)*, 2020, pp. 283–288.

[98] Y. Chou and H. Nian, "Sensorless control of pmsg based on dual two-level inverter open winding configuration for wind turbines," in *2012 15th International Conference on Electrical Machines and Systems (ICEMS)*, 2012, pp. 1–6.

[99] V. T. Somasekhar, S. Srinivas, and K. K. Kumar, "Effect of zero-vector placement in a dual-inverter fed open-end winding induction-motor drive with a decoupled space-vector pwm strategy," *IEEE Transactions on Industrial Electronics*, vol. 55, no. 6, pp. 2497–2505, 2008.

[100] Y. Zhou and H. Nian, "Zero-sequence current suppression strategy of open-winding pmsg system with common dc bus based on zero vector redistribution," *IEEE Transactions on Industrial Electronics*, vol. 62, no. 6, pp. 3399–3408, 2015.

[101] J. M. Liu and Z. Q. Zhu, "Improved sensorless control of permanent-magnet synchronous machine based on third-harmonic back emf," *IEEE Transactions on Industry Applications*, vol. 50, no. 3, pp. 1861–1870, 2014.

[102] A. Somani, R. K. Gupta, K. K. Mohapatra, and N. Mohan, "On the causes of circulating currents in pwm drives with open-end winding ac machines," *IEEE Transactions on Industrial Electronics*, vol. 60, no. 9, pp. 3670–3678, 2013.

[103] H. Zhan, Z.-q. Zhu, and M. Odavic, "Analysis and suppression of zero sequence circulating current in open winding pmsm drives with common dc bus," *IEEE Transactions on Industry Applications*, vol. 53, no. 4, pp. 3609–3620, 2017.

[104] Q. An, J. Liu, Z. Peng, L. Sun, and L. Sun, "Dual-space vector control of open-end winding permanent magnet synchronous motor drive fed by dual

inverter," *IEEE Transactions on Power Electronics*, vol. 31, no. 12, pp. 8329–8342, 2016.

[105] Z. Shen, D. Jiang, L. Zhu, Y. Xu, T. Zou, Z. Liu, and R. Qu, "A novel zero-sequence current elimination pwm scheme for an open-winding pmsm with common dc bus," *IEEE Transactions on Power Electronics*, vol. 34, no. 12, pp. 12 476–12 490, 2019.

[106] W. Hu, H. Nian, and T. Zheng, "Torque ripple suppression method with reduced switching frequency for open-winding pmsm drives with common dc bus," *IEEE Transactions on Industrial Electronics*, vol. 66, no. 1, pp. 674–684, 2019.

[107] A. Hava, R. Kerkman, and T. Lipo, "Simple analytical and graphical methods for carrier-based pwm-vsi drives," *IEEE Transactions on Power Electronics*, vol. 14, no. 1, pp. 49–61, 1999.

[108] R. Chinthamalla, D. Sahoo, and S. Jain, "A discontinuous switching technique to eliminate common mode voltage with reduced switching losses for an open end winding induction motor drive solar water pump," in *2016 IEEE Students' Conference on Electrical, Electronics and Computer Science (SCEECS)*, 2016, pp. 1–5.

[109] K. Lee and Y. Han, "Simple discontinuous pulse-width modulation scheme for the loss reduction of a dual inverter fed an open-end winding induction motor," *IEEE Transactions on Energy Conversion*, vol. 38, no. 1, pp. 495–506, 2023.

[110] J. M. Liu and Z. Q. Zhu, "Improved sensorless control of permanent-magnet synchronous machine based on third-harmonic back emf," *IEEE Transactions on Industry Applications*, vol. 50, no. 3, pp. 1861–1870, 2014.

[111] P. Perruchoud and P. Pinewski, "Power losses for space vector modulation techniques," in *Power Electronics in Transportation*, 1996, pp. 167–173.

[112] D.-W. Chung and S.-K. Sul, "Minimum-loss strategy for three-phase pwm rectifier," *IEEE Transactions on Industrial Electronics*, vol. 46, no. 3, pp. 517–526, 1999.

Borsa di dottorato del Programma Operativo Nazionale Ricerca e Innovazione 2014-2020 (CCI 2014IT16M2OP005), risorse FSE REACT-EU, Azione IV.4 "Dottorati e contratti di ricerca su tematiche dell'innovazione" e Azione IV.5 "Dottorati su tematiche Green.", J35F21003140006